University of Alberta

Morphology Control, Surface Functionalization and Optical Response of Silicon Nanocrystals

by

Zhenyu Yang

A thesis submitted to the Faculty of Graduate Studies and Research
in partial fulfillment of the requirements for the degree of

Doctor of Philosophy

Department of Chemistry

Spring, 2014
Edmonton, Alberta

I dedicate this thesis to my father Mr. Jinhui Yang, and mother Mrs. Liyan Chen.

“……仍願於箕星之分，巫閭之旁，追琢貞瑑，彰灼來葉……”

——李商隱 《太尉衛公會昌一品集序》

Abstract

As one of the most commonly applied semiconductors, nanostructured silicon has received considerable attention over the past several decades due to its suitable band gap for light harvesting (1.2 eV for bulk crystal and up to 1.9 eV for nanocrystals), unique tunable photoluminescence (PL) and high biocompatibility and low toxicity. Significant effort has been made to fabricate and optimize silicon nanocrystal (SiNC) based devices. However, numerous important fundamental questions still remain. Therefore, this thesis mainly focuses on the elucidation of several fundamental research topics in the SiNC area, including nanocrystalline morphology control and evolution, surface functionalization and corresponding optical response of SiNCs, as well as the synthesis of particle/polymer hybrid materials.

The thesis starts with an introduction about physical and chemical properties of SiNCs, general synthetic approaches, the present strategies of morphology control, as well as numerous surface modification approaches. Then details of a convenient method for preparing alkyl-functionalized silicon nanocubes are provided in Chapter Two with discussions about the mechanism of the particle size and shape control. Chapter Three focuses on the “one-pot” synthesis of homogenous SiNC/polystyrene hybrid materials. Also, three prototype micro/nano structures were fabricated for the demonstration of the utility of

material hybrid characteristics such as bright photoluminescence (PL), high solvent processability and chemical stability. In Chapter Four, surface functionalization of SiNCs *via* thermally induced hydrosilylation is reexamined. The successful ligand functionalization processed at various temperatures under air atmosphere and the formation of ligand oligomers on SiNCs were noticed. These strongly suggest that an alternative mechanism exists to promote low temperature thermal hydrosilyaltion as well as ligand oligomerization on SiNCs. The potential influence of surface oxide species on SiNC optical properties is further described in Chapter Five. Based on a systematic study, it is clear that the surface defects or traps created by suboxides are strongly relevant to the non-phonon assisted nanosecond PL lifetime decay found from yellow/orange emitting ligand-functionalized SiNCs. Finally, Chapter Six presents the conclusions of each chapter and some recommended future work relative to SiNC science.

Acknowledgement

It is hard to believe that four and a half years have passed and my Ph.D. life is almost to the end. It was a great time to live in this snow kingdom, learn new knowledge, make friends, and chase my dream. However, some difficulties from both the normal and academic lives did exist and here I need to admit that I did plan to quit the Ph.D. study (more than one time) when certain unexpected difficulties suddenly appear. My friends, family members, professors and department staff, it is your giant help and assistance that support me to overcome these affairs, guide my way, and finally let me stand here and give my public defense talk.

I would like to thank innumerable people here. First of all, I would like to thank my supervisor Dr. Jonathan G. C. Veinot, not only for his excellent guidance, encouragement and generous support during my study, but also for his great patience and tolerance. Jon, I still remember that as a first year group member, I broke two quartz tubes, three quartz boats, six Schlenk flasks, five grams of GeI_2 solid, and accidentally connected the glovebox with air atmosphere twice. I reported all of these and you still looked calm and friendly. You might not know that actually it was the your first lesson to show me how a good leader should behave. I have been learning a lot from you about things inside and outside academia, and gradually grown from a fresh graduate student to a skilled

researcher. Also, without your help I certainly could not finish this thesis.

I would like to thank my examination committee members Drs. Jillian M. Buriak, Arthur Mar, Charles Lucy, Douglas G. Ivey, and external committee member Dr. Bruce Lennox from at the McGill University, for their valuable time and advice on my annual reports, candidacy exam, and also this thesis. I would like to thank Drs. Al Meldrum, Frank Hegmann, Oded Millo, Jan Linnros and their group members for those many constructive discussions and excellent collaborations. In addition, I would like to thank Professor Bernhard Rieger and his group member, especially Dr. Frank Deubel, Julian Kehrle and Ignaz Höhlein, for their nice hosting when I was at the Technische Universität München as a visiting Ph.D. student.

Surely I need to thank the past and current Veinot group members, you are awesome teammates. I would like to thank Stephen Barry and Dr. Melanie Hoffmann, who helped me a lot on experiments from the beginning. I need to thank Drs. Colin Hessel, Eric Henderson, Rhett Clark, Joel Kelly, José Rodriguez and Ms. Sarah Regli for their outstanding results, ideas, and comments which are extremely useful recourses for my research projects. I would like to thank all of the group members including Dr. Muhammad Iqbal, Dr. Purkait, "fresh" Dr. Mita Dasog, Leah Coumont, Christina Gonzalez, Lida Hadidi, Morteza Javadi, Yi Zhai, Muhammad Islam, Regina Sinelnikov, Maryam Aghajamali, Alexander Dobbie,

Maike Wahl and Kathrin Bader for the fun time and useful scientific discussions. Alex, I wish you have a bright future in the graduate school. Maike and Kathrin, I really hope to see both of you again in Munich!

Outside the Veinot group, I would like to thank the physicists Ross Lockwood, Yanyan Zhi, and Glenda De los Reyes for their great support in sample measurements. I would also like to thank numerous staff and technicians from various laboratories, departments and institutes: Wayne Moffat, Brett Mason, Dr. Norman Gee, Dr. Yoram Apelblat, Dr. Jason Cooke, Greg Popowich, De-ann Rollings, George Pemberton, Dr. Nathan Gerein, Dr. Kai Cui, Dr. Dimitre Karpuzov, Dr. Shixiong Xu, Dr. Randy Whittal, Dr. Xiaoxia Ye, Jing Zheng, Bernie Hippel, Ryan Lewis, Anita Weiler, and Bonnie Gover for their help and assistance.

I am glad to have lots of awesome friends over countries and continents. They have been supporting me throughout my graduate study years. I would like to thank Yanzhang He, Tianyu Lin, Dr. Kun Zhao, Fanxing Kong, Zhengting Ren, Jie Wen, Yaohui Pan, Shunzhen Huo, Shunwan Huo, Yuheng Huang, Dr. Wenda Huang, Dr. Long Qi, Zhenggang Xu, Xiaoye Wang, and Dr. Jian Deng for your enthusiastic help. Herein, I would especially like to thank Jingwen Chen for opening my door and lighting the sky above

Last but not the least, I would like to thank my parents for their endless love

and support. Mama, thank you for giving me this wonderful life and freedom to experience everything in the world, including the happiness and the pain. Baba, I know you would be the first one who would feel proud of me if I finally defend my Ph.D. Although you do not understand English and cannot read this thesis by yourself anymore, I will certainly let you know the details if I could see you in my dream again. Also, I would like to thank my pets: Maomao (the cat) and Gaga (the dog) to assist my Mom through tough times. I love you forever (although you might not like each other).

Table of Contents

List of Figures

List of Schemes

List of Symbols, Nomenclature, and Abbreviations

Å	Angstrom
^{o}C	Degrees Celsius
h	Planck's constant
μ	Reduced mass of electron and hole
$\bar{R}$	Average crystal diameter
ε_r	Material relative permittivity
arb.	Arbitrary units
BE	Binding energy
CB	Conduction band
CVD	Chemical vapor deposition
DOS	Density of states
E	Energy
EDS	Energy dispersive X-ray spectroscopy
E_g	Bandgap
EI	Electron ionization
EMA	Effective mass approximation
E_R	Rydberg energy
FFT	Fast Fourier transform
FT-IR	Fourier transform infrared spectroscopy
GPC	Gel permeation chromatography
HAADF	High-angle annular dark field electron microscopy
HEBM	High-energy ball milling
HOMO	Highest occupied molecular orbital
HRTEM	High resolution transmission electron microscopy

HSQ	Hydrogen silsesquioxane
IR	Infrared
K	Degrees Kelvin
λ	Wavelength
LED	light emitting diode
LUMO	Lowest unoccupied molecular orbital
m_e^*	Effective masses of the electron
m_h^*	Effective masses of the hole
MIBK	Methyl isobutyl ketone
MO	Molecular orbital
MRI	Magnetic resonance imaging
MS	Mass spectroscopy
n	Number
NALDI	nanostructure-assisted laser desorption/ionization
NC	Nanocrystal
NMR	Nuclear magnetic resonance
PL	Photoluminescence
PS	Polystyrene
PTFE	Polytetrafluoroethylene
QD	Quantum dot
QY	Quantum yield
R	Radius
rpm	Rotations per minute
SAED	Selected area electron diffraction
SEM	Scanning electron microscopy
SiNCs	Silicon nanocrystals

STEM	Scanning transmission electron microscopy
STM	Scanning tunneling microscopy
TEM	Transmission electron microscopy
TGA	Thermogravimetric analysis
UV	Ultraviolet
UV-Vis	Ultraviolet-visible (spectroscopy)
VB	Valence band
XPS	X-ray photoelectron spectroscopy
XRD	X-ray powder diffraction

Chapter 1

Introduction

1.1 Introduction: Quantum Dots

During the last thirty years, nanomaterials and related research areas have received immense interest and unprecedented development. Numerous reasons for this exist. Among them are the invention of electron microscopes and the discoveries of new nanoscale materials (*e.g.*, fullerenes,[2] colloidal semiconductor nanoparticles[3]). The size reduction of materials to nanoscale dimensions drastically increases the surface area to volume ratio and introduces size dependent changes in electronic structure that substantiality alter the material physical and chemical behavior (*e.g.*, catalytic properties, solubility, quantum confinement effects).[4] Today, our understanding of nanomaterials is well-developed, and significant progress has been made toward the application of nanomaterials in electronics, energy conversion and storage, catalysts, medicine and biological imaging.[4]

Since the discovery of quantum size effect in CdS nanocrystals (NC) by Brus and his colleagues in 1983,[3] I nvestigations of semiconductor nanocystal, or quantum dot (QD) synthesis as well as their various applications have become a key part of the nanotechnology landscape. QDs are pseudo-spherical semiconductor nanoparticles with dimensions approaching the diameter of an exciton in the bulk semiconductor.[5] These structures are particularly interesting

because their optoelectronic properties are dominated by quantum confinement effects.

Molecular orbitals are mathematical functions for describing electron wave-like behavior within a molecule. An electronic band structure can be considered as the ensemble of numerous discrete molecular orbitals (MOs).[6] Therefore similar to MO models, the density of states (DOS) of semiconductor valence bands (VBs) and conduction bands (CBs) are not uniform but usually have the highest density at their centers (See Figure 1-1). For bulk semiconductors, continuous bands are found through the whole DOS of the VB and the CB. The energy gap size between the two bands (*i.e.*, E_g) dominates the electrical and optical behavior of intrinsic semicondu

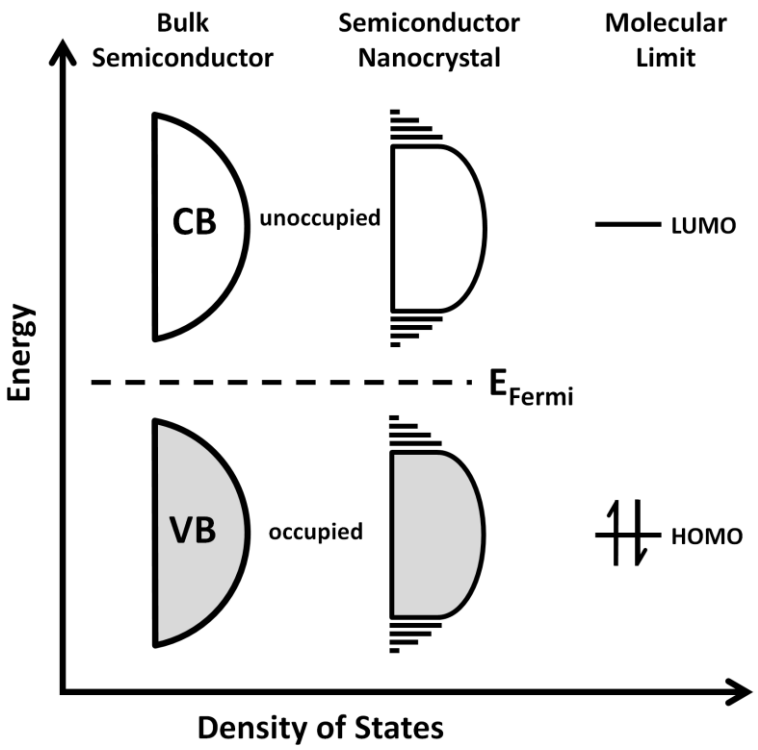

Figure 1-1: A schematic of the density of states (DOS) of a bulk semiconductor, a semiconductor nanocrystal and a molecule. The Fermi level (E_{Fermi}) lies between valence band (VB) and conduction band (CB). Figure adapted from reference 4.

As quantum dots (QDs) decrease in size, there are fewer atoms and orbitals available for bonding and band structure. The center of the bands remains continuous, while the band edges collapse into discrete "MO-like" energy levels and as a result the band gap (E_g) widens. This quantization of the band edges and corresponding increase in band gap energy are the main features of the quantum confinement effect. Changes in the band gap energy (ΔE) can be

estimated using the effective mass approximation (EMA) (Equation 1.1): [7]

$$\Delta E \approx \frac{h^2\pi^2}{2\mu\bar{R}^2} \qquad Equation\ (1.1)$$

where, h is the Planck constant, μ is the reduced mass of electron and hole, and $\bar{R}$ is the average crystal diameter. This elementary model excludes key features such as the Coulomb potential. Kayanuma expanded EMA to include Coulomb interaction (See Equation 1.2):[8]

$$E(R) = E_g + \frac{h^2\pi^2}{2R^2}\left(\frac{1}{m_e^*} + \frac{1}{m_h^*}\right) - \frac{1.786e^2}{\varepsilon_r R} + 0.284\,E_R$$

$$\cdots\cdots\cdots\ Equation\ (1.2)$$

where, E_g is the bulk semiconductor band gap, R is the nanocrystal diameter, e is the electron charge, ε_r is the material relative permittivity, m_e^* and m_h^* are effective masses of the electron and hole in the bulk semiconductor, respectively. E_R is the semiconductor Rydberg energy, which is composition dependent.[8] The EMA shows the contribution of quantum dot size to changes in E_g is proportional to $1/R^2$. As well, the consideration of ε_r and E_R indicates the extent of band gap widening is also dependent upon the semiconductor in question and is reflected in differing properties of QDs of various materials (Figure 1-2).[9]

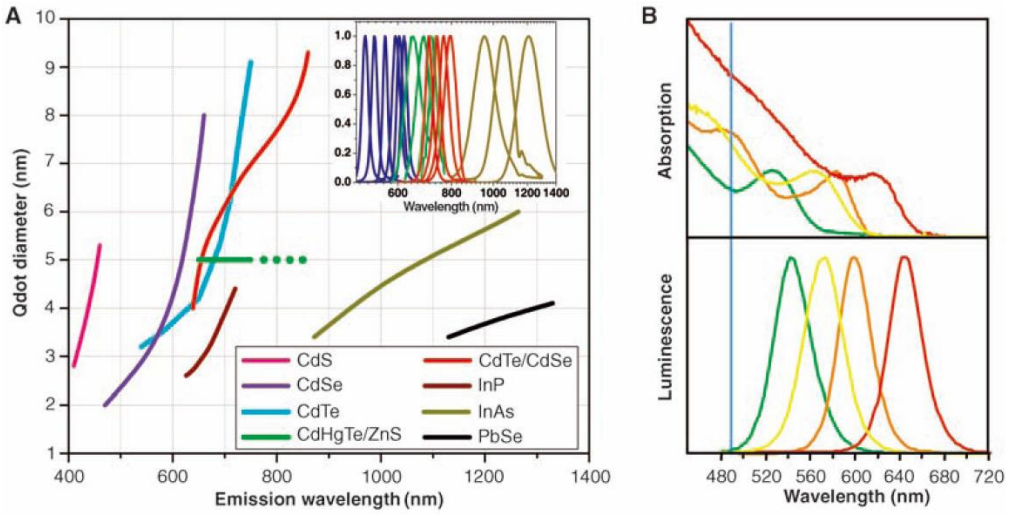

Figure 1-2: (a) The size and composition dependent photoluminescence (PL) emission maxima. (b) Absorption (upper curves) and emission (lower curves) spectra of four CdSe/ZnS QDs. The blue vertical line indicates the 488 nm line of an argon-ion laser, which can be used to efficiently excite all four types of QDs simultaneously. Figure taken from reference 8.

QDs based upon various semiconductors have been prepared and investigated including: II-VI (*e.g.*, CdSe,[10] CdTe,[11] ZnS,[12] HgS[13]), I-VI (*e.g.*, Ag_2S[14]), III-V (*e.g.*, InP,[15] GaAs,[16] GaN[17]), Group IV (*e.g.*, Si,[18] Ge,[19] SiC[20]), as well as I-III-VI (*e.g.*, $CuInSe_2$,[21] $AgInS_2$[22]) ternary systems, and quaternary compounds I-II-IV-VI (*e.g.*, Cu_2ZnSnS_4[23]). Optimized synthetic approaches can even allow the formation of complex structures such as alloys (*e.g.*, Si_xGe_{1-x},[24] $Cu(In_{1-x}Ga_x)S_2$[25]) and core-shell particles (*e.g.*, CdSe-ZnS core-shell[26]).

QDs exhibit unique optoelectronic properties, such as size-tunable band

gap-based PL, narrow emission bands, comparatively wide band gap that allows visible light absorption, excellent photostability (*i.e.*, resistance to photobleaching) and high quantum yield. All of these favorable features of QDs have facilitated applications in photovoltaics,[27-30] light-emitting diodes (LEDs),[31-33] diode lasers,[34-36] sensing,[37-40] bioimaging and labeling,[41-43] as well as photodynamic cancer therapy.[44-45] Despite their facile synthesis, favorable and well-studied optoelectronic properties, restrictions and public perceptions related to heavy metal-based (*e.g.*, Cd and Pb) QDs still exist because of established cytotoxicity and environmental impact of these nanomaterials.[46-48] Unfortunately, these issues are significant barriers to the widespread integration of many quantum dots into commercial products. Thus, the development of alternative non-toxic quantum dots (*e.g.*, silicon) and methods for their derivatization are of paramount importance.

1.2 Silicon Nanocrystals: Properties and Applications

Silicon is the second most abundant element in the Earth's crust and is typically found in nature as an oxide. While some polymorphs exist, the diamond cubic crystal structure is the most thermodynamically stable form of elemental silicon. Most colloidally stable silicon nanocrystals (SiNCs) exhibit

this crystal structure. However very recently examples of SiNCs bearing the BC8 structure were reported (Figure 1-3).[49]

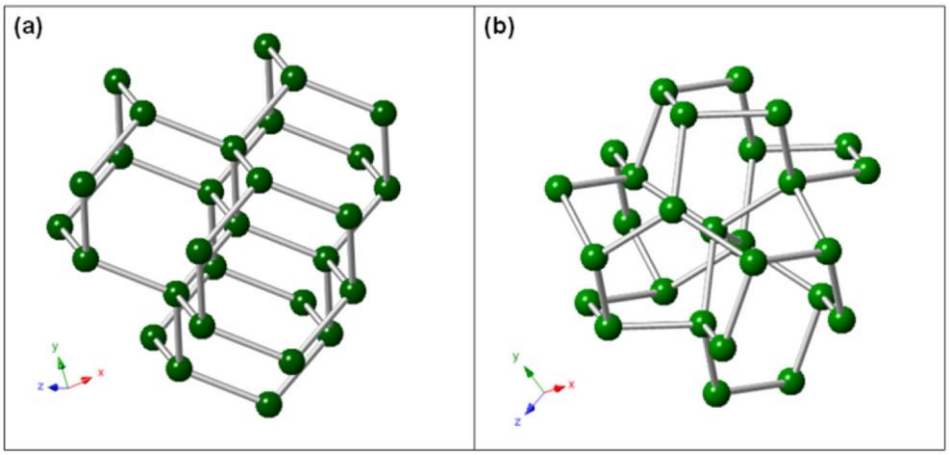

Figure 1-3: View of the crystal structures of (a) cubic diamond Si and (b) Si BC8 structure. Figure taken from reference 48.

The first observation of visible PL from HF-etched porous nanocrystalline silicon was reported by Canham in 1990.[50] Later, similar behavior was noted for various types of SiNCs (*e.g.*, oxide embedded,[51] hydride-terminated,[52] ligand functionalized[53]). Bulk silicon is an indirect band gap semiconductor with an E_g value of 1.12 eV at 300 K. Because the maximum of the VB and the minimum of CB do not occur at the same coordinate in momentum space, the vertical band gap optical transition is forbidden – this made Canham's observation very surprising. There is a longstanding debate about whether the indirect band gap is

retained if the silicon crystal size is significantly reduced (*i.e.*, into the nano-regime). The observations of non-phonon assisted relaxation[54] and nanosecond PL lifetime decay[55-56] suggest ultrasmall silicon crystals (*i.e.*, SiNCs or Si clusters) may possess a direct band gap; this proposal was further supported by computational investigations.[57] However, reports of low-temperature size-selective PL[58] as well an investigation of pressure-dependent SiNC structural and optical properties[59] suggest otherwise.

Similar to other QDs, the band gap energy of SiNCs depends on the changes particle size. SiNC PL has been tuned from the near infrared (NIR) to visible spectral regions through particle size tuning.[60] This size tunability has been attributed to quantum confinement induced changes in the band gap energy and has been confirmed by our group using PL and single particle scanning tunneling spectroscopy measurements (See Figure 1-4).[61]

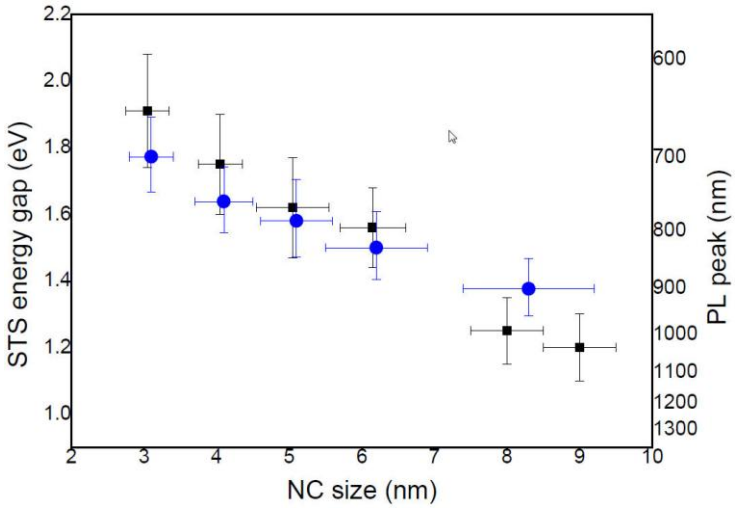

Figure 1-4: Energy gaps determined for dodecyl surface-terminated SiNCs using scanning tunneling spectroscopy (STS, black squares) and PL maxima (blue dots) as a function of particle size. Figure taken from reference 61.

By large, SiNCs are biocompatible.[62-64] When this feature is combined with their relatively high photoluminescent quantum yields (up to 70%[65]), SiNCs become favorable candidates for numerous applications where proof-of-concept applications of luminescent CdSe QDs have been demonstrated, but are no longer appropriate. For example, fluorescent SiNCs are regarded as promising bioimaging materials. Appropriate surface modification (*e.g.*, hydrophilic ligand functionalization,[66] and amphiphilic molecule decoration[67]) renders SiNCs water soluble and suitable for cell labeling. SiNCs are also attractive materials for use in various optoelectronic devices. Early examples of SiNC LEDs have been fabricated and show bright, stable electroluminescence with some colour

tunability from the NIR to yellow spectra region.[68-71] Another attractive application of SiNCs is blending them with active polymers. One example of this involved the physical mixing of alkyl-terminated SiNCs with poly(3-hexylthiophene-2,5-diyl (*i.e.*, P3HT),[72-73] that was in turn applied as an active layer in a prototype solar cell.[74]

1.3 Preparation of Silicon Nanocrystals

SiNCs have been prepared using various physical and chemical approaches. In this section, several mainstream synthetic methods will be presented, including physical top-down methods, gas phase, solution, and solid-state syntheses. The benefits and limitations of each approach will also be discussed briefly.

1.3.1 Physical Methods

Physically breaking down bulk silicon wafers into nanoscale particles offers an apparently straightforward strategy to prepare SiNCs. One top-down approach involves ultrasonication of chemically etched silicon wafers. The varied sizes and shapes of those SiNCs depend on the etching process and sonication time.[75-77] Although highly luminescent SiNCs with somewhat tunable

emission in the visible region can be obtained following filtration,[75] tailorability of NC surface modification remains an issue.

Another common "top-down" approach is mechanical grinding. Fink and co-workers have reported the preparation of silicon nanoparticles using reactive high-energy ball milling (HEBM).[78-79] Compared to ultrasonication, HEBM allows *in situ* ligand functionalization that protects the SiNC surfaces from oxidation and increases solubility.[78] Moreover, particles with different sizes and molecular impurities can be effectively separated by chromatography (See Figure 1-5). However, all SiNCs synthesized by HEBM emit blue light, the origin of which remains unknown.[80-83] Also, chromatographic isolation is not effective to separate particles with different sizes so the particle size tailoring by HEBM remains an issue.

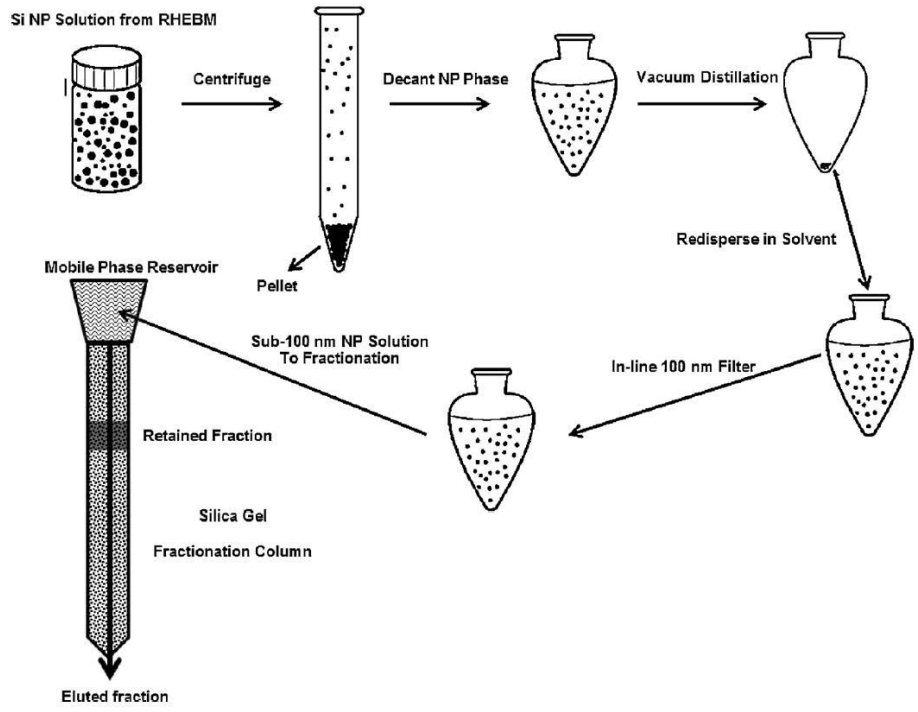

Figure 1-5: Preparation procedure for alkyl-passivated silicon nanoparticles by reactive high energy ball milling and liquid chromatography separation. Figure taken from reference 77.

1.3.2 Gas Phase Synthesis

The first gas phase synthesis of SiNCs using SiH_4 pyrolysis method was reported by a Japanese research group in 1970s,[84] in which a high temperature (1000-1100 ^oC) furnace was used to thermally degrade the silane silicon source. During these syntheses only large particles were reported (30-80 nm). In the 1990s, Huisken and his colleagues employed a pulse CO_2 laser for silane

pyrolysis. The actual reaction temperature was still relatively high (1200 K)[85] and thus a variety of silicon nanostructures were collected,[85-87] ranging from silicon clusters (*i.e.*, 22-100 atoms) and light-emitting SiNCs (diameter ≤ 2.5 nm). Similar approaches were employed by Swihart and his colleagues to prepare SiNCs with tunable visible PLs.[88]

A significant drawback of these early high temperature silane pyrolysis procedures is inevitable particle agglomeration when crystal overgrowing occurs; this leads to broad size distributions.[89] A significant advance was realized with the application of nonthermal plasmas that effectively control particle growth by providing selective local heating while maintaining the gas temperature close to ambient.[89-92] In this approach, the decomposition of silane is initiated by "hot" electrons in the plasma, and results in the formation of small silane clusters (Si_nH_m) that act as seeds for SiNC nucleation.[89] This method affords large quantities of hydride-terminated SiNCs with narrow size distribution,[92] high PL quantum yield (up to 60%[93]) and size-tunable PL through the visible spectrum.[94] In a further optimization of the plasma reactor, an aerosol chamber was added to allow a second step plasma-assisted surface functionalization with various organic ligands.[95] Although no systematic study of the surface modification mechanism has been performed, authors proposed the plasma provides sufficient energy required to induce hydrosilylation.[89]

1.3.3 Solution-Based Synthesis

Solution-based methods have been considered one of the general routes to preparing well-defined nanocrystals.[96] Drawing on known colloidal syntheses of compound semiconductor QDs[11, 97-99] and metal nanoparticles,[100-101] two strategies for SiNCs solution-based preparation have been reported: i) decomposition of silanes/silane derivatives and ii) solvothermal reductions. Silanes (*e.g.*, SiH_4, Si_2H_6, and Si_3H_8) and their derivatives are widely used as silicon sources to form silicon nanowires,[102-103] nanorods,[104-105] and nanoparticles.[106-107] Holmes *et al.* developed supercritical solution methods for preparing small (d~1.5 nm) SiNCs by the thermal decomposition of diphenylsilane in the mixture of octanol and hexane in a pressurized and high temperature system.[108] However, the yield of NCs is low compared with other methods.

The first solvothermal reduction approach was reported by Heath in 1992;[18] this reaction involved reduction of $SiCl_4$ and $RSiCl_3$ using sodium metal (Scheme 1.1). This reaction was carried out over 3 to 7 days in a specialized bomb reactor at 385 ^oC and yielded SiNCs of varied sizes ranging from 5 to 3000 nm. While this procedure did not afford well-defined SiNCs, it was the first report of faceted systems (*vide infra*).

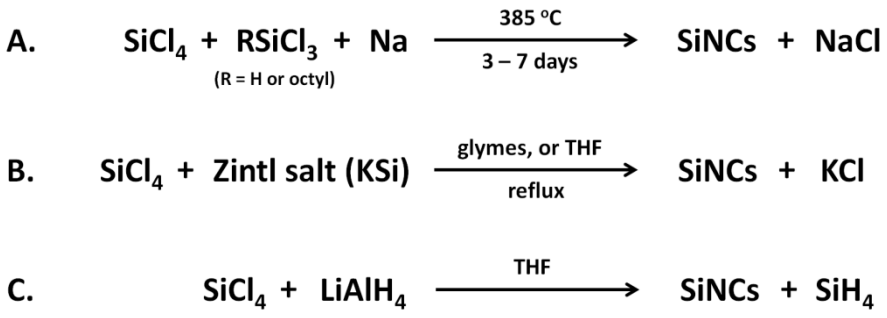

Scheme 1-1: Solvothermal reduction reactions using $SiCl_4$ as a precursor to form SiNCs. The equation is adapted from references 17 and 108.

In the ensuing years, various other reactions employing other reductants (*e.g.*, Zintl salts, Na, $LiAlH_4$) and $SiCl_4$ as silicon source were discovered and investigated. Bley *et al.* used Zintl salt KSi to reduce $SiCl_4$ in glyme or THF solution to yield chloride terminated SiNCs.[109] Strong reducing agents, such as $LiAlH_4$ solution, have also been reported to reduce $SiCl_4$ to form hydride-terminated SiNCs.[110-112] However, generation of substantial quantities of pyrophoric SiH_4 gas during reduction invokes special safety consideration and experiment optimization.[113-114] As well, the claim of the micelles formation in organic solvents is somewhat questionable. Of important note, all SiNCs obtained from these reduction approaches emit blue PL regardless of size, suggesting luminescence is not arising from a band gap transition.[115]

1.3.4 Solid State Synthesis

Generally, solid-state syntheses require silicon rich oxides (SROs) as solid precursors, namely a specific type of solid material with a molecular formula like substoichiometric silica (SiO_x, $0 < x \leq 2$). Under high temperature thermal processing, the disproportionation of SROs yields SiO_2 and elemental silicon.[116-118] The crystallinity and size of Si domains mainly depend on the annealing temperature.[119-120] SROs can be produced by several physical methods, such as ion implantation, co-sputtering and chemical vapor deposition (CVD).[120-123] SRO precursors can also be substituted by molecular or polymeric silicon rich structures with an empirical formula of $(RSiO_{1.5})_n$. They also possess an SiO_x suboxide-like composition similar thermally induced disproportionation occurs and yields SiNCs surrounded by SiO_2.

Compared to physical techniques (*e.g.*, ion implantation), chemical methods such as sol-gel polymerization form SROs with unique benefits including, i) scalable to gram-based quantities of composite, ii) straightforward synthesis without the need for costly infrastructure and toxic or pyrophoric precursors, and iii) the ability to tailor the suboxide composition and form unique inorganic copolymers that offer synthesis of other group 14 materials (*e.g.*, SiC and Si_xGe_{1-x} NCs).[117] To prepare SiNCs, the sol-gel polymers $(HSiO_{1.5})_n$ are formed by the

acid-catalytized sol-gel reaction between $HSiCl_3$ or $HSi(OC_2H_5)_3$.[124-125] During a subsequent annealing step the $(HSiO_{1.5})_n$ polymer decomposes yielding SiO_2 and oxide-embedded SiNCs.

The commercially available hydrogen silsesquioxane ($H_8Si_8O_{12}$, HSQ) is an important presursor for SiNC preparation due to its similar reactivity to those of $(HSiO_{1.5})_n$ sol-gel polymers.[52] The unique cage structure can be synthesized by controlled hydrolysis of trichlorosilane or triethoxylsilane. (Figure 1-6)

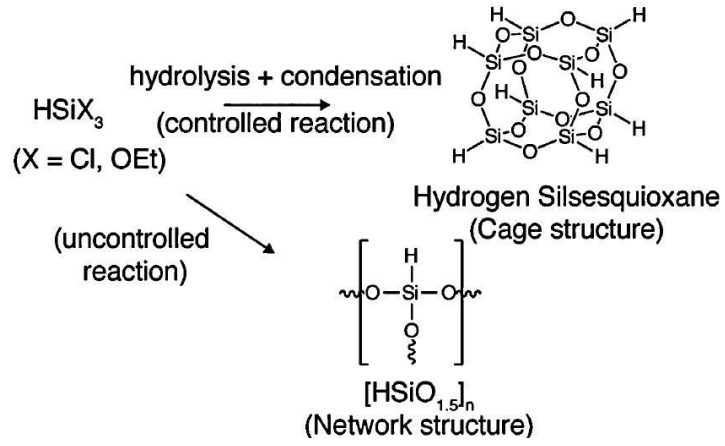

Figure 1-6: Schematic representation of sol-gel reactions of silanes to produce SiNC precursors. Figure taken from reference 116.

HSQ has been widely used to form dielectric layer for microelectronic devices.[126] The first SiNC synthesis using HSQ as precursor was reported by Hessel *et al.*, in which HSQ solid was isolated from a commercially available solution and subsequently heated under slightly reducing atmosphere at 1100 ^oC to produce

SiO_2 embedded SiNCs. SiNCs were further liberated by HF etching, yielding hydride-terminated surface and size-dependent PL (Figure 1-7). The proposed mechanism for the formation of SiNCs includes the formation of various suboxides from crosslinking and rearrangements of HSQ at low temperature, followed by disproportionation for the formation of elemental Si (Scheme 1-2).[52] A follow-up investigation indicated that HSQ was decomposed and formed amorphous Si at low temperature (600 ^{o}C) and started yielding SiNCs when higher temperature was applied (> 900 ^{o}C).[119] As well, one of the immense benefits of this SRO based solid state method is the feasibility of particle size tailoring (from 3 nm to over 20 nm) by simply adjusting annealing temperature from 1100 ^{o}C to 1400 ^{o}C.[60]

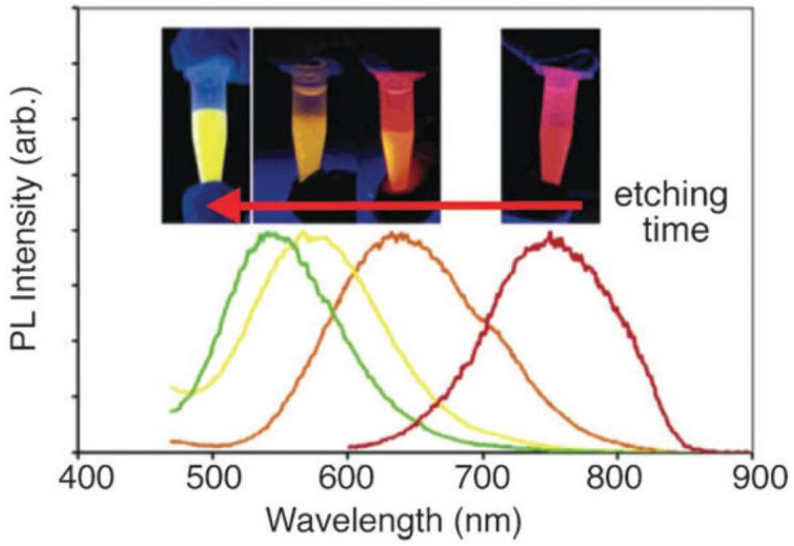

Figure 1-7: PL spectra and corresponding images of hydride-terminated SiNCs toluene solutions after HF etching with various etching time. Figure taken from reference 116.

250 °C – 350 °C

$$2HSiO_{3/2} \longrightarrow H_2SiO_{2/2} + SiO_{4/2} \quad (A)$$

$$H_2SiO_{2/2} + HSiO_{3/2} \longrightarrow SiO_{4/2} + H_3SiO_{1/2} \quad (B)$$

$$H_3SiO_{1/2} + HSiO_{3/2} \longrightarrow SiO_{4/2} + SiH_4 \quad (C)$$

350 °C – 450 °C

$$4HSiO_{3/2} \longrightarrow 3SiO_2 + SiH_4 \quad (D)$$

$$SiH_4 \longrightarrow Si + 2H_2 \quad (E)$$

or cleavage of Si-H + H_2

Scheme 1-2: Stages of HSQ Thermal Degradation in an Inert Atmosphere. Scheme adapted from reference 51.

1.4 Morphology Control of Silicon Nanocrystals

Considerable effort has been aimed at controlling the size and shape of nanomaterials. The reason for this is, it is believed that by controlling the surface energy and electron transfer ability of QDs, their chemical and physical properties can be rationally designed.[96, 127] Morphological control has been widely studied and colloidal synthetic strategies are well-developed for metal and metal oxide nanocrystals, as well as II-VI and III-V QDs. Surfactants, temperature, and concentration allow the preferential growth of crystal faces by altering their relative thermodynamic stability. However, reports applying similar approaches to shape controlled synthesis of silicon nanomaterials are rare and even nonexistent because the strong directional bonding in Si precludes standard colloidal synthesis.

The vast majority of the silicon nanoparticles synthesized by the decomposition of silane or other reduction-functionalization strategies are spherical or pseudospherical (See Section 1.3). The first reported non-spherical freestanding SiNCs was reported by Heath (*vide supra*).[18] In this early report, he noted that larger SiNCs (d~300 nm) exhibited hexagonal morphologies (Figure 1-8).

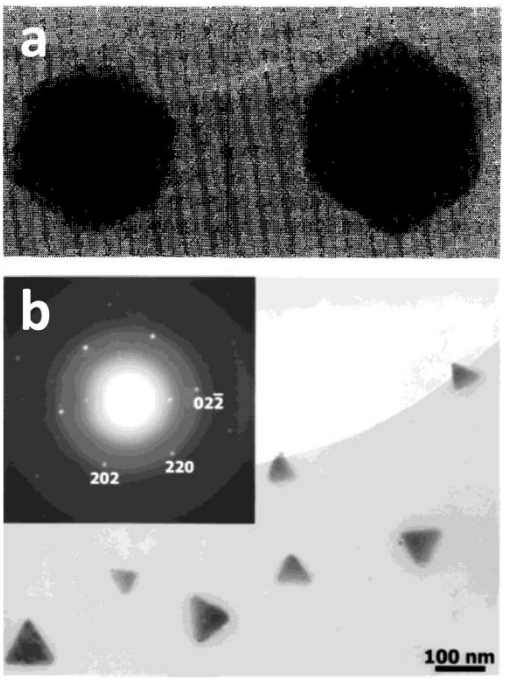

Figure 1-8: (a) Transmission electron microscope (TEM) image of hexagonal SiNCs. The crystals are about 300 nm in diameter. (b) TEM image of tetrahedral SiNCs. Inset: selected-area electron diffraction (SAED) pattern for tetrahedral particles. Figures taken from references 17 and 127.

In 2001, Kauzlarich and colleagues reported tetrahedral shaped SiNCs produced using the solution-based reaction of $SiCl_4$ with sodium naphthalenide in 1,2-dimethoxyethane.[128] These faceted structures were terminated by *n*-butyllithium and had irregular tetrahedral mophologies: edge lengths ranged between 100-150 nm while the height is only 26 nm. Although the surface atomic arrangement is unclear, authors proposed surface atoms were ordered in a (111) plane arrangement based on the assumptions that the surface (111) plane

possesses fewer dangling bonds and exhibits the lowest surface energy compared with those of (110) and (100) planes.[129]

A follow-up study of tetrahedral SiNCs was reported by Barrett *et al.*,[130] in which particles were prepared by thermal decomposition of diphenylsilane in supercritical CO_2 with the presence of various phosphonic acid surfactants. The size and morphology of particles obtained from this reaction included spheres (d = 6 nm), truncated tetrahedrons (d = 15 - 40 nm), and tetrahedrons (d = 50 - 400 nm). Tetrahedrial structures were obtained when surfactants with weaker surface interactions and less intermolecular steric repulsion were employed (Figure 1-9). SAED analysis suggested the tetragonal species exhibted four {111} equivalent facets, consistent with the hypothesis proposed by the Kauzlarich team.[128]

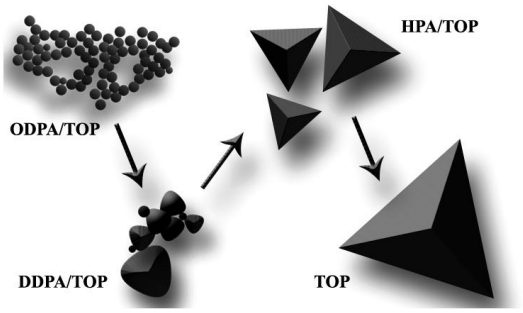

Figure 1-9: A schematic showing the morphological evolution of pseudospherical SiNCs to tetrahedral-shaped crystals (ODPA: octadecylphosphonic acid, DDPA: dodecylphosphonic acid, HPA: hexylphosphonic acid, TOP: trioctylphosphine). Figures taken from reference 129.

Faceted SiNCs can also be produced from gas phase reactions. Bapat *et al.* applied nonthermal low pressure plasma process for the synthesis of well-defined monodisperse silicon nanocubes (30-40 nm, Figure 1-10),[131] which were further used to fabricate single nanoparticle Schottky barrier transistors.[132] The formation mechanism and detailed surface atomic arrangement were not provided. However, a subsequent computational study proposed that the "hydrogen etch" of spherical crystals during nonthermal plasma process could reasonable be expected to induce the formation of a nanocube with a surface atomic arrangement corresponding to the Si(100) plane.[133] In addition, small silicon nanocubes can be also synthesized through solid-state method using HSQ as a precursor.[134] The details of this finding are outlined in Chapter 2 of this thesis.

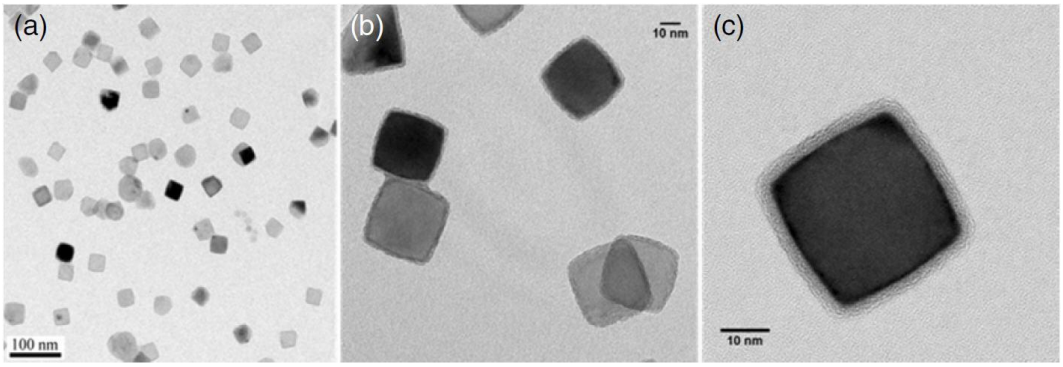

Figure 1-10: TEM images of silicon nanocubes prepared using nonthermal plasma method. Figures taken from reference 131.

1.5 SiNC Surface Hydrosilylation.

When exposed to air or moisture atmosphere, freestanding SiNCs with hydride- or halide-terminated surface are readily oxidized and their optical properties compromized.[68, 135-138] To avoid these undesirable environmental influence and increase compatibility with common solvents, it is important to chemically active Si–H or Si–X (X = Cl, Br) surfaces with more robust alternatives (*e.g.*, Si–O, Si–C). Several important review articles have summarized several well-established strategies for silicon surface modifications.[139-141]

1.5.1 Surface Modification of Silicon

While differences exist when comparing molecular silanes with bulk and nanoscale hydride-terminated silicon surfaces (*e.g.*, bond strength, steric hindrance), the general reactivity of Si–H and Si–X (X = Cl, Br) moieties remains somewhat analogous. However, owing to the fact that SiNC surfaces have a large radius of curvature and are faceted they can differ substantially from flat bulk silicon substrates, it is reasonable that some differences in reactivity would arise — some examples are outlined in Chapter 5 and Reference 141. In this context, many approaches to SiNC surface modification are drawn from their molecular analogues.[142] One approach to modifing silicon surfaces employs a two-step halogenation/alkylation process, in which a freshly-etched hydride-terminated silicon surface is converted to a Si-Cl surface upon reaction with PCl_5, which is subsequently exposed to Grignard reagents to form closely-packed alkyl-terminated surfaces on bulk Si (Scheme 1-3a).[143-145] A similar Grignard-based protocol has been applied to functionalize chloride-terminated SiNCs synthesized by solution-based methods; the resulting alkyl passivated particles show size independent blue PL.[128, 146-147] Another approach to surface modification employed the formation of Si–O linkages *via* controlled oxidation[148-151] or methoxydation.[109] Subsequent hydrolysis with alkoxysilanes introduces a cross-linked siloxane surface (Scheme 1-3a).[152-153]

It is also important to note that several widely reported surface functionalization protocols used for the modification of bulk silicon have not been directly applied to SiNCs (Scheme 1-3b). For example, Villeneuve *et al.* reported benzene derivatives modified bulk silicon surfaces upon reaction with diazonium salts.[154] Similar reactions have also been performed on porous silicon surface by Wang and Buriak.[155] Attempts by researchers in our laboratory to apply this approach to SiNCs have been unsuccessful.

Transition metal compound catalyzed dehydrogenative coupling reactions involving organosilanes are another a common approach to the functionalization of bulk silicon surfaces with organosilanes,[156] but no equivalent reaction has been demonstrated for SiNC system.

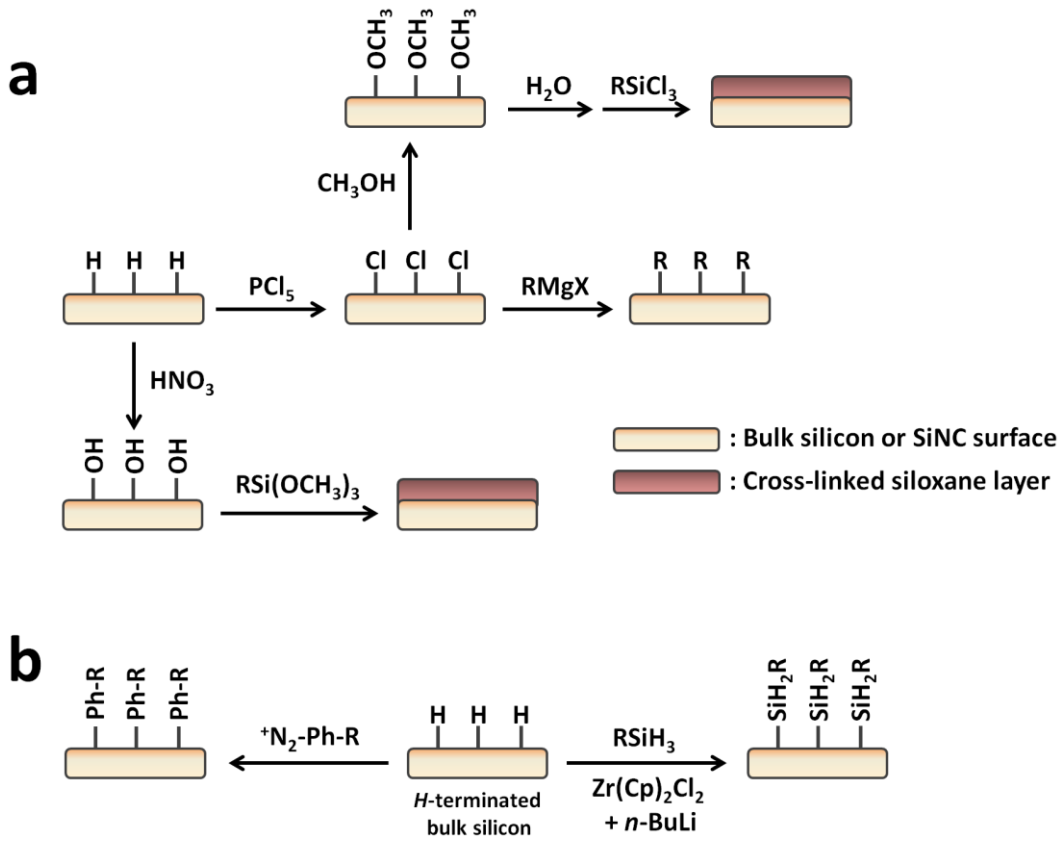

Scheme 1-3: Several major silicon surface modification approaches (hydrosilylation not included). Scheme 1-3a adapted from reference 140.

1.5.2 Silicon Surface Hydrosilylation

Hydrosilylation involves reactions of Si–H bonds with unsaturated functional groups (*e.g.*, multiple bonds of alkenes and alkynes) and produces robust Si–C linkages. It is among the most common silicon surface modification methods because it provides a wide range of surface functionality (*i.e.*, functional group tolerance), it provides effective passivation of surface sites, as well as being

scalable. The first example of Si surface hydrosilylation was reported by Linford and Chidsey in 1993 who demonstrated radical initiated homolytic cleavage of the Si–H bond on a hydride-terminated bulk silicon surface promoted insertion of an alkene.[157] Moran and Carter applied a similar strategy to form densely-packed polystyrene brushes on Si (100).[158] It is also possible to induce Si–H homolytic-cleavage and subsequent hydrosilylation upon heating ($\geq$ 150 ^{o}C)[140] or exposure to appropriate light energy ($\lambda \leq 254$ nm).[159]

Hydrosilylation strategies have been widely employed for bulk and nanoscale Si surface modification. Several proposed mechanisms have appeared and include: i) photoelectron ejection (photoemission),[160] ii) Si–H homolytic cleavage,[159, 161-163] iii) radical assisted hydrosilylation,[164] and iv) exciton mediation.[165] Generally, the active mechanism depends on the conditions employed (*e.g.*, wavelength of the light source).[141] However, in some cases the exact mechanism is difficult (even impossible) to identify (*i.e.*, photoelectron ejection *vs.* exciton mediation[160]).

Hydrosilylation reactions mediated by catalysts, such as platinum complexes[166-167] and Lewis acids (*e.g.*, $EtAlCl_2$)[168] have been applied to functionalize bulk and porous silicon surfaces. Researchers also seek more cost-effective and convenient hydrosilylation approaches. For instance, plasma or microwave activated method have been proven to be highly effective way to

functionalize silicon surface by local heating and the mechanism has been confirmed similar to that of thermal hydrosilylation.[169-170] Recently, Zhong and Bernasek reported a mild sonochemical hydrosilylation method to functionalize silicon surfaces using a simple ultrasonic bath for activation.[171] Several types of unsaturated aliphatic hydrocarbons and bifunctional ligands were tested and their surface attachment was confirmed, although the exact mechanism is currently unclear.

1.5.3 Hydrosilylation on SiNC Surfaces

Many of the above mentioned hydrosilylation methods have been extended to SiNCs. Literature reports suggest functionalization of SiNC surfaces lead to close and often interdigitating packing of surface ligands.[165, 172-175] However, obvious differences exist between hydrosilylation reactions employed in SiNC and bulk silicon systems: these solution-phase hydrosilylation reactions with SiNCs are pseudo-homogeneous and thus experimental details (*e.g.*, particle/ligand ratio, purification steps) require reconsideration. Several types of hydrosilylation reaction have been successfully used and optimized for SiNC surface modification. Thermally induced hydrosilylation is readily applied for grafting hydride-terminated SiNCs with different sizes under the same

temperature range (*e.g.*, ≥ 150 ^{o}C).[60, 67] A similar mechanism drives microwave plasma approach to effectively functionalize SiNCs *via* local heating.[95, 176] UV irradiation has also been shown to be effective for SiNC and porous silicon systems.[165, 174, 177-178] Similarly, their mechanisms can be distinguished by the wavelength of the UV sources. Tilley and his colleagues reported H_2PtCl_6 catalyzed SiNC surface hydrosilylation with various ligands, including allylamine and 1,5-hexadiene, yielding hydrophilic and hydrophobic SiNCs with bright blue PL.[110-111] However, Dasog *et al.* confirmed the spontaneous reaction between R-NH_2 and hydride-terminated surfaces produces blue-emitting particles,[115] suggesting this reaction might not only follow catalytic mechanism. Radical initiator reactions were also tested on SiNC surfaces while few experimental and mechanistic details were provided by authors.[179]

While hydrosilylation has been shown to be effective and efficient for passivating SiNC surface, shortcomings still remain and significantly restrain the applicability of hydrosilylation in particular circumstances. For example, Kelly *et al.* demonstrated the size-dependent reactivity of exciton-driven photochemically induced hydrosilylation on SiNCs, suggesting this approach is not available for bigger particles (*i.e.*, d ≥ 6 nm).[180] Although thermal hydrosilylation is particle size-independent and available for numerous types of ligands, our recent discovery show ligand oligomerization might occur during

thermal reaction, which is undesirable for the goal of producing monomer ligand layer protected SiNCs. Details of the ligand oligomerization will be discussed in chapter 5.

1.6 Thesis Outline

This thesis discusses the optimized synthesis, surface modification, and optical response of SiNCs derived from the disproportionation of hydrogen silsesquioxane (HSQ) under high temperature annealing. Chapter Two focuses on the development of solid state synthesis to achieve size and morphology control of SiNCs. Complex particle shape evolution (from pseudospherical to cube and further faceted structures) and corresponding detailed size crystallinity analysis under prolonged annealing at different high temperature. The proposed formation mechanism of these faceted nanostructures is also discussed.

For preparing nanoparticle/polymer hybrids, one of the big challenges is to achieve even dispersion of small particle inside polymer matrix and meanwhile prevent agglomeration. Chapter Three reports a facile synthesis of highly luminescent SiNC/polystyrene hybrid materials using one-step size-independent radical-initiated hydrosilylation approach. It was noted that the polymer ligands significantly increases SiNC solution processability and provides chemically

resistance to the exposure to strongly basic conditions. To demonstrate these improved properties, a variety of uniform nano- and microscale architectures were synthesized and characterization by electron microscopes.

Thermally induced hydrosilylation mechanism is widely applied for silicon surface modification, because of its particle size independence, relatively high yields and facile purification steps. While chapter four presents a methodical study to critically re-examine this mechanism by functionalizing SiNCs using low temperature (*i.e.*, 100 – 140 °C) thermally induced hydrosilylation approach in argon and air atmosphere. Multiple techniques including X-ray photoelectron spectroscopy and mass spectroscopy show the formation of ligand oligomers on SiNC instead of ligand monolayer passivated surfaces. The results silyl surface radicals generated by either homolytic cleavage of Si-H bonds or oxygen abstraction could initiate ligand oligomerization.

Chapter Five describes an investigation on the origin of nanosecond lifetime decay from yellow/red emitting alkyl-functionalized SiNCs. To perform systematical study, hydride-terminated SiNCs were functionalized by thermal and photochemical hydrosilylation. Detailed photoluminescent properties, such as emission spectrum and lifetime decay, were characterized by single-photon avalanche photodiode and pulse laser system, respectively. The nanosecond lifetime components were only found in samples prepared using photochemical

approach regardless of the size of particles, which is relative to surface defects/traps created by oxidation, which was further confirmed by time dependent photochemical hydrosilylation process.

Finally, Chapter Six outlines the major results from each present chapter and provides a brief outlook of possible future research directions and potential applications of SiNCs.

1.7 References

1. Albrecht, M. G.; Blanchette, C., *J. Electrochem. Soc.* **1998**, *145*, 4019-4025.
2. Kroto, H. W.; Heath, J. R.; O'Brien, S. C.; Curl, R. F.; Smalley, R. E., *Nature* **1985**, *318*, 162-163.
3. Rossetti, R.; Nakahara, S.; Brus, L. E., *J. Chem. Phys.* **1983**, *79*, 1086-1088.
4. Klimov, V. I., *Nanocrystal Quantum Dots*. second edition ed.; CRC Press: 2010; p 485.
5. Goldstein, A. N.; Echer, C. M.; Alivisatos, A. P., *Science* **1992**, *256*, 1425-1427.
6. Hoffmann, R., *Angew. Chem. Int. Ed.* **1987**, *26*, 846-878.
7. Efros, A. L.; Efros, A. L., *Sov. Phys. Semicond.* **1982**, *16*, 772.
8. Trwoga, P. F.; Kenyon, A. J.; Pitt, C. W., *J. Appl. Phys.* **1998**, *83*, 3789-3794.
9. Michalet, X.; Pinaud, F. F.; Bentolila, L. A.; Tsay, J. M.; Doose, S.; Li, J. J.; Sundaresan, G.; Wu, A. M.; Gambhir, S. S.; Weiss, S., *Science* **2005**, *307*, 538-544.
10. Qu, L.; Peng, Z. A.; Peng, X., *Nano Lett.* **2001**, *1*, 333-337.
11. Peng, Z. A.; Peng, X., *J. Am. Chem. Soc.* **2000**, *123*, 183-184.
12. Ohde, H.; Ohde, M.; Bailey, F.; Kim, H.; Wai, C. M., *Nano Lett.* **2002**, *2*, 721-724.
13. Wichiansee, W.; Nordin, M. N.; Green, M.; Curry, R. J., *J. Mater. Chem.* **2011**, *21*, 7331-7336.
14. Zhang, J. Z., *J. Phys. Chem. B* **2000**, *104*, 7239-7253.
15. Talapin, D. V.; Rogach, A. L.; Mekis, I.; Haubold, S.; Kornowski, A.; Haase, M.; Weller, H., *Colloid Surface A* **2002**, *202*, 145-154.
16. Davidson, F. M.; Schricker, A. D.; Wiacek, R. J.; Korgel, B. A., *Adv. Mater.* **2004**, *16*, 646-649.
17. Yang, Y.; Leppert, V. J.; Risbud, S. H.; Twamley, B.; Power, P. P.; Lee, H. W. H., *Appl. Phys. Lett.* **1999**, *74*, 2262-2264.
18. Heath, J. R., *Science* **1992**, *258*, 1131-1133.
19. Muthuswamy, E.; Iskandar, A. S.; Amador, M. M.; Kauzlarich, S. M., *Chem. Mater.* **2012**, *25*, 1416-1422.
20. Zhu, W. Z.; Yan, M., *Mater. Chem. Phys.* **1998**, *53*, 262-266.
21. Tang, J.; Hinds, S.; Kelley, S. O.; Sargent, E. H., *Chem. Mater.* **2008**, *20*, 6906-6910.
22. Mao, B.; Chuang, C.-H.; Wang, J.; Burda, C., *J. Phys. Chem. C* **2011**, *115*, 8945-8954.
23. Steinhagen, C.; Panthani, M. G.; Akhavan, V.; Goodfellow, B.; Koo, B.; Korgel, B. A., *J. Am. Chem. Soc.* **2009**, *131*, 12554-12555.

24. Barry, S. D.; Yang, Z.; Kelly, J. A.; Henderson, E. J.; Veinot, J. G. C., *Chem. Mater.* **2011**, *23*, 5096-5103.
25. Sun, C.; Gardner, J. S.; Long, G.; Bajracharya, C.; Thurber, A.; Punnoose, A.; Rodriguez, R. G.; Pak, J. J., *Chem. Mater.* **2010**, *22*, 2699-2701.
26. Hines, M. A.; Guyot-Sionnest, P., *J. Phys. Chem.* **1996**, *100*, 468-471.
27. Robel, I.; Subramanian, V.; Kuno, M.; Kamat, P. V., *J. Am. Chem. Soc.* **2006**, *128*, 2385-2393.
28. Kamat, P. V., *J. Phys. Chem. C* **2008**, *112*, 18737-18753.
29. Plass, R.; Pelet, S.; Krueger, J.; Grätzel, M.; Bach, U., *J. Phys. Chem. B* **2002**, *106*, 7578-7580.
30. Sargent, E. H., *Nat. Photon.* **2012**, *6*, 133-135.
31. Caruge, J. M.; Halpert, J. E.; Wood, V.; Bulovic, V.; Bawendi, M. G., *Nat. Photon.* **2008**, *2*, 247-250.
32. Anikeeva, P. O.; Halpert, J. E.; Bawendi, M. G.; Bulović, V., *Nano Lett.* **2009**, *9*, 2532-2536.
33. Cho, K.-S.; Lee, E. K.; Joo, W.-J.; Jang, E.; Kim, T.-H.; Lee, S. J.; Kwon, S.-J.; Han, J. Y.; Kim, B.-K.; Choi, B. L.; Kim, J. M., *Nat. Photon.* **2009**, *3*, 341-345.
34. Fafard, S.; Hinzer, K.; Raymond, S.; Dion, M.; McCaffrey, J.; Feng, Y.; Charbonneau, S., *Science* **1996**, *274*, 1350-1353.
35. Haase, M. A.; Qiu, J.; DePuydt, J. M.; Cheng, H., *Appl. Phys. Lett.* **1991**, *59*, 1272-1274.
36. Rafailov, E. U.; Cataluna, M. A.; Sibbett, W., *Nat. Photon.* **2007**, *1*, 395-401.
37. Medintz, I. L.; Clapp, A. R.; Mattoussi, H.; Goldman, E. R.; Fisher, B.; Mauro, J. M., *Nat. Mater.* **2003**, *2*, 630-638.
38. Zhang, C.-Y.; Yeh, H.-C.; Kuroki, M. T.; Wang, T.-H., *Nat. Mater.* **2005**, *4*, 826-831.
39. Willard, D. M.; Van Orden, A., *Nat. Mater.* **2003**, *2*, 575-576.
40. Goldman, E. R.; Medintz, I. L.; Whitley, J. L.; Hayhurst, A.; Clapp, A. R.; Uyeda, H. T.; Deschamps, J. R.; Lassman, M. E.; Mattoussi, H., *J. Am. Chem. Soc.* **2005**, *127*, 6744-6751.
41. Arya, H.; Kaul, Z.; Wadhwa, R.; Taira, K.; Hirano, T.; Kaul, S. C., *Biochem. Bioph. Res. Co.* **2005**, *329*, 1173-1177.
42. Medintz, I. L.; Uyeda, H. T.; Goldman, E. R.; Mattoussi, H., *Nat. Mater.* **2005**, *4*, 435-446.
43. Jaiswal, J. K.; Goldman, E. R.; Mattoussi, H.; Simon, S. M., *Nat. Methods* **2004**, *1*, 73-78.
44. Bakalova, R.; Ohba, H.; Zhelev, Z.; Nagase, T.; Jose, R.; Ishikawa, M.; Baba, Y., *Nano Lett.* **2004**, *4*, 1567-1573.

45. Samia, A. C. S.; Chen, X.; Burda, C., *J. Am. Chem. Soc.* **2003**, *125*, 15736-15737.
46. Oberdörster, G.; Oberdörster, E.; Oberdörster, J., *Environ. Heatlth Perspect.* **2005**, *113*, 823-839.
47. Derfus, A. M.; Chan, W. C. W.; Bhatia, S. N., *Nano Lett.* **2003**, *4*, 11-18.
48. Resch-Genger, U.; Grabolle, M.; Cavaliere-Jaricot, S.; Nitschke, R.; Nann, T., *Nat. Methods* **2008**, *5*, 763-775.
49. Ganguly, S.; Kazem, N.; Carter, D.; Kauzlarich, S. M., *J. Am. Chem. Soc.* **2014**.
50. Canham, L. T., *Appl. Phys. Lett.* **1990**, *57*, 1046-1048.
51. Vinciguerra, V.; Franzò, G.; Priolo, F.; Iacona, F.; Spinella, C., *J. Appl. Phys.* **2000**, *87*, 8165-8173.
52. Hessel, C. M.; Henderson, E. J.; Veinot, J. G. C., *Chem. Mater.* **2006**, *18*, 6139-6146.
53. Sweryda-Krawiec, B.; Cassagneau, T.; Fendler, J. H., *J. Phys. Chem. B* **1999**, *103*, 9524-9529.
54. Kovalev, D.; Heckler, H.; Ben-Chorin, M.; Polisski, G.; Schwartzkopff, M.; Koch, F., *Phys. Rev. Lett.* **1998**, *81*, 2803-2806.
55. Wilcoxon, J. P.; Samara, G. A.; Provencio, P. N., *Phys. Rev. B* **1999**, *60*, 2704-2714.
56. Dohnalova, K.; Poddubny, A. N.; Prokofiev, A. A.; de Boer, W. D. A. M.; Umesh, C. P.; Paulusse, J. M. J.; Zuilhof, H.; Gregorkiewicz, T., *Light Sci Appl* **2013**, *2*, e47.
57. Zhou, Z.; Brus, L.; Friesner, R., *Nano Lett.* **2003**, *3*, 163-167.
58. Nirmal, M.; Brus, L., *Acc. Chem. Res.* **1998**, *32*, 407-414.
59. Hannah, D. C.; Yang, J.; Podsiadlo, P.; Chan, M. K. Y.; Demortière, A.; Gosztola, D. J.; Prakapenka, V. B.; Schatz, G. C.; Kortshagen, U.; Schaller, R. D., *Nano Lett.* **2012**, *12*, 4200-4205.
60. Hessel, C. M.; Reid, D.; Panthani, M. G.; Rasch, M. R.; Goodfellow, B. W.; Wei, J.; Fujii, H.; Akhavan, V.; Korgel, B. A., *Chem. Mater.* **2011**, *24*, 393-401.
61. Wolf, O.; Dasog, M.; Yang, Z.; Balberg, I.; Veinot, J. G. C.; Millo, O., *Nano Lett.* **2013**, *13*, 2516-2521.
62. Jang, H.; Pell, L. E.; Korgel, B. A.; English, D. S., *J. Photoch. Photobio. A* **2003**, *158*, 111-117.
63. Zhong, Y.; Peng, F.; Bao, F.; Wang, S.; Ji, X.; Yang, L.; Su, Y.; Lee, S.-T.; He, Y., *J. Am. Chem. Soc.* **2013**, *135*, 8350-8356.
64. Liu, J.; Erogbogbo, F.; Yong, K.-T.; Ye, L.; Liu, J.; Hu, R.; Chen, H.; Hu, Y.; Yang, Y.; Yang, J.; Roy, I.; Karker, N. A.; Swihart, M. T.; Prasad, P. N., *ACS Nano* **2013**, *7*, 7303-7310.

65. Miura, S.; Nakamura, T.; Fujii, M.; Inui, M.; Hayashi, S., *Phys. Rev. B* **2006**, *73*, 245333.
66. Shiohara, A.; Hanada, S.; Prabakar, S.; Fujioka, K.; Lim, T. H.; Yamamoto, K.; Northcote, P. T.; Tilley, R. D., *J. Am. Chem. Soc.* **2009**, *132*, 248-253.
67. Hessel, C. M.; Rasch, M. R.; Hueso, J. L.; Goodfellow, B. W.; Akhavan, V. A.; Puvanakrishnan, P.; Tunnel, J. W.; Korgel, B. A., *Small* **2010**, *6*, 2026-2034.
68. Pavesi, L.; Dal Negro, L.; Mazzoleni, C.; Franzo, G.; Priolo, F., *Nature* **2000**, *408*, 440-444.
69. Puzzo, D. P.; Henderson, E. J.; Helander, M. G.; Wang, Z.; Ozin, G. A.; Lu, Z., *Nano Lett.* **2011**, *11*, 1585-1590.
70. Maier-Flaig, F.; Rinck, J.; Stephan, M.; Bocksrocker, T.; Bruns, M.; Kübel, C.; Powell, A. K.; Ozin, G. A.; Lemmer, U., *Nano Lett.* **2013**, *13*, 475-480.
71. Maier-Flaig, F.; Kübel, C.; Rinck, J.; Bocksrocker, T.; Scherer, T.; Prang, R.; Powell, A. K.; Ozin, G. A.; Lemmer, U., *Nano Lett.* **2013**, *13*, 3539-3545.
72. Niesar, S.; Fabian, W.; Petermann, N.; Herrmann, D.; Riedle, E.; Wiggers, H.; Brandt, M. S.; Stutzmann, M., *Green* **2011**, *1*, 12.
73. Liu, C.-Y.; Holman, Z. C.; Kortshagen, U. R., *Nano Lett.* **2008**, *9*, 449-452.
74. Kim, S.; Jeon, K.; Lee, J. C.; Swihart, M. T.; Yang, M., *Appl. Phys. Express* **2012**, *5*, 022302.
75. Belomoin, G.; Therrien, J.; Smith, A.; Rao, S.; Twesten, R.; Chaieb, S.; Nayfeh, M. H.; Wagner, L.; Mitas, L., *Appl. Phys. Lett.* **2002**, *80*, 841-843.
76. Nayfeh, M. H.; Barry, N.; Therrien, J.; Akcakir, O.; Gratton, E.; Belomoin, G., *Appl. Phys. Lett.* **2001**, *78*, 1131-1133.
77. Bley, R. A.; Kauzlarich, S. M.; Davis, J. E.; Lee, H. W. H., *Chem. Mater.* **1996**, *8*, 1881-1888.
78. Heintz, A. S.; Fink, M. J.; Mitchell, B. S., *Adv. Mater.* **2007**, *19*, 3984-3988.
79. Heintz, A. S.; Fink, M. J.; Mitchell, B. S., *Appl. Organomet. Chem.* **2010**, *24*, 236-240.
80. Dohnalová, K.; Žídek, K.; Ondič, L.; Kůsová, K.; Cibulka, O.; Pelant, I., *J. Phys. D: Appl. Phys.* **2009**, *42*, 135102.
81. Luppi, M.; Ossicini, S., *Phys. Rev. B* **2005**, *71*, 035340.
82. Lioudakis, E.; Othonos, A.; Nassiopoulou, A. G., *Appl. Phys. Lett.* **2007**, *90*, -.
83. Brewer, A.; von Haeften, K., *Appl. Phys. Lett.* **2009**, *94*, -.
84. Murthy, T. U. M. S.; Miyamoto, N.; Shimbo, M.; Nishizawa, J., *J. Cryst. Growth* **1976**, *33*, 1-7.
85. Ehbrecht, M.; Huisken, F., *Phys. Rev. B* **1999**, *59*, 2975-2985.
86. Ehbrecht, M.; Ferkel, H.; Huisken, F.; Holz, L.; Polivanov, Y. N.; Smirnov, V. V.; Stelmakh, O. M.; Schmidt, R., *J. Appl. Phys.* **1995**, *78*, 5302-5306.

87. Huisken, F.; Ledoux, G.; Guillois, O.; Reynaud, C., *Adv. Mater.* **2002**, *14*, 1861-1865.
88. Li, X.; He, Y.; Talukdar, S. S.; Swihart, M. T., *Langmuir* **2003**, *19*, 8490-8496.
89. Kortshagen, U., *J. Phys. D Appl. Phys.* **2009**, *42*, 113001.
90. Liptak, R. W.; Kortshagen, U.; Campbell, S. A., *J. Appl. Phys.* **2009**, *106*, -.
91. Anthony, R.; Kortshagen, U., *Phys. Rev. B* **2009**, *80*, 115407.
92. Mangolini, L.; Thimsen, E.; Kortshagen, U., *Nano Lett.* **2005**, *5*, 655-659.
93. Jurbergs, D.; Rogojina, E.; Mangolini, L.; Kortshagen, U., *Appl. Phys. Lett.* **2006**, *88*, -.
94. Pi, X. D.; Liptak, R. W.; Nowak, J. D.; Wells, N. P.; Carter, C. B.; Campbell, S. A.; Kortshagen, U., *Nanotechnology* **2008**, *19*, 245603.
95. Mangolini, L.; Kortshagen, U., *Adv. Mater.* **2007**, *19*, 2513-2519.
96. Burda, C.; Chen, X.; Narayanan, R.; El-Sayed, M. A., *Chem. Rev.* **2005**, *105*, 1025-1102.
97. Murray, C. B.; Norris, D. J.; Bawendi, M. G., *J. Am. Chem. Soc.* **1993**, *115*, 8706-8715.
98. Yu, W. W.; Peng, X., *Angew. Chem. Int. Ed.* **2002**, *41*, 2368-2371.
99. Shim, M.; Guyot-Sionnest, P., *J. Am. Chem. Soc.* **2001**, *123*, 11651-11654.
100. Sun, S.; Murray, C. B.; Weller, D.; Folks, L.; Moser, A., *Science* **2000**, *287*, 1989-1992.
101. Puntes, V. F.; Zanchet, D.; Erdonmez, C. K.; Alivisatos, A. P., *J. Am. Chem. Soc.* **2002**, *124*, 12874-12880.
102. Lee, D. C.; Hanrath, T.; Korgel, B. A., *Angew. Chem. Int. Ed.* **2005**, *44*, 3573-3577.
103. Tuan, H.-Y.; Korgel, B. A., *Chem. Mater.* **2008**, *20*, 1239-1241.
104. Heitsch, A. T.; Hessel, C. M.; Akhavan, V. A.; Korgel, B. A., *Nano Lett.* **2009**, *9*, 3042-3047.
105. Lu, X.; Hessel, C. M.; Yu, Y.; Bogart, T. D.; Korgel, B. A., *Nano Lett.* **2013**, *13*, 3101-3105.
106. Littau, K. A.; Szajowski, P. J.; Muller, A. J.; Kortan, A. R.; Brus, L. E., *J. Phys. Chem.* **1993**, *97*, 1224-1230.
107. Fojtik, A.; Henglein, A., *Chem. Phys. Lett.* **1994**, *221*, 363-367.
108. Holmes, J. D.; Ziegler, K. J.; Doty, R. C.; Pell, L. E.; Johnston, K. P.; Korgel, B. A., *J. Am. Chem. Soc.* **2001**, *123*, 3743-3748.
109. Bley, R. A.; Kauzlarich, S. M., *J. Am. Chem. Soc.* **1996**, *118*, 12461-12462.
110. Warner, J. H.; Hoshino, A.; Yamamoto, K.; Tilley, R. D., *Angew. Chem. Int. Ed.* **2005**, *44*, 4550-4554.

111. Tilley, R. D.; Warner, J. H.; Yamamoto, K.; Matsui, I.; Fujimori, H., *Chem. Commun.* **2005**, 1833-1835.
112. Wilcoxon, J. P.; Samara, G. A., *Appl. Phys. Lett.* **1999**, *74*, 3164-3166.
113. Huber, D. L.; Wilcoxon, J. P.; Samara, G. A., *Appl. Phys. Lett.* **2008**, *92*, -.
114. Wilcoxon, J. P.; Samara, G. A.; Provencio, P. N., *Phys. Rev. B* **2007**, *76*, 199903.
115. Dasog, M.; Yang, Z.; Regli, S.; Atkins, T. M.; Faramus, A.; Singh, M. P.; Muthuswamy, E.; Kauzlarich, S. M.; Tilley, R. D.; Veinot, J. G. C., *ACS Nano* **2013**, *7*, 2676-2685.
116. Corriu, R. J. P.; Leclercq, D., *Angew. Chem. Int. Ed.* **1996**, *35*, 1420-1436.
117. Kelly, J. A.; Henderson, E. J.; Veinot, J. G. C., *Chem. Commun.* **2010**, *46*, 8704-8718.
118. Lee, J.-I.; Lee, K. T.; Cho, J.; Kim, J.; Choi, N.-S.; Park, S., *Angew. Chem. Int. Ed.* **2012**, *124*, 2821-2825.
119. Hessel, C. M.; Henderson, E. J.; Veinot, J. G. C., *J. Phys. Chem. C* **2007**, *111*, 6956-6961.
120. Shimizu-Iwayama, T.; Kurumado, N.; Hole, D. E.; Townsend, P. D., *J. Appl. Phys.* **1998**, *83*, 6018-6022.
121. Shimizu-Iwayama, T.; Nakao, S.; Saitoh, K.; Itoh, N., *J. Phys.-Condens. Mat.* **1994**, *6*, L601.
122. Dusane, S.; Bhave, T.; Hullavard, S.; Bhoraskar, S. V.; Lokhare, S., *Solid State Commun.* **1999**, *111*, 431-435.
123. Calleja, W.; Falcony, C.; Torres, A.; Aceves, M.; Osorio, R., *Thin Solid Films* **1995**, *270*, 114-117.
124. Pauthe, M.; Bernstein, E.; Dumas, J.; Saviot, L.; Pradel, A.; Ribes, M., *J. Mater. Chem.* **1999**, *9*, 187-191.
125. Henderson, E. J.; Kelly, J. A.; Veinot, J. G. C., *Chem. Mater.* **2009**, *21*, 5426-5434.
126. Zhuang, Z.; Peng, Q.; Li, Y., *Chem. Soc. Rev.* **2011**, *40*, 5492-5513.
127. Baldwin, R. K.; Pettigrew, K. A.; Ratai, E.; Augustine, M. P.; Kauzlarich, S. M., *Chem. Commun.* **2002**, 1822-1823.
128. Jaccodine, R. J., *J. Electrochem. Soc.* **1963**, *110*, 524-527.
129. Barrett, C. A.; Dickinson, C.; Ahmed, S.; Hantschel, T.; Arstila, K.; Ryan, K. M., *Nanotechnology* **2009**, *20*, 275605.
130. Bapat, A.; Anderson, C.; Perrey, C. R.; Carter, C. B.; Campbell, S. A.; Kortshagen, U., *Plamas Phys. Contr. F.* **2004**, *46*, B97.
131. Bapat, A.; Gatti, M.; Ding, Y.-P.; Campbell, S. A.; Kortshagen, U., *J.*

Phys. D Appl. Phys. **2007**, *40*, 2247.
132. Hawa, T.; Zachariah, M. R., *J. Phys. Chem. C* **2008**, *112*, 14796-14800.
133. Yang, Z.; Dobbie, A. R.; Cui, K.; Veinot, J. G. C., *J. Am. Chem. Soc.* **2012**, *134*, 13958-13961.
134. Kim, S.; Shin, D. H.; Choi, S.-H., *Appl. Phys. Lett.* **2012**, *100*, 253103-3.
135. English, D. S.; Pell, L. E.; Yu, Z.; Barbara, P. F.; Korgel, B. A., *Nano Lett.* **2002**, *2*, 681-685.
136. Kůsová, K.; Cibulka, O.; Dohnalová, K.; Pelant, I.; Valenta, J.; Fučíková, A.; Žídek, K.; Lang, J.; Englich, J.; Matějka, P.; Štěpánek, P.; Bakardjieva, S., *ACS Nano* **2010**, *4*, 4495-4504.
137. Mastronardi, M. L.; Maier-Flaig, F.; Faulkner, D.; Henderson, E. J.; Kübel, C.; Lemmer, U.; Ozin, G. A., *Nano Lett.* **2011**, *12*, 337-342.
138. Yang, L.; Lua, Y.-Y.; Lee, M. V.; Linford, M. R., *Acc. Chem. Res.* **2005**, *38*, 933-942.
139. Buriak, J. M., *Chem. Rev.* **2002**, *102*, 1271-1308.
140. Veinot, J. G. C., *Chem. Commun.* **2006**, *0*, 4160-4168.
141. Buriak, J. M., *Chem. Mater.* **2013**, *26*, 763-772.
142. Brook, M. A., *Silicon in Organic, Organometallic, and Polymer Chemistry*. 1 ed.; Wiley-Interscience: 1999; p 704.
143. Bansal, A.; Li, X.; Lauermann, I.; Lewis, N. S.; Yi, S. I.; Weinberg, W. H., *J. Am. Chem. Soc.* **1996**, *118*, 7225-7226.
144. Bansal, A.; Lewis, N. S., *J. Phys. Chem. B* **1998**, *102*, 1067-1070.
145. Bansal, A.; Lewis, N. S., *J. Phys. Chem. B* **1998**, *102*, 4058-4060.
146. Mayeri, D.; Phillips, B. L.; Augustine, M. P.; Kauzlarich, S. M., *Chem. Mater.* **2001**, *13*, 765-770.
147. Pettigrew, K. A.; Liu, Q.; Power, P. P.; Kauzlarich, S. M., *Chem. Mater.* **2003**, *15*, 4005-4011.
148. Kanemitsu, Y.; Okamoto, S.; Otobe, M.; Oda, S., *Phys. Rev. B* **1997**, *55*, R7375-R7378.
149. Li, S.; Silvers, S. J.; El-Shall, M. S., *J. Phys. Chem. B* **1997**, *101*, 1794-1802.
150. Li, X.; He, Y.; Swihart, M. T., *Langmuir* **2004**, *20*, 4720-4727.
151. Liu, S.-m.; Sato, S.; Kimura, K., *Langmuir* **2005**, *21*, 6324-6329.
152. Zou, J.; Baldwin, R. K.; Pettigrew, K. A.; Kauzlarich, S. M., *Nano Lett.* **2004**, *4*, 1181-1186.
153. Sieval, A. B.; Demirel, A. L.; Nissink, J. W. M.; Linford, M. R.; van der Maas, J. H.; de Jeu, W. H.; Zuilhof, H.; Sudhölter, E. J. R., *Langmuir* **1998**, *14*, 1759-1768.
154. Hunger, R.; Jaegermann, W.; Merson, A.; Shapira, Y.; Pettenkofer, C.;

Rappich, J., *J. Phys. Chem. B* **2006**, *110*, 15432-15441.
155. Wang, D.; Buriak, J. M., *Langmuir* **2006**, *22*, 6214-6221.
156. Li, Y.-H.; Buriak, J. M., *Inorg. Chem.* **2006**, *45*, 1096-1102.
157. Linford, M. R.; Chidsey, C. E. D., *J. Am. Chem. Soc.* **1993**, *115*, 12631-12632.
158. Moran, I. W.; Carter, K. R., *Langmuir* **2009**, *25*, 9232-9239.
159. Terry, J.; Linford, M. R.; Wigren, C.; Cao, R.; Pianetta, P.; Chidsey, C. E. D., *Appl. Phys. Lett.* **1997**, *71*, 1056-1058.
160. Wang, X.; Ruther, R. E.; Streifer, J. A.; Hamers, R. J., *J. Am. Chem. Soc.* **2010**, *132*, 4048-4049.
161. Terry, J.; Linford, M. R.; Wigren, C.; Cao, R.; Pianetta, P.; Chidsey, C. E. D., *J. Appl. Phys.* **1999**, *85*, 213-221.
162. Effenberger, F.; Götz, G.; Bidlingmaier, B.; Wezstein, M., *Angew. Chem. Int. Ed.* **1998**, *37*, 2462-2464.
163. Cicero, R. L.; Linford, M. R.; Chidsey, C. E. D., *Langmuir* **2000**, *16*, 5688-5695.
164. Eves, B. J.; Lopinski, G. P., *Langmuir* **2006**, *22*, 3180-3185.
165. Stewart, M. P.; Buriak, J. M., *J. Am. Chem. Soc.* **2001**, *123*, 7821-7830.
166. Lewis, L. N., *J. Am. Chem. Soc.* **1990**, *112*, 5998-6004.
167. Zazzera, L. A.; Evans, J. F.; Deruelle, M.; Tirrell, M.; Kessel, C. R.; Mckeown, P., *J. Electrochem. Soc.* **1997**, *144*, 2184-2189.
168. Buriak, J. M.; Stewart, M. P.; Geders, T. W.; Allen, M. J.; Choi, H. C.; Smith, J.; Raftery, D.; Canham, L. T., *J. Am. Chem. Soc.* **1999**, *121*, 11491-11502.
169. Boukherroub, R.; Petit, A.; Loupy, A.; Chazalviel, J.-N.; Ozanam, F., *J. Phys. Chem. B* **2003**, *107*, 13459-13462.
170. Petit, A.; Delmotte, M.; Loupy, A.; Chazalviel, J.-N. l.; Ozanam, F. o.; Boukherroub, R., *J. Phys. Chem. C* **2008**, *112*, 16622-16628.
171. Zhong, Y. L.; Bernasek, S. L., *J. Am. Chem. Soc.* **2011**, *133*, 8118-8121.
172. Warner, J. H.; Hoshino, A.; Yamamoto, K.; Tilley, R. D., *Angew. Chem. Int. Ed.* **2005**, *117*, 4626-4630.
173. Tilley, R. D.; Yamamoto, K., *Adv. Mater.* **2006**, *18*, 2053-2056.
174. Kelly, J. A.; Veinot, J. G. C., *ACS Nano* **2010**, *4*, 4645-4656.
175. Weeks, S. L.; Macco, B.; van de Sanden, M. C. M.; Agarwal, S., *Langmuir* **2012**, *28*, 17295-17301.
176. Gupta, A.; Swihart, M. T.; Wiggers, H., *Adv. Funct. Mater.* **2009**, *19*, 696-703.
177. Stewart, M. P.; Buriak, J. M., *Angew. Chem. Int. Ed.* **1998**, *37*, 3257-3260.
178. Clark, R. J.; Dang, M. K. M.; Veinot, J. G. C., *Langmuir* **2010**, *26*,

15657-15664.
179. Nelles, J.; Sendor, D.; Ebbers, A.; Petrat, F.; Wiggers, H.; Schulz, C.; Simon, U., *Colloid Polym Sci* **2007**, *285*, 729-736.
180. Kelly, J. A.; Shukaliak, A. M.; Fleischauer, M. D.; Veinot, J. G. C., *J. Am. Chem. Soc.* **2011**, *133*, 9564-9571.

Chapter 2

Shape Evolution of Faceted Silicon Nanocrystals upon Thermal Annealing in an Oxide Matrix[1]

[1] Portions of this chapter have been published:
1. Yang, Z.; Dobbie, A. R.; Cui, K.; Veinot, J. G. C., *J. Am. Chem. Soc.* **2012,** *134* 13958.
2. Yang, Z.; Dobbie, A. R.; Veinot, J. G. C., *MRS Proceedings* **2013,** DOI: 10.1557/opl.2013.890.

2.1 Introduction

The synthesis of silicon nanoparticles/crystals has been a very active research area over the past 15-20 years, in part because these materials are not readily accessible through the application of standard methods used to prepare traditional nanomaterials. In addition, their biocompatibility (compared to Cd-based quantum dots) makes them particularly appealing.[1-3] In this context, the unique properties of SiNCs make them suitable for nanoelectronic devices, *in-vivo* imaging, and other light-emitting applications.[4-7] It is already established for II-VI and III-V semiconductor nanocrystals that particle shape tailoring leads to exquisite control of material optical and chemical properties.[8-9] Beyond tailoring the characteristics of individual nanocrystals and promoting better understanding of the influence of surface chemistry (*e.g.*, surface reconstruction) on silicon nanocrystal (SiNC) properties, nanocrystal morphology also plays an important role in their assembly into larger extended structures.[10] Nanocrystal superstructures have received much attention because of their tunable particle components.[11-12] The properties of these extended structures show great promise as active systems in many devices.[13] Most superlattice structures consist of assemblies of pseudospherical particles; still, there are benefits offered by achieving other particle shapes.[14-15] For example, nanocubes offer more efficient

space filling compared to their pseudospherical counterparts.

Colloidal synthesis offers a convenient method for tailoring the shapes of II-VI and III-V NCs as well as metal and metal oxide nanoparticles.[16-18] This is made possible by altering/controlling the position of the thermodynamic dissolution/crystallization equilibria.[19] Preferential growth of given crystal faces can be achieved through addition of reagents (*e.g.*, surfactants) that selectively bond to crystal faces thereby altering their relative thermodynamic stability.[19] Similar solution approaches are not readily applied to Group 14 semiconductors (*e.g.*, Si) because of the limited compatibility with solution syntheses.[20-24] Unfortunately, because of the complex chemistry of silicon and its strong directional bonding, shape controlled SiNC synthesis is non-trivial – few examples exist.

The majority of Si and GeNCs, regardless of the synthetic method employed, are spherical or pseudospherical.[25-27] It is possible to use solvothermal techniques and controlled colloidal synthesis to form cube-shaped Ge nanocrystals, but particle dimensions are large (*i.e.*, >80 nm).[28] Silicon tetrahedra with edge the dimensions larger than 100 nm have also been synthesized using solution-based methods.[29-30] In all of these cases, the NCs are comparatively large – this observation is consistent with directed NC growth rather than the equilibrium driven processes implicated in the colloidal phase shape evolution of II-VI and

III-V materials (*vide supra*). Nonthermal plasma processing of silanes is an attractive alternative method for shape controlled SiNC synthesis that produces nanocubes with edge dimensions of approximately 35 nm.[31] Unfortunately, these relatively large nanocrystals are not readily compatible with solution processing and lie outside the size regime where quantum confinement is observed.[32] In this regard, new straightforward methods for preparing small solution compatible crystalline Si nanocubes are appealing.

The Veinot research group has established a facile solid-state method that affords well-defined SiNCs from hydrogen silsesquioxane (HSQ) (Scheme 2-1).[33] High temperature processing in a slightly reducing atmosphere causes HSQ to disproportionate and provides SiNCs embedded in an SiO_2-like matrix. These SiNCs were readily liberated via aqueous HF etching and their surfaces tailored *via* thermal and photochemical hydrosilylation. The size and crystallinity of these nanoparticles could be tailored by defining the processing temperature.[34] Generally, nanoparticles prepared at 1100 ^{o}C were crystalline and high temperature (*i.e.*, > 1400 ^{o}C) annealing led to increased size polydispersity and faceted structures. These observations are consistent with Ostwald ripening arising from increased silicon atom diffusion associated with softening of the oxide matrix (*i.e.*, the solid oxide matrix behaves like a viscous solvent).[35] To date, direct evaluation of the effect of annealing time on NC morphology has largely

been overlooked. In this chapter we report that processing of an oxygen-deficient sol-gel derived precursor using a two-stage high temperature annealing allows formation of Si nanocube and cuboid structures with edge lengths of *ca.* 8–15 nm. SiNC with more complex morphologies (*e.g.*, hexagonal-shape) can be acquired by tailoring the processing temperature and time. We also note the silicon oxide matrix influences the SiNC morphology and size: once the oxide matrix softens at higher temperatures, larger NCs (edge dimension >50 nm) of uncontrolled facetted structures form.

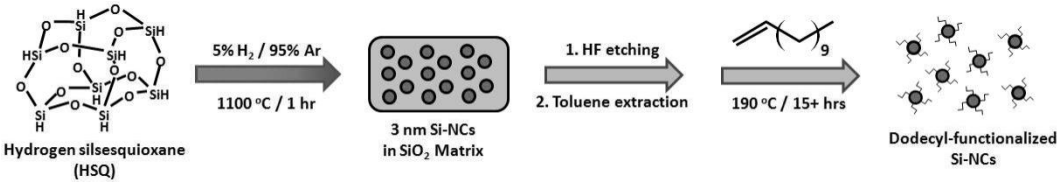

Scheme 2-1: Synthetic pathway from HSQ to dodecyl-functionalized silicon nanocrystals.

2.2 Materials and Methods

2.2.1 Reagents and Materials

Hydrogen silsesquioxane (HSQ, trade name Fox-16, sold commercially as a solution in methyl isobutyl ketone) was purchased from Dow Corning Corp. (Midland, MI). Electronic grade hydrofluoric acid (HF, 49% aqueous solution) was purchased from J. T. Baker. Methanol (reagent grade), toluene (reagent grade), ethanol (reagent grade) and 1-dodecene (97%) were purchased from Sigma Aldrich.

2.2.2 Synthesis and Liberation of SiNCs with Various Morphologies

Silicon Nanocrystal Preparation. The solvent was removed from a HSQ stock solution to yield a white solid. One gram of the HSQ solid was placed in a quartz reaction boat and transferred to a Lindberg Blue tube furnace and heated from ambient to a peak processing temperature of 1100 ℃ at 18 ℃/min in a slightly reducing atmosphere (*i.e.*, 5% H_2/95% Ar). The sample was maintained at the peak processing temperature for predetermined times to obtain particles of different dimensions (*e.g.*, 1 hour, d_{TEM} = 3 nm; 5 hours, d_{TEM} = 4 nm; 24 hours, d_{TEM} = 6 nm). Upon cooling to room temperature, the resulting amber solid was

crushed using an agate mortar and pestle to break up the larger pieces. More complete grinding was achieved using a Burrell Wrist Action Shaker upon shaking with high-purity silica beads for 5 hours. The resulting SiNC/SiO_2-like composite powders were stored in standard glass vials.

The synthesis of larger particles (*i.e.*, d > 6 nm) and SiNCs with non-spherical shapes (*i.e.*, cubes, hexagonal and truncated trigonal prisms) required a second processing step at higher temperature. Following the mortar and pestle grinding (*vide supra*), 0.5 g of SiNC/SiO_2-like composite containing d_{TEM} = 3 nm SiNCs were placed in a high temperature furnace (Sentro Tech Corp.) for further thermal processing in an argon atmosphere. Samples were heated to peak processing temperatures from 1200 − 1400 ℃ at 10 ℃/min and for processing times between 1 and 72 hours. After cooling to room temperature, the resulting brown composites were ground using the identical procedures noted above.

Liberation of SiNCs. Hydride-terminated SiNCs were liberated from the protective SiO_2-like matrix upon etching with HF. Briefly, 0.25 g of ground/shaken composite was transferred to a polyethylene beaker equipped with a Teflon coated stir bar. Three ml of water and 3 ml of ethanol were added under constant mechanical stirring followed by 3 ml of 49 % HF solution. After 1 hour, the color of the etching suspension changed from dark brown to orange/yellow. The liberated, hydride-terminated SiNCs were isolated by

extracting into *ca.* 30 ml (*i.e.*, 3×10 ml) of toluene. The toluene solution was transferred to test tubes and used immediately for thermal hydrosilylation (*vide infra*).

2.2.3 Functionalization and Purification

Following centrifugation at 3000 rpm, the toluene was decanted from the hydride-terminated SiNCs and *ca*. 30 ml dodecene was added. The reaction mixture was transferred to a 100 ml Schlenk flask equipped with Teflon coated stir bar and the flask was evacuated and refilled with argon 3× to minimize the presence of air in the reaction solution. The reaction mixture was left open to an Ar filled manifold at atmospheric pressure, heated to 190 ℃ and was left stirring for a minimum of 15 hours.

Following thermal hydrosilylation, equal volumes (*i.e.*, *ca.* 7.5 ml) of the orange/yellow solution were placed in four centrifuge tubes. Approximately 35 ml of a 1:1 methanol:ethanol mixture was added to each. This procedure resulted in the formation of a cloudy yellow suspension. The precipitate was isolated by centrifugation in a high-speed centrifuge at 14000 rpm for 0.5 hour. The supernatant was decanted and the particles were redispersed in a minimum amount of toluene and re-precipitated by addition of 35 ml of 1:1 methanol:ethanol. The dissolution/precipitation/centrifugation procedure was

repeated twice. Finally, the purified functionalized SiNCs were redispersed in toluene, filtered through a 0.45 μm PTFE syringe filter and stored in vials for further characterization.

2.2.4 Material Characterization and Instrumentation

FTIR spectroscopy was performed on powder samples using a Nicolet Magna 750 IR spectrophotometer. Photoluminescence spectra were obtained by irradiation of a quartz vial containing the sample solution with a 441 nm line of a GaN laser (Wicked Laser Arctic Blue, ~600 mW). Emitted photons were collected with a fiber optic connected to an Ocean Optics USB2000 spectrometer. The spectrometer spectral response was normalized using a black body radiator. X-ray Powder Diffraction (XRD) was performed using an INEL XRG 3000 X-ray diffractometer equipped with a Cu-Kα radiation source (λ = 1.54 Å). Transmission electron microscopy (TEM), selected area electron diffraction (SAED) and energy dispersive X-ray (EDX) analyses were performed using a JEOL-2010 (LaB_6 filament) electron microscope with an accelerating voltage of 200 kV. High resolution TEM (HRTEM) imaging was performed on a JEOL-2200FS TEM instrument with an accelerating voltage of 200 kV. TEM samples of SiNCs and Si nanocubes were drop-coated onto a holey carbon coated copper grid and the solvent was removed under vacuum. TEM and HRTEM

images were processed using ImageJ and Gatan Digital micrograph software, respectively.

2.3 Results and Discussion

The present study shows SiNC size and morphology obtained from thermal processing of HSQ and liberated from the resulting oxide matrix (Scheme 2-2) are dependent upon processing time and temperature. Based upon these observations two complementary processes influence particle size/shape evolution are proposed: 1. Ostwald ripening leads to the formation of larger nanocrystals at the expense of smaller ones. 2. Diffusion and reorganization of silicon atoms to minimize the surface energy yield faceted structures. We also have found that higher temperature (*i.e.,* 1400 ℃) annealing produces large faceted SiNCs, that presumably are the result of the combined influences of oxide matrix softening and melting of the silicon nanodomains which results in ready diffusion of Si atoms.

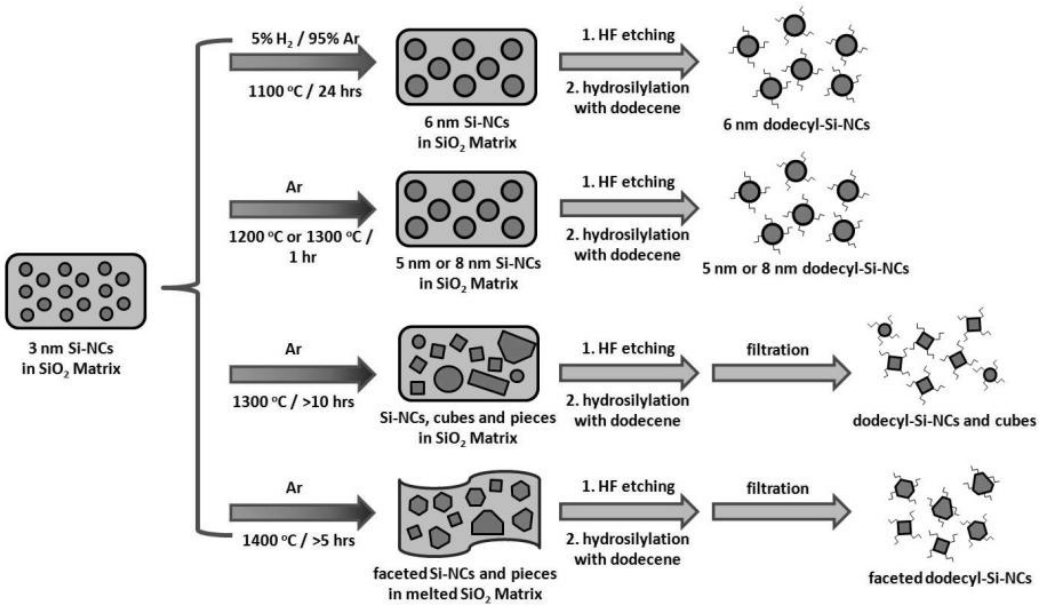

Scheme 2-2: Synthetic pathway from SiNC embedded SiO_2 matrix to functionalized silicon nanocrystals with different sizes and morphologies.

2.3.1 Influence of Processing Time and Temperature

HSQ is heated to 1100^{o}C in a slightly reducing atmosphere (5% H_2/95% Ar) to produce oxide-embedded SiNCs. After cooling to room temperature, the resulting product was transferred to a high temperature furnace and annealed at higher temperatures (*i.e.*, 1200, 1300 or 1400 ^{o}C) in an Ar atmosphere for predetermined times (*i.e.*, between 1 to 72 hours). This second heating step in an inert atmosphere induced morphological evolution of the SiNCs. The resulting orange/brown powder was mechanically ground and subsequently etched using a 1:1:1 HF/ethanol/water solution to liberate hydride-terminated SiNCs and large Si

pieces. The freestanding particles were in turn passivated with dodecene *via* thermal hydrosilylation,[36] purified by centrifugation and redispersed into toluene. Finally, large agglomerates and unfunctionalized particles were removed from the solution using a 0.45 μm PTFE syringe filter to yield a nonopalescent yellow solution.

Table 2-1: Size and Percentage of Nanocube Structures in SiNC Samples.

Temperature (℃)	1100	1100	1200	1200	1200	1300	1300	1300
Time (hour)	1	24	1	24	72	1	10	20
Size (nm)	2.9	7.7	5.1	8.1	6.4	7.9	8.2	12.1
% Cubic	0	0	0	2	15	0	3	71

Temperature (℃)	1300	1300	1350	1350	1350	1350	1350	1350
Time (hour)	24	36	1	2	3	4	5	10
Size (nm)	11.4	8.7	8.0	7.5	7.6	7.4	6.6	7.0
% Cubic	34	7	3	11	16	21	8	7

Table 2-1 summarizes how the SiNC size and shape (*i.e.*, frequency of cube formation) changes with the thermal processing time and temperature. In general, the particle size increases with longer processing time. Extended annealing at 1100 and 1200 ℃ leads to SiNC growth as confirmed by XRD and TEM (Figure 2-1 and 2-2). Peak narrowing in the XRD patterns arising from increased NC size is evident when the annealing time is extended from 1 hour to 24 hours. Consistent with these observations, TEM imaging of liberated

particles indicates SiNCs synthesized at 1100 ℃ are 2.9 ± 0.5 nm after 1 hour processing and 7.6 ± 1.3 nm after 24 hours proceeding. A similar trend was observed for SiNCs annealed at 1200 ℃. SiNCs obtained from etching Si/SiO_2 composites annealed for 1 hour at 1200 ^{o}C exhibited an average diameter of 4.7 ± 0.9 nm; this increased to 7.1 ± 2.0 nm for composites processed for 24 hours. Of important note, the general pseudospherical shape of the SiNCs was maintained even after prolonged annealing (*i.e.*, 24 hours) at 1100 ℃, however for samples processed at 1200 ℃, some faceted NCs were observed (Figure 2-2d).

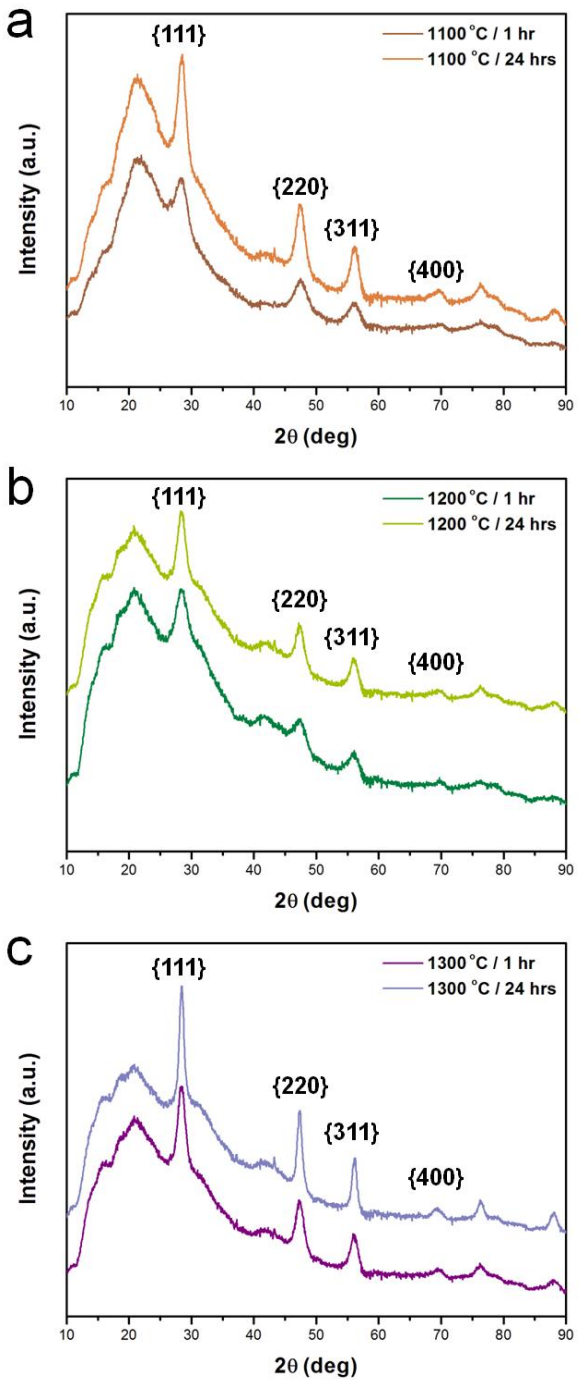

Figure 2-1: XRD patterns of Si/SiO_2 composites formed with various processing temperature and time. Broad peaks at $2\theta = 22°$ may be from the oxide and amorphous silicon.

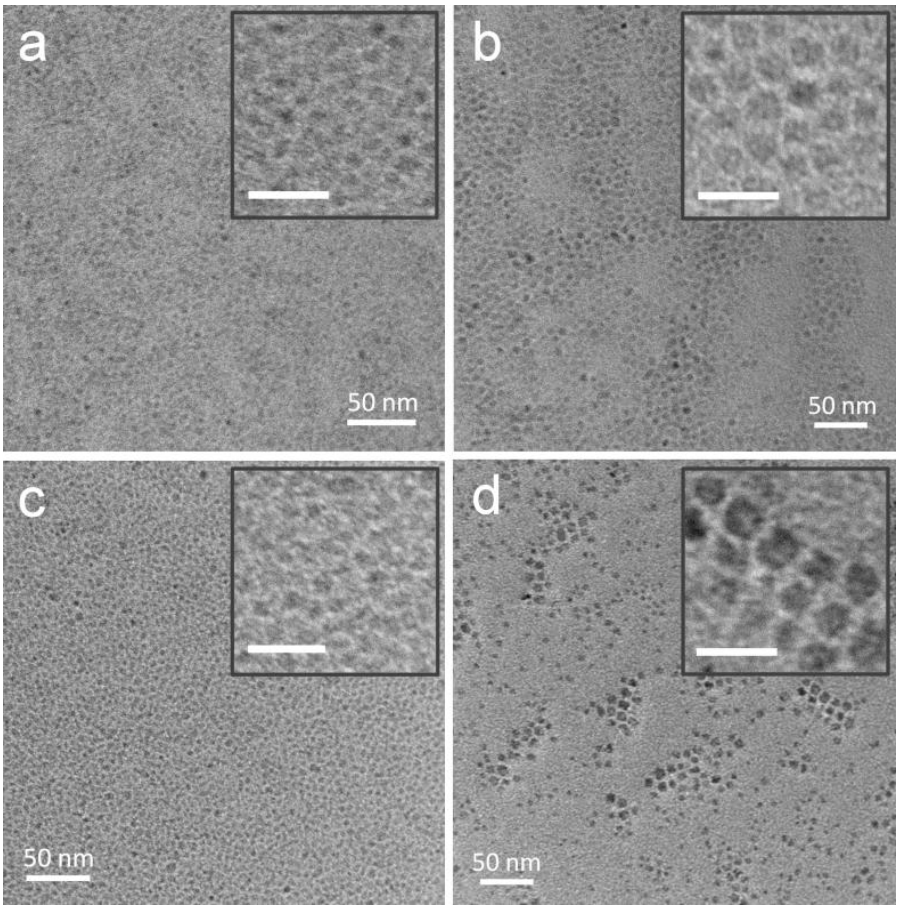

Figure 2-2: TEM images of dodecene functionalized silicon nanocrystals formed at (a) 1100 ℃ for 1 hour; (b) 1100 ℃ for 24 hours; (c) 1200 ℃ for 1 hour; (d) 1200 ℃ for 24 hours. Inset: magnified images of each sample (scale bar = 20 nm).

2.3.2 Silicon Nanocubes and Structure Details

As one would expect, extended heating at 1300 ℃ also leads to evolution of the SiNC morphology (Figure 2-3). Processing for 1 hour yields

pseudospherical NCs with TEM evaluated diameters of 7.9 ± 1.3 nm. Initially, annealing favors pseudospherical particle growth (*i.e.*, 5 hours, d_{TEM} = 8.2 ± 1.3 nm; 10 hours, d_{TEM} = 8.3 ± 1.5 nm; 15 hours, d_{TEM} = 9.1 ± 1.6 nm) (Figure 2-4). A small population of faceted structures (*e.g.*, cubes, cuboids) are noted in TEM images of functionalized SiNCs liberated from the sample processed for 15 hours (Table 2-1). Surprisingly, 70% of the functionalized NCs obtained from samples processed for 20 hours were cubic/cuboid (Figure 2-3c). Infrared spectroscopy indicates the surfaces of the nanocubes are terminated with dodecyl functionalities (Figure 2-5). Toluene solutions of these functionalized nanocubes show extremely weak orange-red PL under 441 nm irradiation (Figure 2-6). It is reasoned that this PL arises from the excitation of small SiNC impurities (*ca.* 3 nm) present in solution;[36] no visible PL from large NCs or cubes was detected. A typical nanocube synthesis employing *ca.* 0.25 g of HSQ yields *ca.* 3.5 mg of functionalized Si nanocubes. Extending the annealing time decreases the yield of cubes: after 24 hours only 34% of the particles are cubes/cuboids, after 36-hour few cuboidal structures remain (*ca*. 7%) and the overall size of particles become slightly smaller (Figure 2-4g).

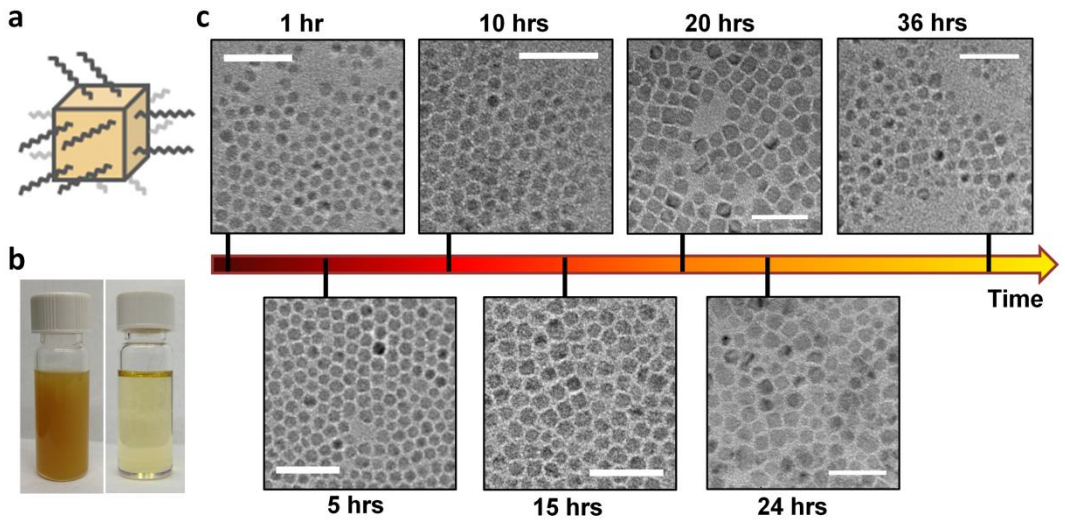

Figure 2-3: Dodecene functionalized Si nanocubes and cuboids (a) Schematic of functionalized Si cubes. (b) Image of functionalized Si nano-cubes and cuboids dispersed in toluene before (left) and after (right) filtration. (c) Annealing time dependent size and shape evolution of SiNCs and Si nanocubes and cuboids formed after annealing at 1300 ℃ as demonstrated by representative TEM images (scale bar = 50 nm).

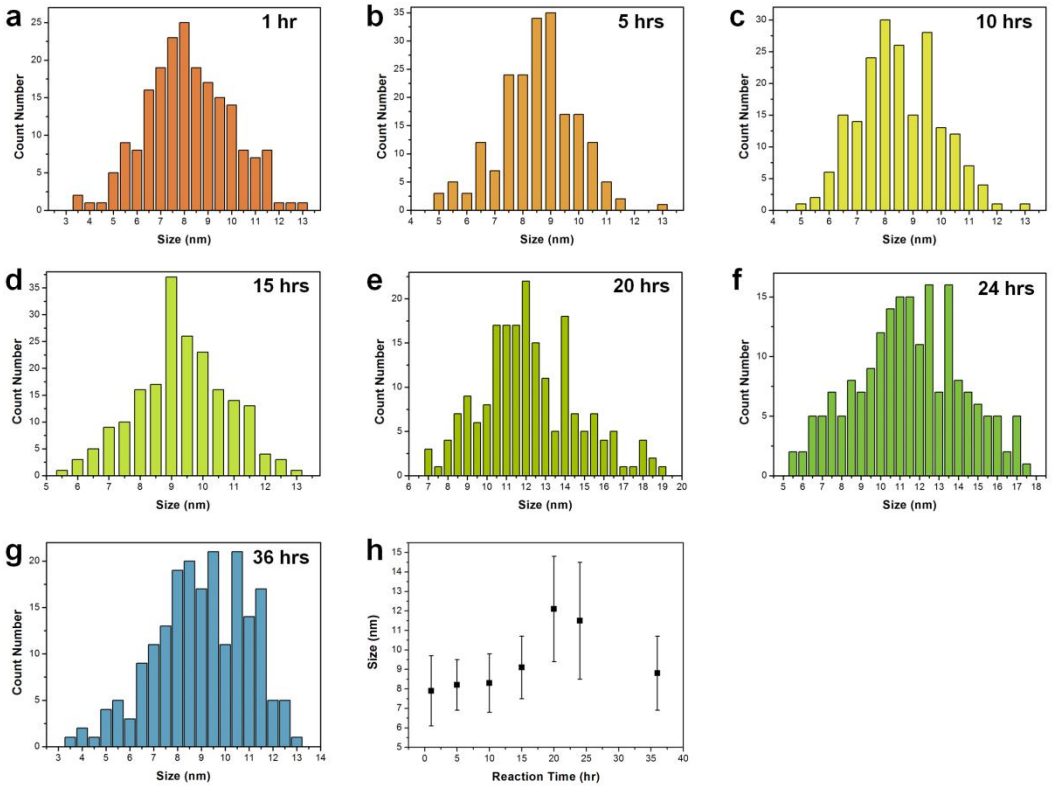

Figure 2-4: Size distribution of dodecene functionalized SiNCs and nanocubes formed at 1300 ℃ with various annealing time: (a) 1 hour, (b) 5 hours, (c) 10 hours, (d) 15 hours, (e) 20 hours, (f) 24 hours and (g) 36 hours. (h) Average sizes of SiNCs and cubes mentioned above. Error bars showing the standard deviation of each samples *(i.e.*, a – g).

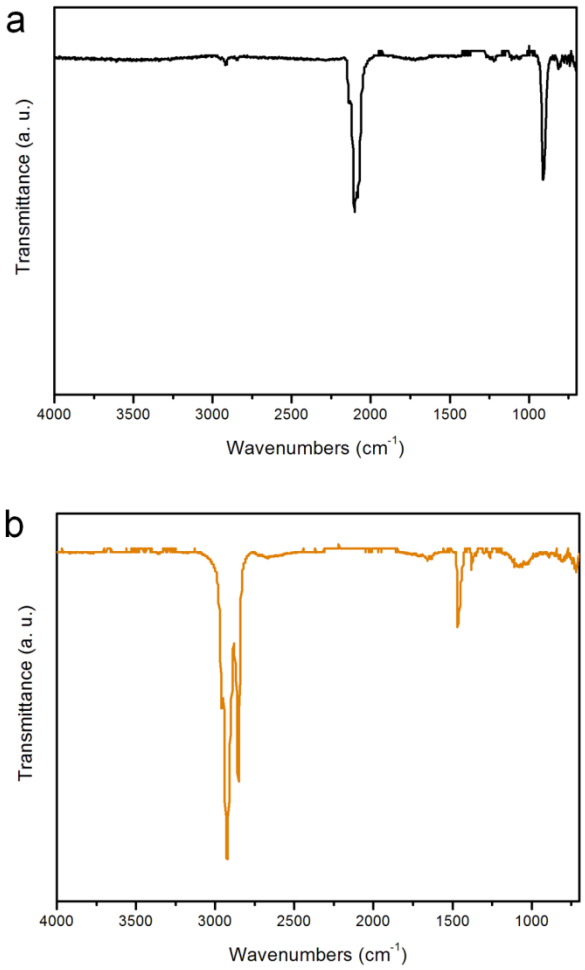

Figure 2-5: FT-IR spectra of hydride-terminated (a) and dodecene-functionalized Si nanocrystals. Vibrations at *ca.* 2100 cm^{-1} and *ca.* 850 cm^{-1} are associated with the Si–H_x stretching and scissoring. The intense absorptions observed at *ca.* 2850 cm^{-1}, *ca.* 2650 cm^{-1} and *ca.* 1460 cm^{-1} are attributed to the alkyl group C–H stretching and bending.

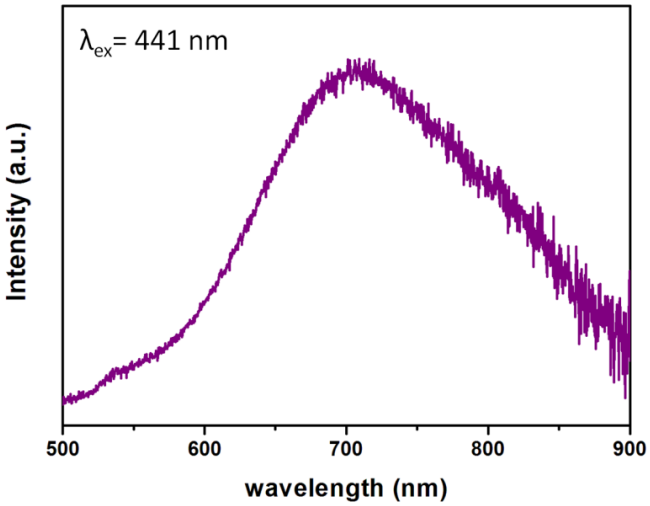

Figure 2-6: Photoluminescence spectrum of silicon nanocubes in toluene.

With this observation in hand, the question arises, why do Si nanocubes form after 20-hour processing? We have already established silicon atoms readily diffuse through the oxide matrix at higher temperatures.[34] It is reasonable, upon prolonged annealing that the silicon atoms will rearrange to form larger faceted structures in order to minimize surface energy.[27] In addition, under this conditions oxygen atoms at the SiO_2/Si interface can also migrate and influence this surface atom arrangement. Tsoukalas *et al.* reported that the silicon and oxygen atom diffusion would be correlated through the formation of silicon domains within SiO_2 matrix.[44] Furthermore, simulations suggest Si nanocubes are thermodynamically favored over their pseudospherical counterparts when their surfaces are passivated.[37] In this context, under the present processing conditions, the SiNC shape is expected to evolve to minimize the surface energy, leading to

the more stable cube geometry with the lowest energy surfaces (*i.e.*, {111} and {110}). As the particles grow with longer annealing, preferential formation of the cube/cuboid shape is lost because the oxide-embedded nanodomains coalesce and yield larger silicon pieces upon removal of the oxide with HF.

Consistent with our proposal of how cubic/cuboidal structures form, we have found the presented approach to be quite general. It is only necessary to identify suitable parameters (*e.g.*, time and temperature). For example, Si nanocubes are also obtained from reactions performed at higher temperatures over shorter times (*e.g.*, 1400 ℃/1 hour, Table 2-1) presumably due to the more rapid diffusion of silicon atoms.

We now turn our attention to a more detailed examination of the Si nanocubes/cuboids obtained after 20 hours of processing at 1300 ℃. Figure 2-7 shows electron microscopy images confirming the size and morphology of the Si nanocubes/cuboids (edge length = 12.1 ± 2.7 nm) with aspect ratios of *ca*. 1–1.5 (Figure 2-8). Selected area electron diffraction (SAED, Figure 2-7e) clearly shows diffraction patterns consistent with diamond structure silicon.[38] A comparison of the intensity ratio for diffraction rings obtained for pseudospherical ($I_{(111)}$:$I_{(220)}$ = 1.58) and nanocube/cuboid ($I_{(111)}$:$I_{(220)}$ = 1.70) is consistent with some oriented growth of the nanocrystals.[38] Energy-dispersive X-ray spectroscopy (EDX, Figure 2-7d) confirms the presence of silicon and a small amount of

oxygen likely arising because of the limited surface passivation by the alkyl chains and air exposure during handling. To determine the "true" shape of the silicon core and eliminate any influence arising from surface ligands, the Si particles were analyzed by high-angle annular dark-field (HAADF) imaging. The HAADF image (Figure 2-7c) highlights Si nanocubes/cuboids with edge dimensions of *ca*. 8–15 nm showing higher Z-contrast indicating an enriched Si content.

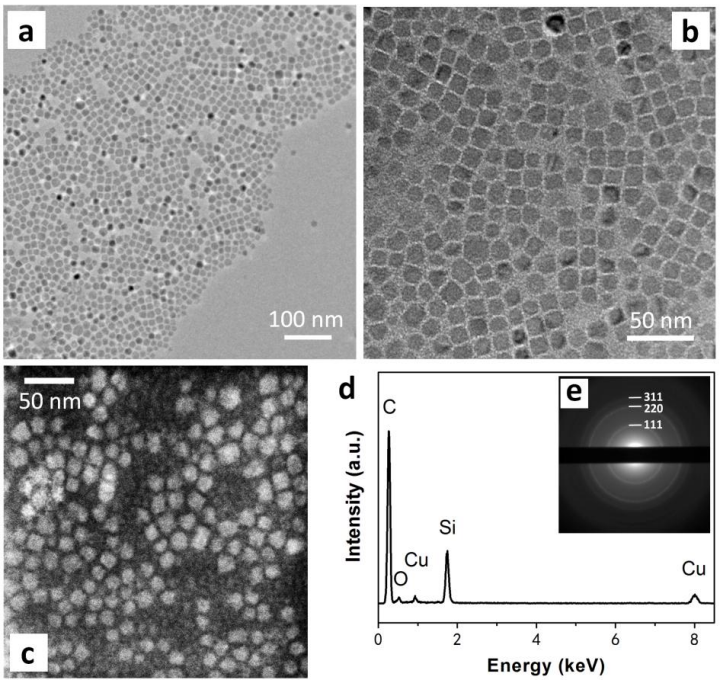

Figure 2-7: Size and morphology analysis of dodecene functionalized silicon nanocubes formed from 1300 ℃ after 20 hours processing. (a, b) Bright-field TEM and (c) HAADF images of SiNCs. (d) EDX spectrum and (e) SAED ring patterns of SiNCs. C and Cu signals arise from the sample grid.

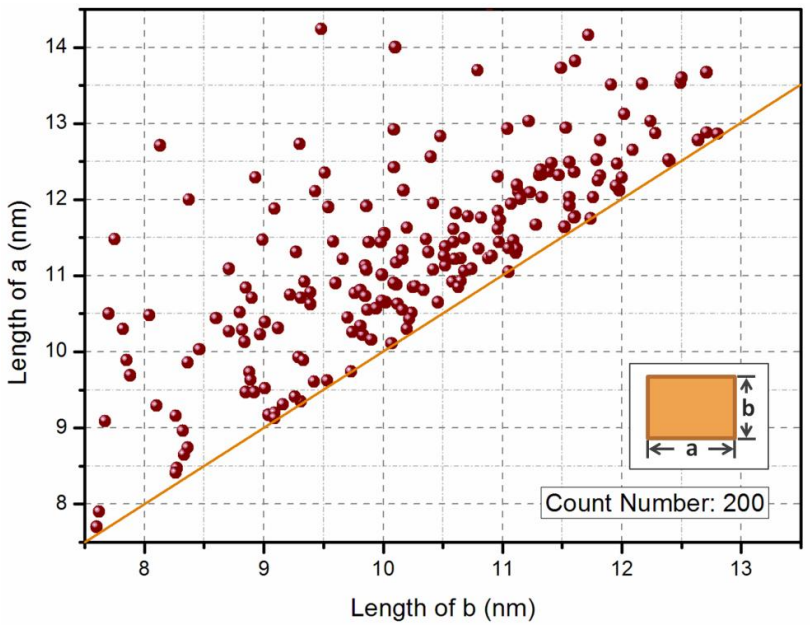

Figure 2-8: Aspect ratio of Si nanocubes formed at 1300 ℃ for 20 h. The dimensions a and b are the lengths of the two sides of nanocubes and the data are acquired from TEM images. Here we define a ≥ b. The orange line represents the situation that a equals b.

High resolution TEM (HRTEM) imaging provided valuable information regarding the crystal structure of the present Si nanocubes/cuboids (Figure 2-9). The periphery of each Si particle is highlighted with a dashed parallelogram for clarity. The majority of the Si nanocuboid structures examined showed lattice fringes spaced by 0.33 nm, perpendicular to the [111] direction and parallel to one of the square edges. This spacing is close to that of the bulk {111} atomic plane spacing (*i.e.*, 0.32 nm) for diamond structured Si.[39-41] A small subset of the

nanocubes showed two sets of lattice fringes (Figure 2-9b), which were assigned specifically to the perpendicular [111] and [11$\bar{1}$] directions with an angle between them of *ca*. 70 º. In addition to those particles that show lattice fringes, a small number of the Si nanocubes/cuboids analyzed lacked any obvious lattice fringes. This observation may be the result of a misalignment of the particles with the electron beam.

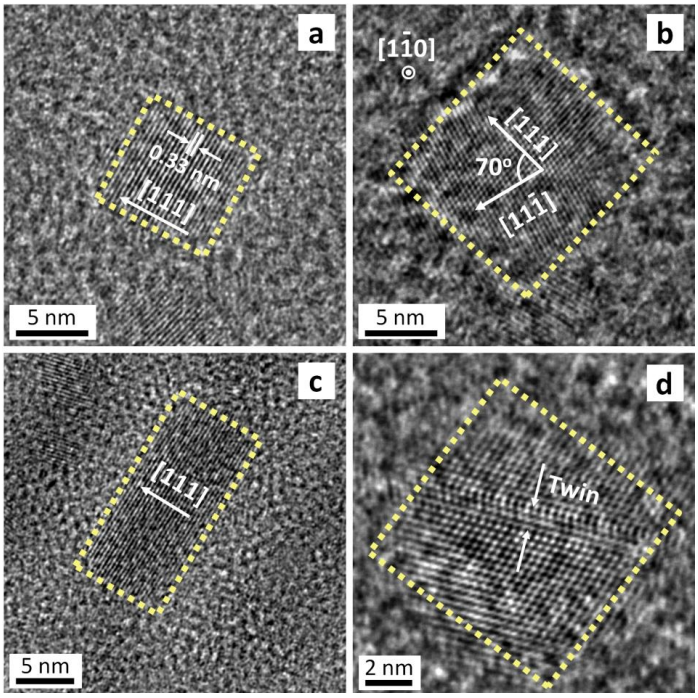

Figure 2-9: HRTEM images of silicon nanocubes/cuboids. (a) A set of lattice fringes perpendicular to [111] direction and parallel to the cube edge. (b) Two sets of fringes perpendicular specifically to the [111] and [11$\bar{1}$] directions. Projection direction parallel to [1$\bar{1}$0] is indicated. (c) A cuboid Si nanoparticle. (d) Twinned structure in one Si cube.

No extended defects (*i.e.*, dislocations or stacking faults) were obvious in the presented analysis. However, we did note a small number of Si cubes displaying twinned structures (Figure 2-9d). Detecting these twinned structures is only possible if the twinning boundary is aligned appropriately (*i.e.*, parallel or almost parallel) with the incident electron beam direction.[42] This orientation dependence may account for the small number of particles displaying twinning that were detected.

From the present observations we conclude that most of the Si nanocubes grow in the [111] direction, while small subpopulations grow in the $[1\bar{1}0]$ and $[11\bar{2}]$ directions (Figure 2-9c). The preferential growth direction may be understood when considering the comparatively low surface energy of the {111} and {110} silicon surfaces versus that of the {100}.[43] In this context, we propose the annealing-induced evolution of the present particles is thermodynamically driven and cubes form in response to the minimization of the surface energy. Simulations involving larger silicon nanocubes suggest the silicon (100) surface should emerge as the preferred surface atom arrangement on each facet because of the slower etch rate in (110) and (111) directions during vapor phase synthesis.[37] However, here silicon cubes with $(1\bar{1}0)$, (111), and $(11\bar{2})$ faces were grown within a silica matrix , consistent with the Si/O interactions influencing the surface atom arrangements. The exact nature of the interactions remains unknown at this

time.

Definitive conclusions regarding the exact ordering of atoms on the nanocube surfaces must be made with caution because surface reconstruction cannot be ignored; this remains a difficult challenge and the subject of ongoing study. Still, it is possible to make some reasonable proposals on the basis of Figure 2-9. Figure 2-9a suggests that two faces of the cubes exhibit the {111} atomic arrangement. Figure 2-9b suggests some may prefer {110} ordering based upon the electron beam direction. In this regard, we propose the resulting nanocubes are terminated by $(1\bar{1}0)$, (111), and $(11\bar{2})$ surfaces. Figure 2-10 illustrates how a cubic structure can be derived from a three-dimensional model of diamond lattice silicon by terminating the structure by these crystal faces. More detailed surface crystallographic studies are the subject of ongoing investigations.

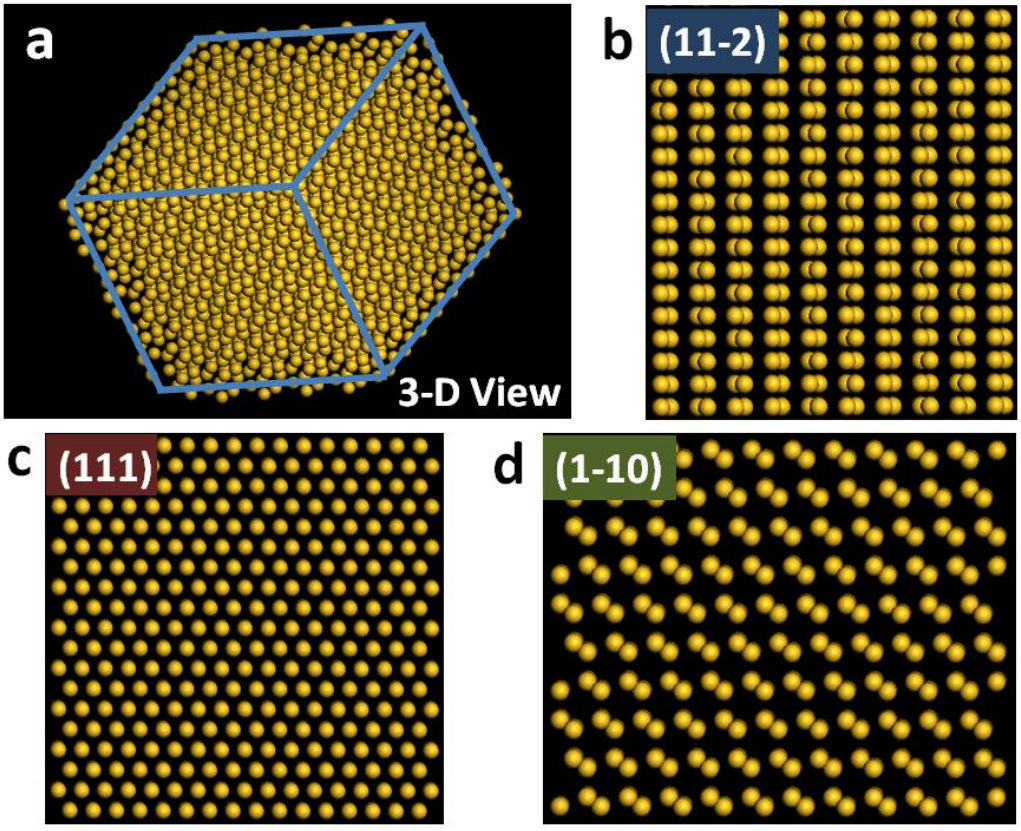

Figure 2-10: Schematic representation of a silicon nano-cuboid structure terminated by $(1\bar{1}0)$-(111)-$(11\bar{2})$ faces. (a) Three dimensional view. (b, c, d) Surface atom arrangement on each face. This figure was prepared using the software Material Studio ver. 4.3 (Accelrys Inc.)

2.3.3 Formation of Large Faceted SiNCs

Raising the processing temperature to 1200 ℃ yielded faceted NCs when samples were processed for 24 hours (Figure 2-11a). The formation of nanocubes was also noted after prolonged annealing (*i.e.*, 1200 ℃ for 72 hours,

Figure 2-11b). These observations suggest the relative stability of Si crystal planes/faces are influencing the particle shape. When the processing temperature was increased to 1300 ℃, surface self-optimization became more obvious. While it requires at least 15 hours for the formation of a small amount of faceted NCs, similar nanostructures were obtained only after 1-hour annealing at 1350 ℃ but only a maximum of 21% nanocubes could be achieved.

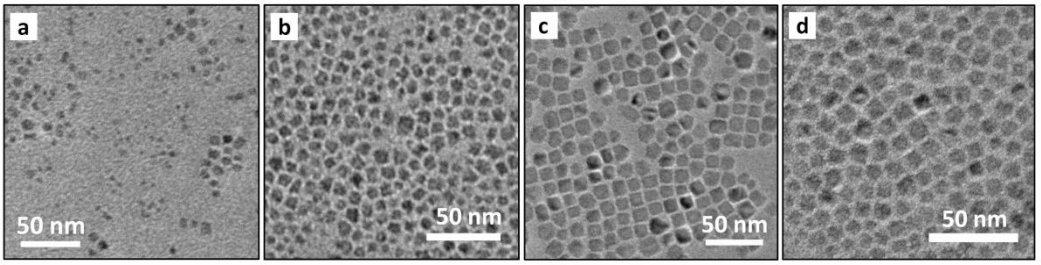

Figure 2-11: TEM images of dodecyl-functionalized faceted silicon nanocrystals formed from prolonged high temperature annealing: (a) 1200 ℃/24 hours, (b) 1200 ℃/72 hours, (c) 1300 ℃/20 hours, and (d) 1350 ℃/4 hours.

Silicon atoms are expected to diffuse and rearrange readily at 1400 ℃ because the oxide matrix and Si nanodomains NCs are expected to soften or even melt (SiO_2 softening point: *ca.* 1200 ℃, Si mp = 1414 ℃). As a result, substantial morphology evolution of SiNCs is observed (Figure 2-12a−c). After only 1-hour annealing a notable population of Si nanocubes (24%) was detected

suggesting the oxide matrix is likely still intact and is still influencing the particle shape. The average size (edge dimension ~ 10 nm) is larger than those formed at lower temperatures, but a comparatively narrow size distribution remains consistent with a softened matrix and easier Si diffusion. No cubic structures were observed upon processing for 24 hours and only larger faceted structures (edge dimensions >20 nm) including, cuboid, hexagonal- and truncated trigonal-shapes were detected Figure (2-12d). These observations suggest substantial Si diffusion and that these structures may have similar surface energy. Clearly, controlling silicon nanoparticle morphology within an oxide matrix is complicated by the softening of the oxide matrix which is expected to influence SiNC size/shape upon high temperature annealing.[27] This is the subject of ongoing investigation in our laboratory.

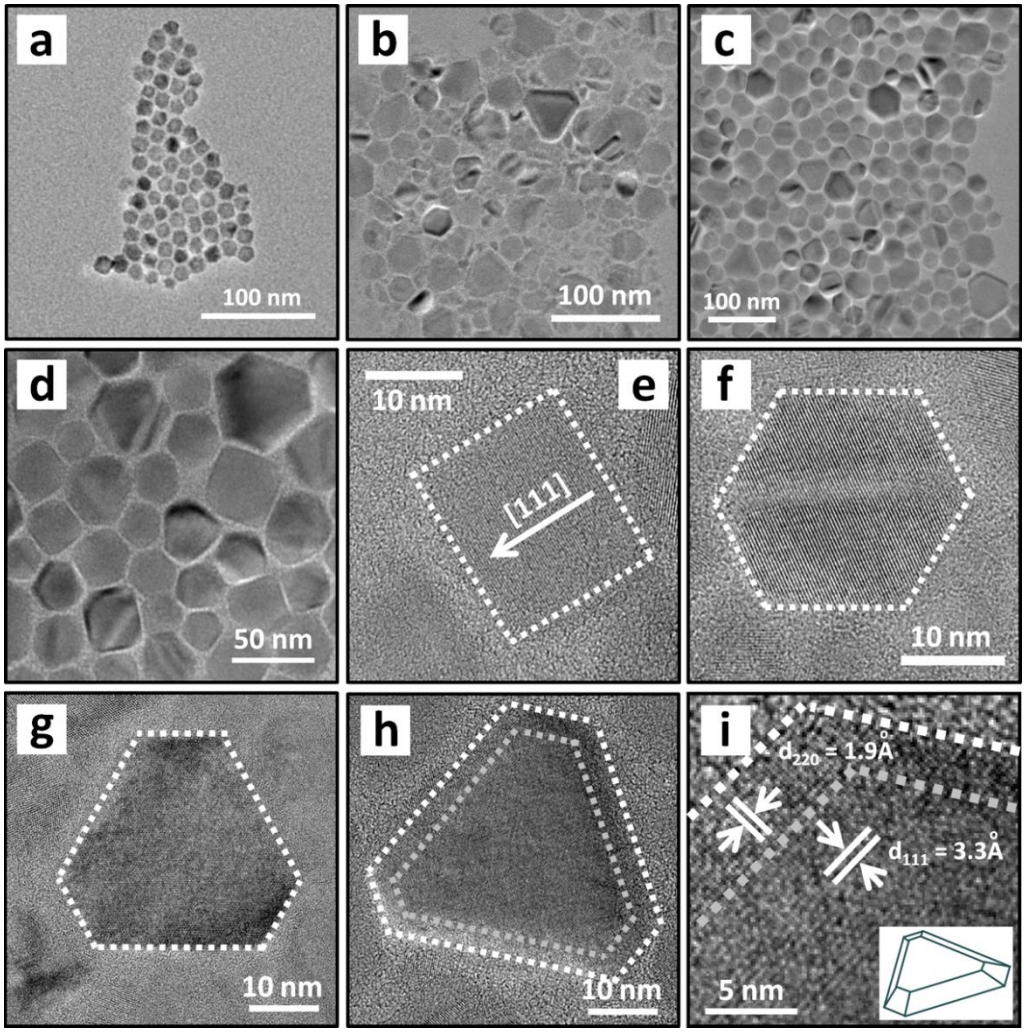

Figure 2-12: Bright-field TEM and HRTEM images of faceted SiNCs formed from 1400 ℃ after (a) 1-hour, (b) 24-hour, and (c, d) 48-hour annealing. Several types of faceted structures are shown: (e) cuboid, (f) hexagon, and (g), (h) truncated trigonal platelets. (i) zoom-in image of (h) showing two sets of fringes Inset: hypothetical structure of the truncated trigonal platelets.

Despite the complexity of these processes and their influences on the particle size and shape evolution, valuable information can be obtained from

straightforward observation of the particles obtained from various reaction conditions. At comparatively low temperatures (*i.e.*, ≤1350 ℃) the rigid structure of the oxide matrix is maintained and the SiNC size does change dramatically with increased processing time. In contrast, when the integrity of the SiO_2-like matrix, that effectively separates nucleation from growth when syntheses are performed at lower temperatures, is somewhat compromised at *ca.* 1400 ℃ comparatively rapid diffusion of Si atoms occurs and particle growth and shape evolution are promoted.

HRTEM images of Si particles obtained upon processing at 1400 ℃ are shown in Figure 2-12e−i. Larger nanocubes are formed at 1400 ℃ and they tend to grow in the [111] direction, consistent with the samples from the 1300 ℃ reaction [16]. In addition, hexagonal and truncated-trigonal NCs with {111} bases and facets were found, consistent with the expected tetrahedral symmetry. The growth direction appears to be dominated by the thermodynamic stability of the {111}. Compared with previously reported large faceted SiNCs (edge dimension >100 nm),[22, 29-30] it is possible that these relatively small faceted particles may finally grow larger with similar morphologies if prolonged annealing is applied.

2.4 Conclusions

In this chapter I have demonstrated annealing time and temperature can affect the morphology of SiNCs formed during the disproportionation of HSQ. In doing so, I have found it is possible to exploit the relative thermodynamic stabilities of the Si crystal faces to induce silicon nanocrystal shape evolution in an oxide matrix. At higher temperatures, the silicon nanodomains melt and surface atom diffusion occurs more readily and produces complex nanostructures. Such oxide-embedded Si cubes can be liberated without compromising their shape and subsequently passivated using thermochemical functionalization. Furthermore, the oxide matrix plays an important role in controlling NC sizes upon annealing, while its softening would induce the formation of larger faceted structure with relative lower surface energy.

2.5 References

1. Jang, H.; Pell, L. E.; Korgel, B. A.; English, D. S., *J. Photochem. Photobiol. A* **2003**, *158*, 111-117.
2. Zhong, Y.; Peng, F.; Bao, F.; Wang, S.; Ji, X.; Yang, L.; Su, Y.; Lee, S.-T.; He, Y., *J. Am. Chem. Soc.* **2013**, *135*, 8350-8356.
3. Liu, J.; Erogbogbo, F.; Yong, K.-T.; Ye, L.; Liu, J.; Hu, R.; Chen, H.; Hu, Y.; Yang, Y.; Yang, J.; Roy, I.; Karker, N. A.; Swihart, M. T.; Prasad, P. N., *ACS Nano* **2013**, *7*, 7303-7310.
4. Maltzahn, G. v.; Park, J. H.; Lin, K. Y.; Singh, N.; Schwöppe, C.; Mesters, R.; Berdel, W. E.; Ruoslahti, E.; Sailor, M. J.; Bhatia, S. N., *Nat. Mater.* **2011**, *10*, 545.
5. Holman, Z. C.; Liu, C.; Kortshagen, U. R., *Nano Lett.* **2010**, *10*, 2661.
6. Erogbogbo, F.; Yong, K. T.; Roy, I.; Xu, G. X.; Prasad, P. N.; Swihart, M. T., *ACS Nano* **2008**, *2*, 873.
7. Puzzo, D. P.; Henderson, E. J.; Helander, M. G.; Wang, Z.; Ozin, G. A.; Lu, Z., *Nano Lett.* **2011**, *11*, 1585.
8. Burda, C.; Chen, X.; Narayanan, R.; El-Sayed, M. A., *Chem. Rev.* **2005**, *105*, 1025.
9. Zhuang, Z.; Peng, Q.; Li, Y., *Chem. Soc. Rev.* **2011**, *40*, 5492.
10. Kalsin, A. M.; Fialkowski, M.; Paszewski, M.; Smoukov, S. K.; Bishop, K. J. M.; Grzybowski, B. A., *Science* **2006**, *312*, 420-424.
11. Redl, F. X.; Cho, K. S.; Murray, C. B.; O'Brien, S., *Nature* **2003**, *423*, 968-971.
12. Shevchenko, E. V.; Talapin, D. V.; Kotov, N. A.; O'Brien, S.; Murray, C. B., *Nature* **2006**, *439*, 55-59.
13. Talapin, D. V.; Lee, J.; Kovalenko, M. V.; Shevchenko, E. V., *Chem. Rev.* **2010**, *110*, 389.
14. Demortière, A.; Launois, P.; Goubet, N.; Albouy, P. A.; Petit, C., *J. Phys. Chem. B* **2008**, *112*, 14583.
15. Stebe, K. J.; Lewandowski, E.; Ghosh, M., *Science* **2009**, *325*, 159.
16. Jana, N. R.; Chen, Y.; Peng, X., *Chem. Mater.* **2004**, *16*, 3931-3935.
17. Jun, Y.-w.; Choi, J.-s.; Cheon, J., *Angew. Chem., Int. Ed.* **2006**, *45*, 3414-3439.
18. Tao, A. R.; Habas, S.; Yang, P., *Small* **2008**, *4*, 310-325.
19. Burda, C.; Chen, X.; Narayanan, R.; El-Sayed, M. A., *Chemical Reviews* **2005**, *105*, 1025-1102.
20. Littau, K. A.; Szajowski, P. J.; Muller, A. J.; Kortan, A. R.; Brus, L. E., *J. Phys. Chem.* **1993**, *97*, 1224-1230.

21. Fojtik, A.; Henglein, A., *Chem. Phys. Lett.* **1994**, *221*, 363-367.
22. Heath, J. R., *Science* **1992**, *258*, 1131-1133.
23. Veinot, J. G. C., *Chem. Commun.* **2006**, *0*, 4160-4168.
24. Warner, J. H.; Hoshino, A.; Yamamoto, K.; Tilley, R. D., *Angew. Chem., Int. Ed.* **2005**, *44*, 4550-4554.
25. Pettigrew, K. A.; Liu, Q.; Power, P. P.; Kauzlarich, S. M., *Chem. Mater.* **2003**, *15*, 4005.
26. Warner, J. H.; Hoshino, A.; Yamamoto, K.; Tilley, R. D., *Angew. Chem., Int. Ed.* **2005**, *44*, 4550.
27. Hessel, C. M.; Reid, D.; Panthani, M. G.; Rasch, M. R.; Goodfellow, B. W.; Wei, J.; Fujii, H.; Akhavan, V.; Korgel, B. A., *Chem. Mater.* **2012**, *24*, 393.
28. Wang, W.; Huang, J.; Ren, Z., *Langmuir* **2005**, *21*, 751.
29. Baldwin, R. K.; Pettigrew, K. A.; Garno, J. C.; Power, P. P.; Liu, G.; Kauzlarich, S. M., *J. Am. Chem. Soc.* **2002**, *124*, 1150.
30. Barrett, C. A.; Dickinson, C.; Ahmed, S.; Hantschel, T.; Arstila, K.; Ryan, K. M., *Nanotechnology* **2009**, *20*, 275605.
31. Bapat, A.; Anderson, C.; Perrey, C. R.; Carter, C. B.; Campbell, S. A.; Kortshagen, U., *Plasma Phys. Controlled Fusion* **2004**, *46*, B97.
32. Cullis, A. G.; Canham, L. T.; Calcott, P. D. J., *J. Appl. Phys.* **1997**, *82*, 909-965.
33. Hessel, C. M.; Henderson, E. J.; Veinot, J. G. C., *Chem. Mater.* **2006**, *18*, 6139.
34. Hessel, C. M.; Henderson, E. J.; Veinot, J. G. C., *J. Phys. Chem. C* **2007**, *111*, 6956.
35. Talapin, D. V.; Rogach, A. L.; Haase, M.; Weller, H., *J. Phys. Chem. B* **2001**, *105*, 12278.
36. Kelly, J. A.; Veinot, J. G. C., *ACS Nano* **2010**, *4*, 4645.
37. Hawa, T.; Zachariah, M. R., *J. Phys. Chem. C* **2008**, *112*, 14796.
38. Baldwin, R. K.; Pettigrew, K. A.; Garno, J. C.; Power, P. P.; Liu, G.-y.; Kauzlarich, S. M., *J. Am. Chem. Soc.* **2002**, *124*, 1150-1151.
39. Liu, S.; Kobayashi, M.; Sato, S.; Kimura, K., *Chem. Commun.* **2005**, 4690.
40. Yang, Y.; Wu, S.; Chiu, H.; Lin, P.; Chen, Y., *J. Phys. Chem. B* **2004**, *108*, 846.
41. Kang, Z.; Tsang, C. H. A.; Zhang, Z.; Zhang, M.; Wong, N.; Zapien, J. A.; Shan, Y.; Lee, S., *J. Am. Chem. Soc.* **2007**, *129*, 5326.
42. Williams, D. B.; Carter, C. B., *Transmission Electron Microscopy*. 2009.
43. Jaccodine, R. J., *J. Electrochem. Soc. C* **1963**, *110*, 524.
44. Tsoukalas, D.; Tsamis, C.; Normand, P., *J. Appl. Phys.* **2001**, *89*, 7809.

Chapter 3

Highly Luminescent Covalently Linked Silicon Nanocrystal/ Polystyrene Hybrid Functional Materials: Synthesis, Properties and Processability[2]

[2] A Portion of this chapter has been published:
Yang, Z.; Dasog, M.; Dobbie, A. R.; Lockwood, R.; Zhi, Y.; Meldrum, A.; Veinot, J. G. C., *Adv. Funct. Mater.* **2014**. *24*, 1345 – 1353.

3.1 Introduction

Semiconductor nanocrystals, or quantum dots (QDs), and functional polymers are among the many triumphs of modern materials chemistry.[1-4] QDs of a vast array of compound semiconductors (*e.g.*, CdSe, CdS, PbSe) are now routinely prepared and exploited for their size-dependent optical, electronic, and chemical properties.[5-8] Similarly, synthetic advances in polymer chemistry now allow rational design and tailoring of their material characteristics.[9-12] Marrying the exquisitely tunable properties of these two very different materials to produce hybrids offers yet another degree of freedom in the preparation of designer materials that find application in far reaching areas including optoelectronic structures,[4, 13] drug delivery systems,[14] sensors,[15] solar cells,[16] LEDs,[10] and data storage.[17]

Still, hurdles associated with the development of these hybrids remain that could slow and even preclude their practical implementation. Important among these are homogeneous distribution of QDs throughout the host polymer,[18-20] material stability,[21-22] and the established cytotoxicity of many prototypical QDs.[22-24] If QDs are not uniformly distributed, variable material properties will likely result. Unstable QD dispersions will certainly have variable properties and even degrade under some application conditions. It is reasonable issues

associated with uniformity and stability can be mitigated through direct bonding between the host polymer and the QD surface. Few examples of direct polymerization from the surface of archetypical CdSe QDs have appeared,[25] presumably because QDs and/or bonds tethering ligands to their surface are frequently not compatible with common polymerization conditions.[26] Fortunately, the ionic bonding of ligands with QD surfaces can undergo equilibrating exchange processes that allow introduction of various surface moieties, including polymers.[27-29] Another promising method for interfacing QDs with polymers relies upon exploiting the collective contributions of comparatively weak bonding interactions (*e.g.*, van der Waals interactions) between surface groups on QDs and polymers.[30-31] This approach has provided tailored QD solubility. Polymer coating can also slow, and even limit the release of cytotoxic ions, but this largely remains an outstanding challenge and clearly the most effective solution is to eliminate the use of cytotoxic elements.[24, 32]

Recent synthetic advances have resulted in well-defined silicon nanocrystals (SiNCs) that have bettered the community's understanding of their properties and reactivity.[33-36] Modern SiNCs exhibit many, if not all of the favorable properties of traditional QDs with the added benefit of being non-toxic.[37-42] Their surface chemistry differs substantially from that of other QDs and is routinely tailored *via* various hydrosilylation approaches that afford robust covalent Si–C bonds.[43-47]

These surface linkages preclude direct application of the surface exchange approach (*vide supra*). Approaches involving non-covalent surface-group/polymer interactions have been successfully applied to prepare SiNC/polymer hybrids typically with the intent of tailoring their solubility.[48-49] As with other QDs, this strategy requires multiple synthetic steps to prepare the NC/polymer hybrid structure and the comparatively weak interactions between the polymer and nanoparticles could limit material stability. Alternative methods for interfacing SiNCs with polymers must be explored if hybrid materials with targeted properties are to be realized.

Investigations describing bulk silicon surface chemistry are vast and examples exist that offer a variety of promising approaches for interfacing SiNCs with polymers. Generally, modification of bulk silicon begins with a reactive surface (*e.g.*, Si–H; Si–X where X = Cl, Br) that is subsequently modified by active functional groups on grafted molecules. For example: Tour and co-workers designed an efficient surface grafting approach on hydride-terminated silicon film surface using diazonium sources that leads to the formation of mono- and multilayers (*i.e.,* oligomers and polymers).[50-52] Xu *et al.* investigated surface initiated atom transfer radical polymerization (ARTP) on Si surfaces derived from monolayer modification of hydride and halogen terminated silicon and effectively induced the formation of polymer grafted surface.[53-54] Similarly, Zhang *et al.*

reported a rapid grafting method to grow thick and dense polymer brushes on silicon using a multiple-step functionalization including UV-induced hydrosilylation followed by rare metal catalyzed polymerization.[55] All of these reports provide a basis for the preparation of SiNC/polymer hybrids, but many employ metal catalysts or reaction conditions that could compromise favorable SiNC properties.

Most reports of photochemically and thermally induced hydrosilylation are aimed at monolayer formation, but they also provide important platforms for controlled surface polymerization. Such "one-pot" hydrosilylation/ polymerizations would dramatically simplify material preparation, minimize impurities, and assist in material processing. Our group, and others have reported polymerization of monomers (*e.g.*, propionic acid), indicating that catalyst free polymerization from SiNC surfaces is indeed possible.[56-58] Styrene has long been a preferred monolayer surface modification for SiNCs.[59] Polystyrene (PS) is a ubiquitous polymer with wide ranging applications. It has been introduced to bulk silicon surfaces *via* radical initiated polymerization,[60-61] and very recently thin films of PS composites containing ill-defined, blue-emitting Si nanoparticles were investigated as an active material in prototype thin film transistors.[61]

To date, the bulk synthesis and processing of well-defined SiNC/PS hybrid materials have not been reported. Furthermore, demonstrations of micro and

nanostructured SiNC/PS hybrid architectures exhibiting tunable photoluminescent properties have not appeared. Clearly, a comprehensive study on the physical and chemical properties as well as the solution processability of SiNC/PS hybrids would provide substantial benefit to the realization of functional materials and materials applications. To this end, this Chapter outlines a systematic investigation of the preparation of a series of covalently linked SiNC/PS hybrids with tunable luminescence arising from state-of-the-art SiNCs that exhibit SiNC-based photoluminescence arising from quantum confinement. We also demonstrate the solution processability of the present SiNC/PS hybrids and prepare a variety of chemically resistant, uniform nano- and microscale photoluminescent architectures.

3.2 Materials and Methods

3.2.1 Reagents and Materials

Hydrogen silsesquioxane (HSQ) was purchased from Dow Corning Corporation (Midland, MI) as FOx-17. Electronics grade hydrofluoric acid (HF, 49% aqueous solution) was purchased from J. T. Baker. Reagent grade methanol, toluene, ethanol, and 1-dodecene (97%) were purchased from Sigma

Aldrich and used as received. Styrene was purified by passing over neutral alumina immediately prior to use. Anodic aluminum oxide (AAO) membranes with 200 nm pores were obtained from Whatman.

3.2.2 Synthesis and Liberation of SiNCs

Preparation of oxide-embedded SiNCs (3 nm): Established literature procedures were used to prepare oxide-embedded silicon nanocrystals ($SiNC/SiO_2$).[62] Briefly, solvent was removed from the stock HSQ solution under vacuum to yield a white solid. The solid (*ca.* 4 g) was placed in a quartz reaction boat and transferred to a Lindberg Blue tube furnace and heated from ambient to a peak processing temperature of 1100 ℃ at 18 ℃ min^{-1} in a slightly reducing atmosphere (5% H_2/95% Ar). The sample was maintained at the peak processing temperature for 1 hour. Upon cooling to room temperature, the resulting amber solid was ground into a fine brown powder using a two-step process. The solid was crushed using an agate mortar and pestle to remove the large particles, and finally ground to a fine powder using a Burrell Wrist Action Shaker by shaking with high-purity silica beads for 5 hours. The resulting $SiNC/SiO_2$ powders were stable for extended periods and stored in standard glass vials.

Preparation of oxide-embedded SiNCs (d = 5 nm and 8 nm): After grinding with a mortar and pestle (*vide supra*), 0.5 g of the SiNC/SiO_2 composite containing 3 nm SiNCs were transferred to a high temperature furnace (Sentro Tech Corp.) for further thermal processing under an inert argon atmosphere. This procedure leads to particle growth while maintaining a relatively narrow particle size distribution. In the furnace, the SiNC/SiO_2 composite was heated to appropriate peak processing temperatures at 10 ℃/min to achieve the target particle size (*i.e.,* 1200 ℃ for 5 nm NCs and 1300 ℃ for 8 nm NCs). Samples were maintained at the peak processing temperature for 1 hour. After cooling to room temperature, the brown composites were ground using procedures identical to those noted above.

Liberation of SiNCs: Hydride-terminated SiNCs were liberated from the SiNC/SiO_2 composite by HF etching. Predefined quantities of SiNC/SiO_2 composite corresponding to the final hybrid SiNC loading (*i.e.,* 0.8, 1.6, and 2.4 wt% SiNC/polystyrene hybrids, 0.25 g, 0.50 g and 1.0 g of ground SiNC/SiO_2, respectively) were transferred to a polyethylene terephthalate beaker equipped with a Teflon coated stir bar. Ethanol (3 ml) and water (3 ml) were added under mechanical stirring to form a brown suspension followed by 3 ml of 49% HF aqueous solution (**Caution!** HF must be handled with extreme care). After 1 hour of etching in subdued light the suspension appeared orange/yellow.

Hydride-terminated SiNCs were subsequently extracted from the aqueous layer into *ca.* 30 ml of toluene by multiple (*i.e.*, 3 x 10 ml) extractions. The SiNC toluene suspension was transferred to test tubes and the SiNCs were isolated by centrifugation at 3000 rpm.

3.2.3 Formation and purification of SiNC/polystyrene hybrids

After decanting the clear toluene supernatant, hydride-terminated SiNCs were dispersed in 12 ml of a 1:1 styrene:toluene mixture to yield a cloudy suspension. This suspension was transferred to a dry 100 mL Schlenk flask equipped with magnetic stir bar and attached to an argon charged Schlenk line. The reaction mixture was subjected to three freeze–pump–thaw cycles and finally backfilled with argon. The temperature was increased to 110 ℃ in an oil bath under a static argon atmosphere. The reaction mixture was stirred for a minimum of 15 hours to yield a transparent orange solution.

Following cooling to room temperature, equal volumes of the orange solution were dispensed into 4 test tubes and 10 ml of ethanol was added to yield a cloudy light yellow dispersion. The precipitate was isolated by centrifugation at 3000 rpm for 10 minutes. The supernatant was decanted and the precipitate was redispersed in a minimum amount (*ca.* 5 ml) of toluene with ultrasonication for

0.5 hour and subsequently reprecipitated by addition of ethanol. This dissolution/precipitation/centrifugation procedure was repeated twice. Finally, the purified hybrid material were redispersed in toluene, filtered through a 0.45 μm PTFE syringe filter and dried under vacuum for 12 hours to yield an amber solid that was stored in a vial for further use until needed.

3.2.4 Fabrication of SiNC/Polystyrene Coated Fibers and Nanofabrics

Fabrication of polystyrene/SiNC coated fibers: Polyimide coated fused-silica capillary tubing was purchased from Polymicro Technologies with a 102 μm inner diameter (ID) and a 164 μm outer diameter (OD). Tubing was cleaved into *ca.* 5 cm long pieces, placed in a quartz boat and transferred into a tube furnace (Barnstead Thermolyne 21100). The tube was evacuated with a roughing pump and backfilled with oxygen, then heated at 650 ℃ for 45 minutes under a steady flow of oxygen to remove the polyimide cladding layer. After cooling to room temperature, the fibers were stored in air in a covered plastic petri dish for until needed.

Coating of the internal surface of the capillaries was achieved by dissolving 0.2 g of the 2.4 wt % SiNC (d = 3 nm)/polystyrene hybrid in *ca.* 3 ml of toluene. The end of the capillary was dipped into the toluene solution causing it to be

drawn into the tube by capillary action. The fibers were subsequently placed perpendicularly in a glass vial and dried in the air at room temperature for 24 hours.

Fabrication of SiNC/polystyrene nanofibres: Anodic aluminum oxide (AAO) membranes were placed on a standard glass microscope slide. 0.1 g of 0.8 wt % SiNC(d=3 nm)/polystyrene hybrid was dissolved in 3 ml of toluene and a predefined volume (*i.e.*, 60 μL) of the solution was drop-cast using a micropipette onto the top surface of the AAO. A second glass slide was placed on top of the liquid and gently pressed to form a "glass-liquid-AAO-glass" assembly. After drying in air, the glass slides were removed and the coated AAO was immersed in 10 M aqueous KOH for 24 hours to remove the AAO template. The resulting transparent film was washed with deionized water and ethanol and finally dried in air at room temperature for 24 hours.

3.2.5 Fabrication and Stability of Hybrid Thin Films

The toluene solution (700 μL) used for AAO templated nanofiber preparation (*vide supra*) was dropped into the wells of a glass spot plate. The solvent was evaporated after 15-hours in air at atmospheric pressure to yield a curved thin film that was readily released from the glass surface. The chemical resistance of the

thin films was assessed by immersing it in a saturated NaOH solution for a predefined time (*i.e.*, 15 days or 30 days) after which the photoluminescence (PL) was evaluated. Before the evaluation of the PL response, the samples were rinsed with deionized water and ethanol, and dried in vacuum for 24 hours. For the fabrication of a 500 nm-thick thin film, *ca.* 25 μL of the toluene solution used for AAO templated nanofiber preparation was transferred onto a clean silicon wafer (1.5 cm × 1.5 cm) and spin-coated three times with a speed of 3000 rpm for 30 seconds. Then the silicon wafer supported thin film was soaked in a saturated NaOH solution for 7 days. Finally, the supported thin film was removed from the solution and rinsed repeatedly with deionized water and ethanol, and dried under vacuum for 24 hours prior to evaluating the surface morpholoy using SEM.

3.2.6 Material Characterization and Instrumentation

PL spectra were obtained upon irradiating a quartz vial containing a toluene solution of the sample in question with the 441 nm line of a GaN laser (Wicked Laser Arctic Blue, ~600 mW). Emitted photons were collected with a fiber optic connected to an Ocean Optics USB2000 spectrometer. The spectrometer spectral response was normalized using a black body radiator.

^{1}H NMR spectra were recorded on an Agilent/Varian INova four-channel 500

MHz spectrometer and referenced externally to $SiMe_4$.

FT-IR spectroscopy was performed on uniform powder samples using a Nicolet Magna 750 IR spectrophotometer.

Raman spectroscopy was performed using a Renishaw inVia Raman microscope equipped with a 514 nm diode laser on the sample.

Gel-permeation chromatography (GPC) was performed at 35 ℃ using THF (stabilized with 250 ppm butylated hydroxytoluene) as the eluent at a flow rate of 1 mL min^{-1}. GPC measurements were made using a Varian GMBH GPC50 instrument and calibrated to polystyrene standards.

X-ray photoelectron spectroscopy (XPS) was acquired in the energy spectrum mode at 210 W, using a Kratos Axis Ultra X-ray photoelectron spectrometer. Samples were prepared as films drop-cast from solution onto a copper foil substrate. CasaXPS (VAMAS) software was used to process the high-resolution spectra. All spectra were calibrated to the C1s emission (284.8 eV) arising from adventitious carbon. After calibration, the extrinsic loss structure in the background from each spectrum was subtracted using a Shirley-type background. Sample compositions were determined from the emission intensities of the survey spectra using appropriate sensitivity factors. The high-resolution Si 2p region of spectra were fit to Si $2p_{1/2}$/Si $2p_{3/2}$ partner lines, with spin-orbit splitting fixed at 0.6 eV, and the Si $2p_{1/2}$/Si $2p_{3/2}$ intensity ratio was set to 1/2.

Thermal gravimetric analysis (TGA) was performed using a Perkin-Elmer Pyris 1 TGA. Samples were heated in a Pt pan under N_2 gas from 20 to 900 ℃ at a rate of 10 ℃/min.

Transmission electron microscopy (TEM) and energy dispersive X-ray (EDX) analyses were performed using a JEOL-2010 (LaB_6 filament) electron microscope with an accelerating voltage of 200 keV. TEM samples of SiNCs were drop-casted onto a holey carbon coated copper grid (SPI supplies) and the solvent was evaporated under vacuum. Secondary electron scanning electron microscopy (SEM) images of the nanofibres were obtained using field-emission SEM (JEOL JSM 7500F) with an accelerating voltage of 0.5 to 1.0 kV. Optical fibers and thin films were imaged using a JEOL 6301F field-emission SEM with an acceleration voltage of 5 kV. TEM and SEM images were processed using ImageJ software. Particle size distribution was processed by visual analysis of the images aided by the ImageJ software.

An Ar^+ laser with the wavelength of 488 nm was applied at a pumping power of 300 mW for the fluorescent imaging of the polymer-coated capillaries. The beam was incident in free space through the side of the optical fiber, which was placed on the stage of an epifluorescence microscope. The resulting fluorescence was collected through a 10× microscope objective (numerical aperture of 0.22) and imaged using a color CCD camera (Fast 1394 FireWire™, Retiga EX).

3.3 Results and Discussion

3.3.1 Functionalization of SiNCs with Polystyrene

The methodology used to prepare the present SiNC/PS hybrids is summarized in Scheme 3-1. Well-defined SiNCs (*i.e.,* d = 3, 5 and 8 nm) were prepared using a well-established procedure that exploits thermally induced disproportionation of commercially available hydrogen silsesquioxane (HSQ). Briefly, HSQ was heated in a slightly reducing atmosphere (*i.e.*, 5% H_2/95% Ar) at 1100 ℃ to induce formation of SiNCs inside an SiO_2-like matrix. Larger SiNCs were obtained following a second processing of the composite obtained from this procedure at higher temperatures (*i.e.*, 1200 ℃ d = 5 nm; 1300 ℃ d = 8 nm) in an Ar atmosphere.[63] The resulting brown solids were mechanically ground and etched using an ethanol/water HF solution to liberate hydride-terminated SiNCs.

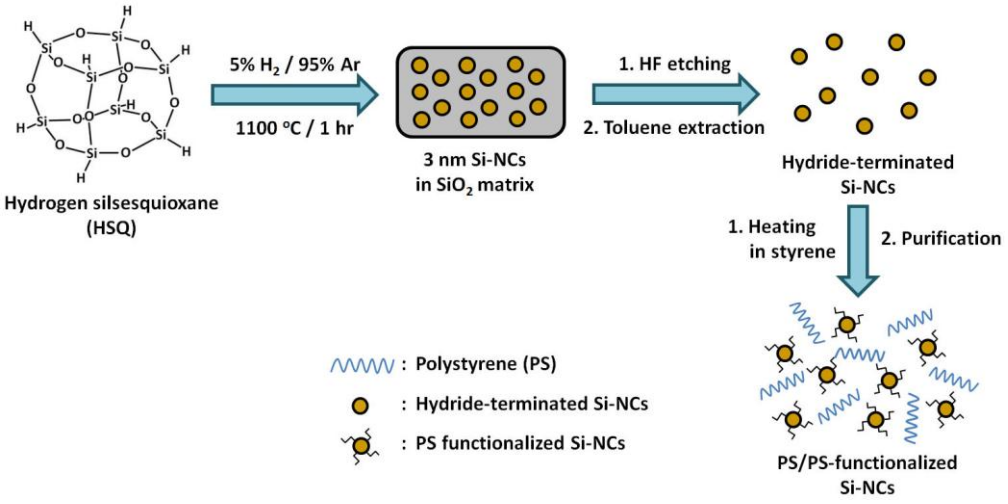

Scheme 3-1: Synthetic pathway from HSQ to polystyrene functionalized silicon nanocrystals/polystyrene hybrid material.

Subsequent functionalization/polymerization of styrene onto the SiNC surfaces was achieved using a convenient "one-pot" procedure followed by purification. SiNCs were combined with a toluene solution of styrene and heated to 110 ℃ in an Ar atmosphere. Prolonged heating (*i.e.*, at least 15 hours) yielded an orange solution from which an amber solid was precipitated upon addition of ethanol. FT-IR spectra of the products are consistent with SiNC surface functionalization and formation of polystyrene (Figure 3-1). Prior to reaction with styrene, the SiNC IR spectrum shows two distinctive signals at *ca.* 2100 cm^{-1} and *ca.* 850 cm^{-1} which are readily attributed to Si–H_x stretching and scissoring, respectively.[36] IR spectra of the SiNC/PS products are independent of the SiNC size and strongly resemble literature spectra of polystyrene.[64] The

stretching bands are attributable to the C–H_x of phenyl rings (3000–3200 cm^{-1}) and aliphatic polymer backbone (2650–2900 cm^{-1}). In addition, weak absorptions characteristic of overtone bands arising from mono-substituted aromatic rings are observed at 2000 cm^{-1} and 1650 cm^{-1}. Strong features at *ca.* 1600 cm^{-1} and *ca.* 1500 cm^{-1} are readily assigned to C=C stretching of the phenyl rings and a weak signal at *ca.* 1370 cm^{-1} is associated with C–H_x bending in aliphatic chain. The intense peak at *ca.* 1450 cm^{-1} has also been assigned to the combination of phenyl group the C=C stretching and aliphatic C–H_x bending.[64] Additional features, such as the weak features between 1250 cm^{-1} and 1000 cm^{-1}, and the strong peak at *ca.* 760 cm^{-1} arise from in-plane and out-of-plane the C–H_x bending. Of important note, there is no evidence of features arising from Si–H_x which supports the conclusion that SiNCs are covalently attached to the polystyrene. NMR analysis confirms no free styrene is present in the purified samples (Figure 3-2). Raman spectroscopy shows a clear absorption at 624 cm^{-1}, confirming the Si-C covalent linkages between the polystyrene and SiNC surface (Figure 3-3).[65]

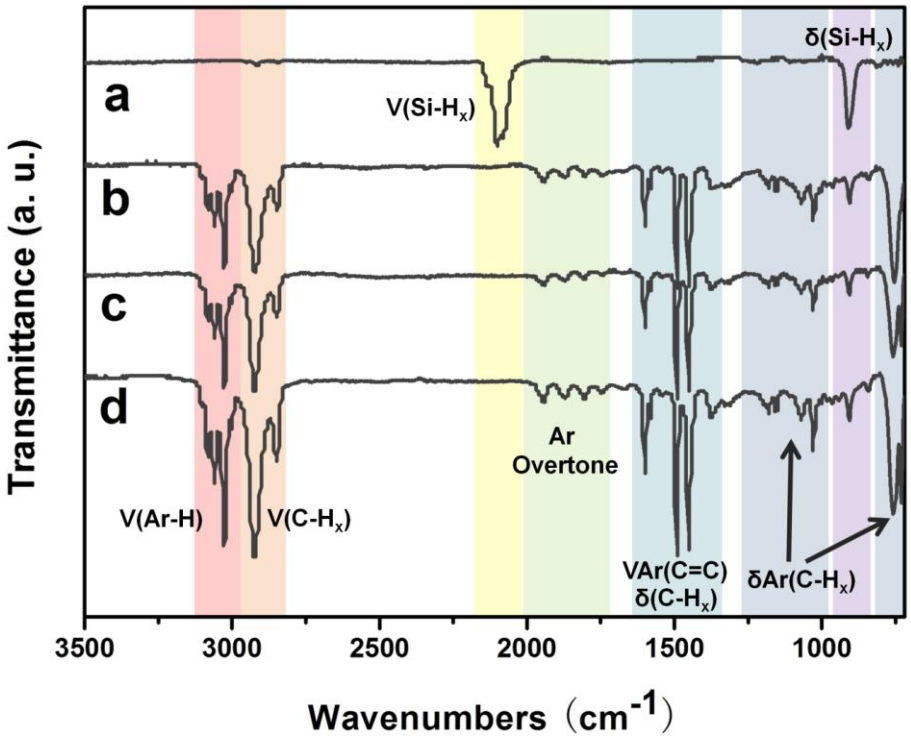

Figure 3-1: FT-IR spectra of (a) 3 nm hydride-terminated and (b-d) Si nanocrystals with different sizes (b: 3 nm, c: 5 nm and d: 8 nm).

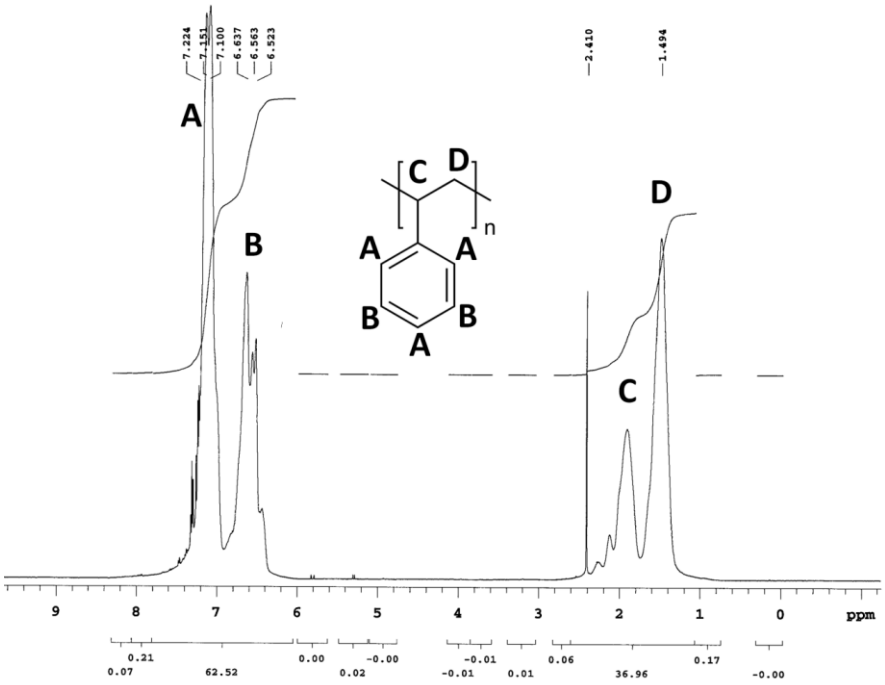

Figure 3-2: ^{1}H NMR spectrum ($CDCl_3$, 500 MHz) of SiNC/polystyrene hybrid material. Peak at 2.41 rpm is correspondent to a trace amount of toluene.

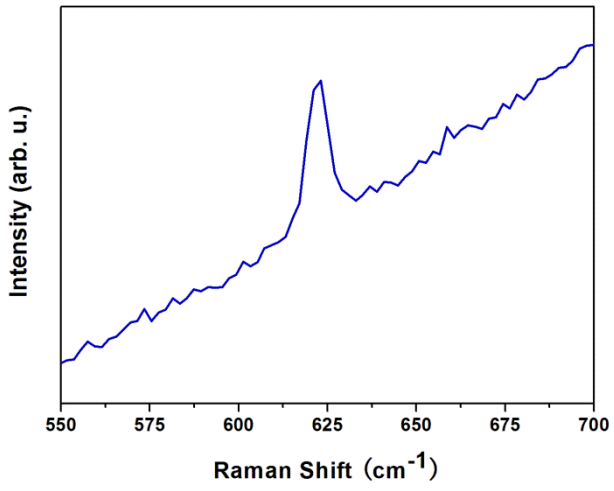

Figure 3-3: The Si-C stretching region of the Raman spectrum of the hybrid material. The huge background results from the photoluminescence of the material.

The uniformity of the SiNC/PS hybrids was evaluated using bright field transmission electron microscopy (TEM). Figure 3-4 shows minimal clustering of the SiNCs regardless of size, indicating the NCs are uniformly dispersed throughout the polymer. Photoluminescence spectroscopy clearly shows the size-dependent emission of the SiNCs (*i.e.*, d = 3 nm, λ_{em}= 700 nm; d = 5 nm, λ_{em}= 786 nm; d = 8 nm, λ_{em}= 888 nm) is preserved with functionalization (Figure 3-5). Consistent with this emission arising from a band gap transition, we note a radiative lifetime decay of 164.5 μs (Figure 3-6) indicative of a SiNC-based band gap emission and no evidence of excitation wavelength dependence.

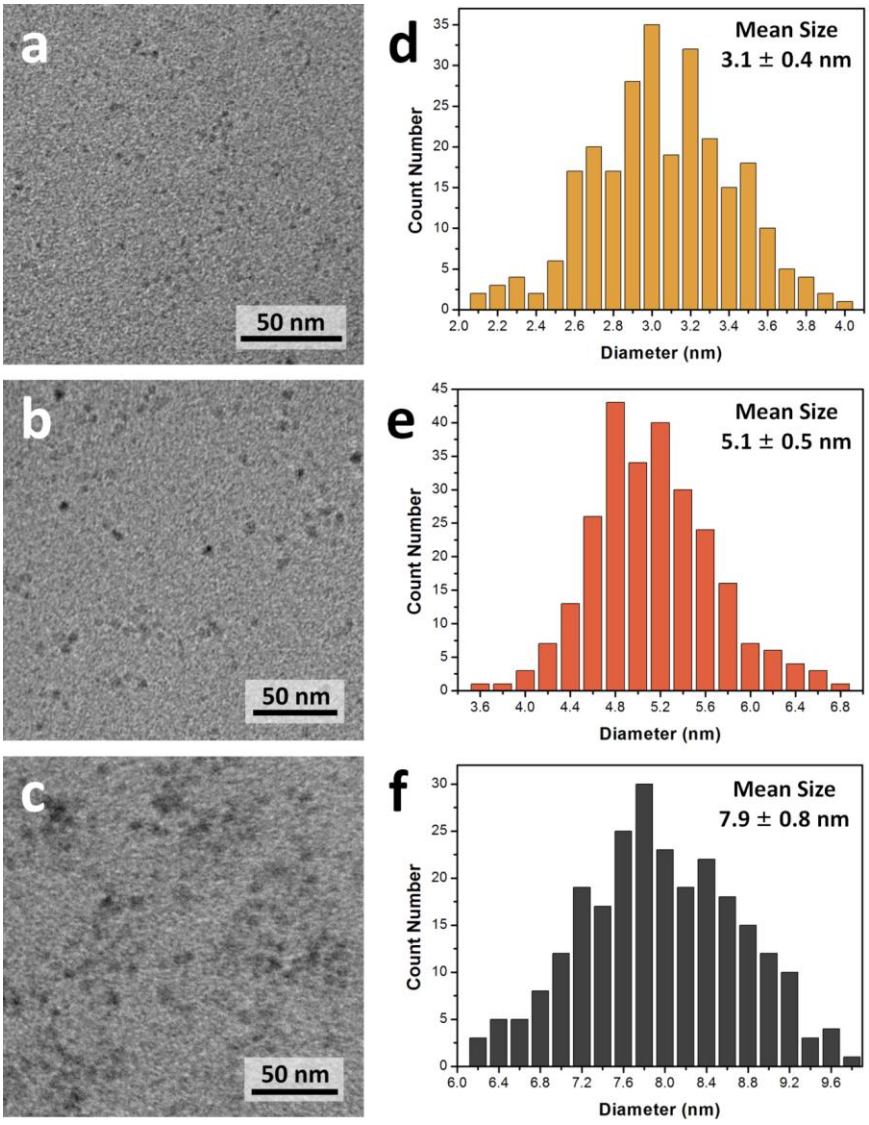

Figure 3-4: Bright field TEM images (a-c) and size distribution (d-f) of ensembles of the polystyrene-functionalized silicon nanocrystals with several average diameters: (a, d) 3.1 nm, (b, e) 5.1 nm, and (c, f) 7.9 nm.

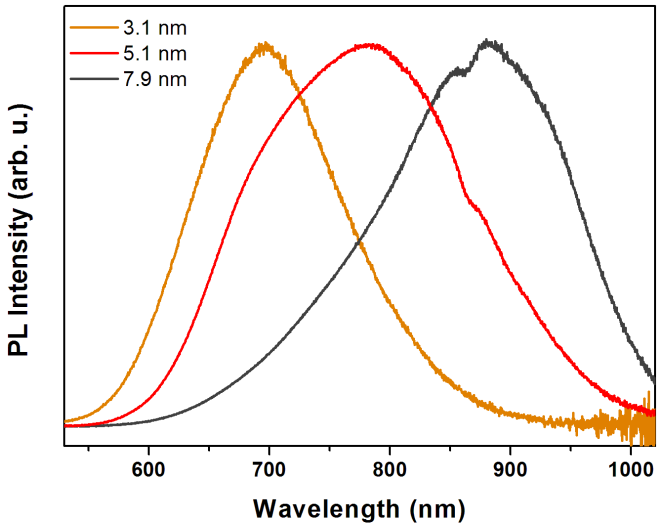

Figure 3-5: PL spectra of toluene solutions containing SiNC/PS hybrid materials with indicated mean particle sizes determined using TEM.

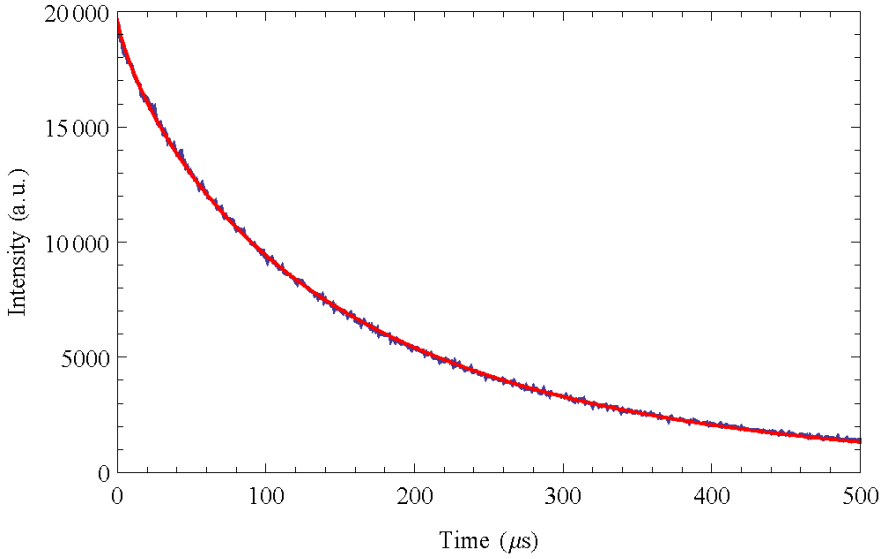

Figure 3-6: Representative data of lifetime decay with fitting curve (using 3 nm SiNC/PS hybrids in toluene solution under 476 nm (10 mW) irradiation). The decay was fit with a stretched exponential function: $F(t) = A*\exp(-(t / \tau)^{\gamma})$, where $A = 19623.4$, $\gamma = 0.809206$, lifetime decay $\tau = 146.5$ μs.

Survey X-ray photoelectron (XPS, not shown) and Energy Dispersive X-ray spectra (EDX) indicate the present SiNC/PS hybrids contain only silicon, oxygen and carbon. High-resolution XPS analyses further supports the formation of PS functionalized SiNCs (Figure 3-7). The C 1s emission located at 284.8 eV and a second emission at 291.6 eV (Figure 3-7a) substantiate the presence of aromatic groups (*i.e.*, phenyl rings).[60] Multi-component features appear in the Si 2p spectral region (Figure 3-7b). For clarity only the Si $2p_{3/2}$ components of the spin-orbit coupling pairs are displayed. Consistent with previous reports of functionalized SiNCs,[66] an emission attributable to elemental Si is noted at 99.3 eV. Other fitted features (*i.e.*, 100.4, 101.6, 102.4 and 103.4 eV) are readily assigned to Si–C and silicon oxides.[57]

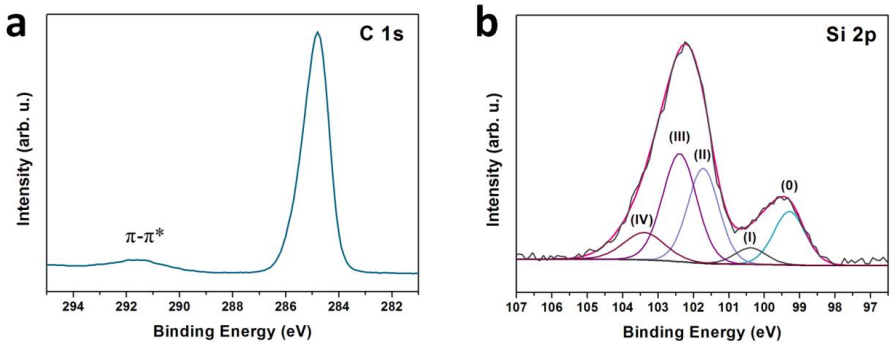

Figure 3-7: High-resolution XPS spectra of carbon (1s) and silicon (2p) for the SiNCs/PS hybrid material. Fitting results are shown for the silicon spectrum with only the Si $2p_{3/2}$ signal shown. The Si $2p_{1/2}$ signals have been omitted for clarity.

3.3.2 Polymer Behavior and Functionalization Mechanism

To investigate the impact of the SiNC concentration on hybrid material properties, a series of materials were prepared using varied concentrations of 3 nm diameter SiNCs. The SiNC content was determined using thermal gravimetric analysis (TGA, Figure 3-8). We note that in order to achieve complete SiNC functionalization, qualitatively determined by the formation of a non-opalescent solution, longer processing times are required when more NCs are present (15 hours for 0.8 wt% SiNCs, 59 hours for 2.4 wt% SiNCs). GPC provides molecular weight information for the SiNC/PS hybrids (Figure 3-9). Two major components are observed: a weak signal indicating a component with a M_w of several million g/mol and a second more intense peak is found at a longer retention time corresponding to M_w = 200000 – 330000 g/mol. We attribute the larger molecular weight component to the PS functionalized silicon particles, while those molecules with smaller M_w values are free PS formed during hydrosilylation. Based on the GPC results, the thickness of the polymer brush on SiNC surface is about 30 to 90 nm depending on the particle sizes.

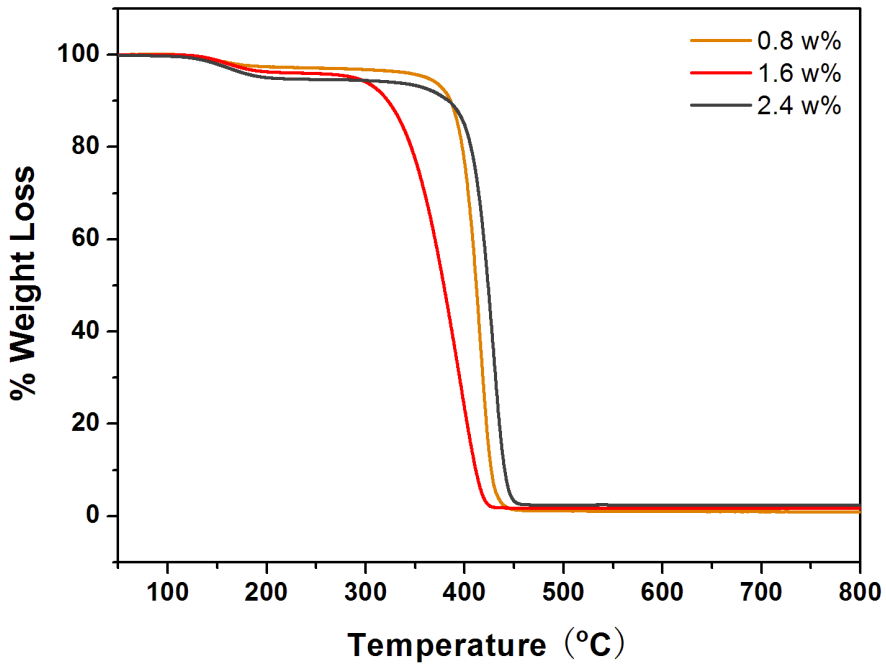

Figure 3-8: Thermogravimetric analysis (TGA) of hybrid materials with indicated 3 nm SiNC concentration.

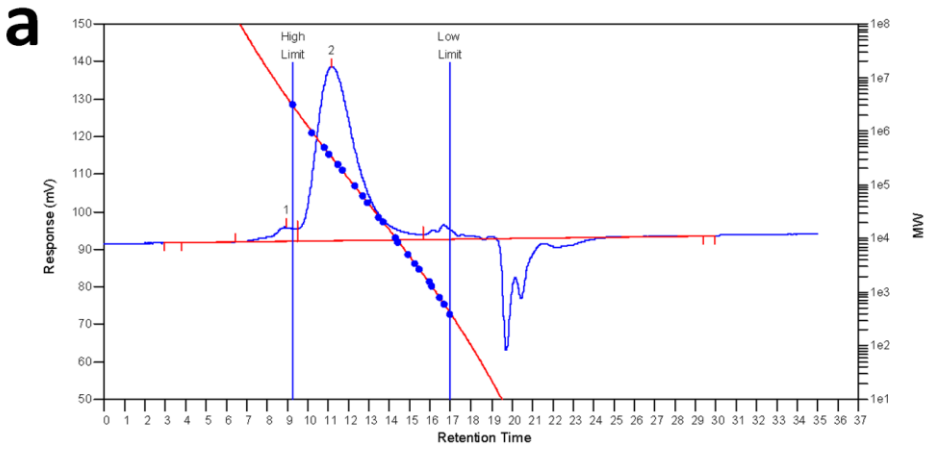

MW Averages

Peak No	Mp	Mn	Mw	Mz	Mz+1	Mv	PD
1	4511991	5281947	9430222	24555816	51086087	8216875	1.78537
2	321997	77029	334048	653083	987013	294143	4.33665

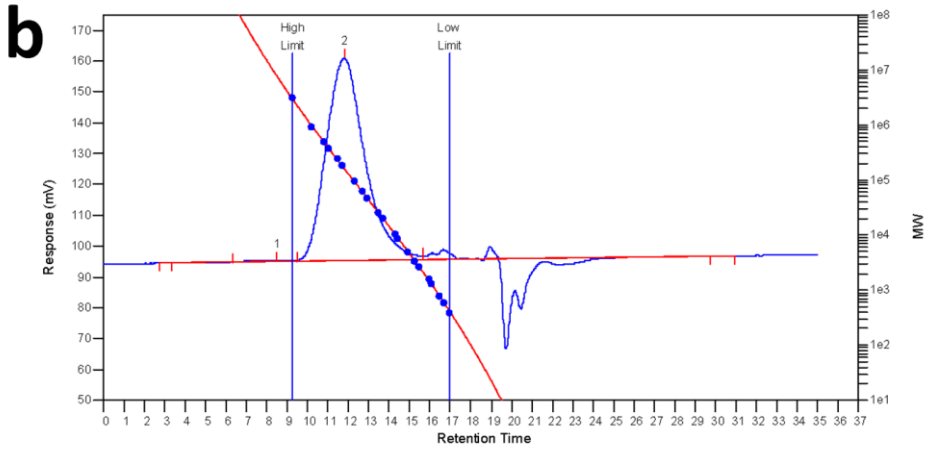

MW Averages

Peak No	Mp	Mn	Mw	Mz	Mz+1	Mv	PD
1	21114037	9681106	26623846	58980376	87322387	22861798	2.75008
2	159629	63098	207870	419952	680297	183392	3.2944

Figure 3-9: GPC results of SiNC/PS hybrid material with various particle sizes: (a) 3 nm, (b) 5 nm, and (c) 8 nm.

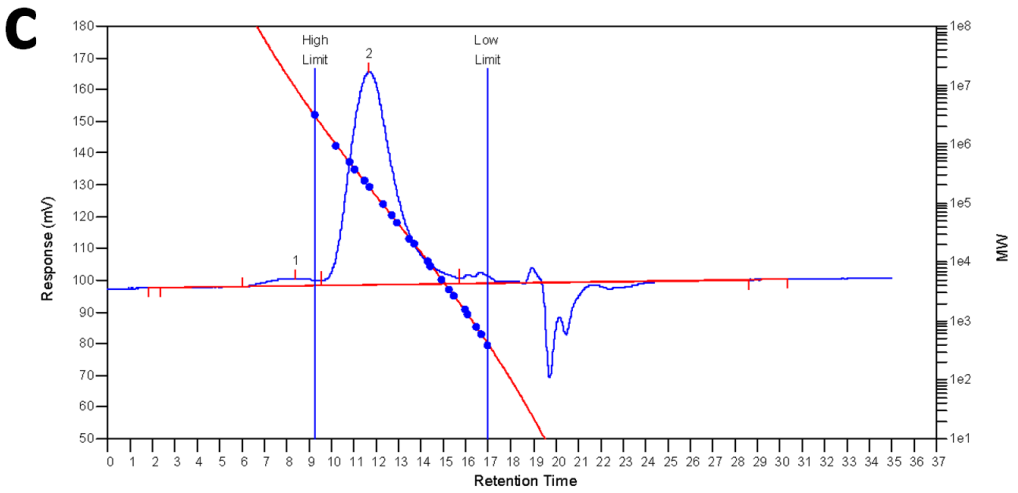

MW Averages

Peak No	Mp	Mn	Mw	Mz	Mz+1	Mv	PD
1	8704096	7947921	22878091	61394234	106174141	19157735	2.8785
2	184890	55710	220456	455135	739541	193027	3.95721

Figure 3-9 (Continued): GPC results of SiNC/PS hybrid material with various particle sizes: (a) 3 nm, (b) 5 nm, and (c) 8 nm.

As noted above, styrene has been a SiNC surface functionalization of choice because of the favorable solution properties and stability this surface modification endows. Surprisingly, reports of polymerization/oligomerization of styrene on/from the surface of SiNCs are rare.[61] Previously, styrene polymerization on the presence of Si nanoparticles has been attributed to the homolytic cleavage of the Si-H bond.[61] While this reaction mechanism is likely active at high reaction temperatures (*i.e.*, ≥150 ℃), there is little question it is not the dominant reaction pathway for the comparatively low temperatures used here. Scheme 3-2 illustrates how polymerization is expected to proceed. Rather than relying upon thermally induced homolytic cleavage of the Si–H bond,[44] or the presence of an external radical initiator,[60] styrene can thermally self-initiate producing radicals *via* a Diels-Alder cycloaddition.[67] Besides the initiation of styrene polymerization in solution, these radicals can abstract hydrogen atoms from the Si–H terminated SiNC surface and the resulting silyl radicals are free to react with solution-phase styrene. This would form Si–C bonds and new radicals localized on the beta-carbon of the surface bonded moiety, which can subsequently react with more styrene to produce surface bonded oligomers/polymers or react in a surface chain-hydrosilylation reaction.[68] Finally reactions end with radical–radical termination events. A more detailed study of the polymerization mechanism and the roles of various additives are necessary to extend to the synthesis and

applications of other types of polymer/SiNCs hybrids.

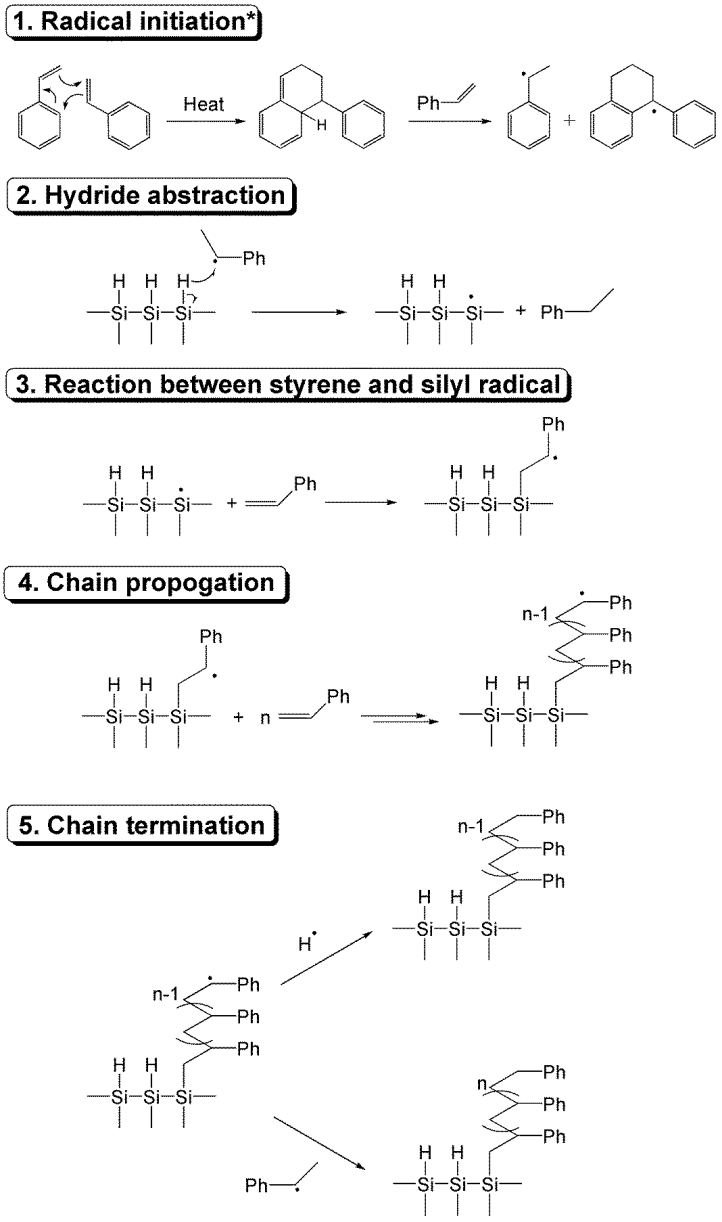

Scheme 3-2: Possible routes for the PS functionalization of the hydride terminated SiNCs. Note (*) indicates multiple products co-exist during the initiation step.[67] Si surface radicals might also be created by the hydrogen transfer from the surface to the ligand radical,[44] which is not shown here for clarity.

3.3.3 Processability and Stability of Hybrid Material

One of the primary goals of developing functional hybrid materials like the SiNC/PS hybrids presented here is to effectively combine the characteristics of the constituent components. Photoluminescent response, solution processability, and chemical stability are key properties of the present systems. To demonstrate the unification and utility of these hybrid characteristics the fabrication and properties of three photoluminescent prototype PS/SiNCs micro/nanostructures is described.

Photoluminescent optical fibres were fabricated by solution-coating of the interior surfaces of commercially available quartz capillaries. A toluene solution of the SiNC/PS (d = 3 nm) was drawn into a fiber that had been freed from its protective polyimide coating. Following evaporation of the solvent, a smooth thin film of the hybrid is formed on the inner capillary wall (see Figure 3-10). To approximate the residual solvent content, TGA analysis of a thin film sample was performed which indicated *ca.* 8 mass % toluene remained (See Figure 3-11). This solvent content exhibits no obvious influence on the material properties. While the coating layer cannot be imaged directly with an optical microscope, intense and uniform red PL couples the whole fiber under 488 argon laser irradiation (Figure 3-10f and g). Scanning electron microscopy (SEM) shows a

smooth *ca.* 1.5 μm thick polymer layer (Figure 3-10a–d).

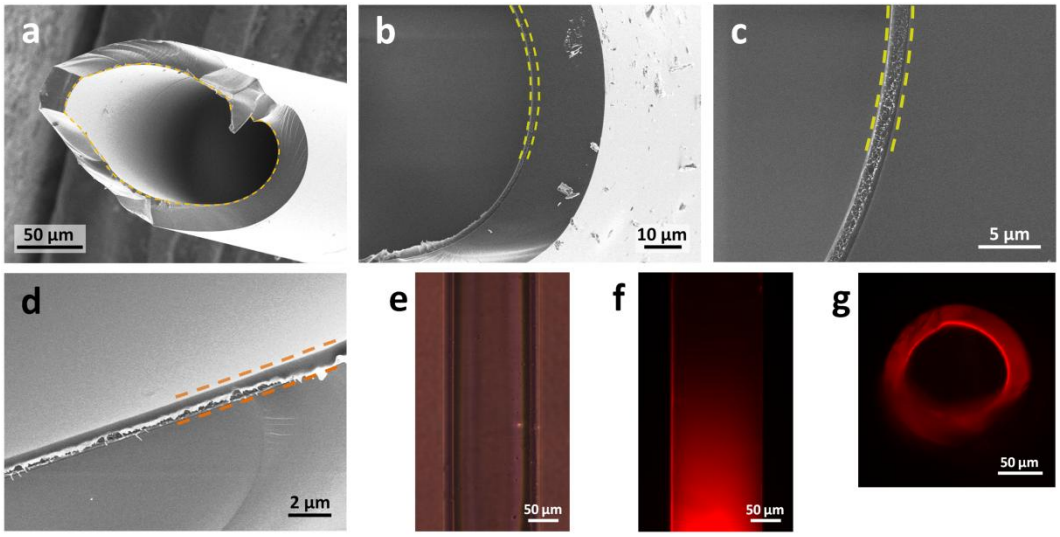

Figure 3-10: SEM images (a-d) of optical fibers with 3 nm SiNC/PS coating on the inner wall. Dotted lines indicate the coating layer. (e) optical microscope and (f, g) fluorescence microscope images of the fibers with red emission from (f) the top and (g) cleaved end shown upon 488 nm excitation.

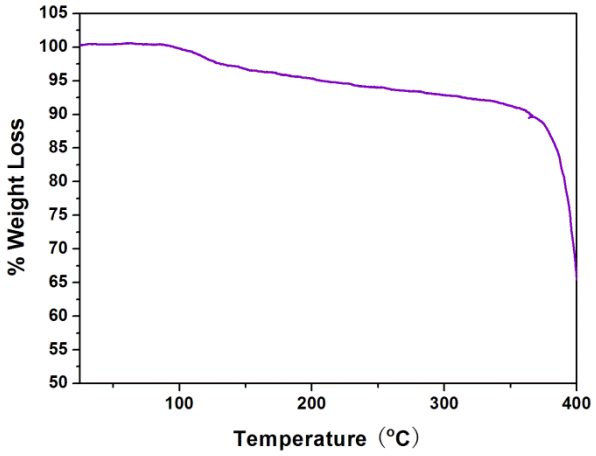

Figure 3-11: Thermogravimetric analysis of a thin film sample. The weight loss below 360 ^{o}C is reasonably attributed to the evaporation of residual toluene.

To extend our solution coating procedure and fabricate nanoscaled structures it was necessary to determine if the present hybrids were resistant to the basic etching environment used to remove our nano-templates of choice (*i.e.,* anodic aluminum oxide, AAO). This is particularly true considering that hydride-terminated SiNCs are readily oxidized and their luminescence compromised upon exposure to basic solutions.[69] Reports also indicate that the SiNC-based luminescence of hybrid materials is compromised or blue-shifted upon treatment with NH_4OH or NaOH solutions despite encapsulation.[70] To investigate the resistance of our hybrids in strongly basic conditions, samples were cast as transparent SiNC/PS luminescent thin films with thicknesses in the range of 45–60 μm (See Figure 3-12). These films were immersed for 15- and 30-day intervals in NaOH aqueous solutions (19.4 M) followed by evaluation of their morphology, texture, as well as the intense PL. Negligible changes were detected (Figure 3-12a) in the optical response, however some minor damage to the outer polymer surface was noted (Figure 3-12d). Freestanding thin films (*i.e.*, thickness *ca.* 500 nm) were also prepared *via* spincoating (See Figure 3-13) and were exposed to saturated aqueous NaOH solutions for 7 days. No material degradation was detected at the sensitivity of SEM.

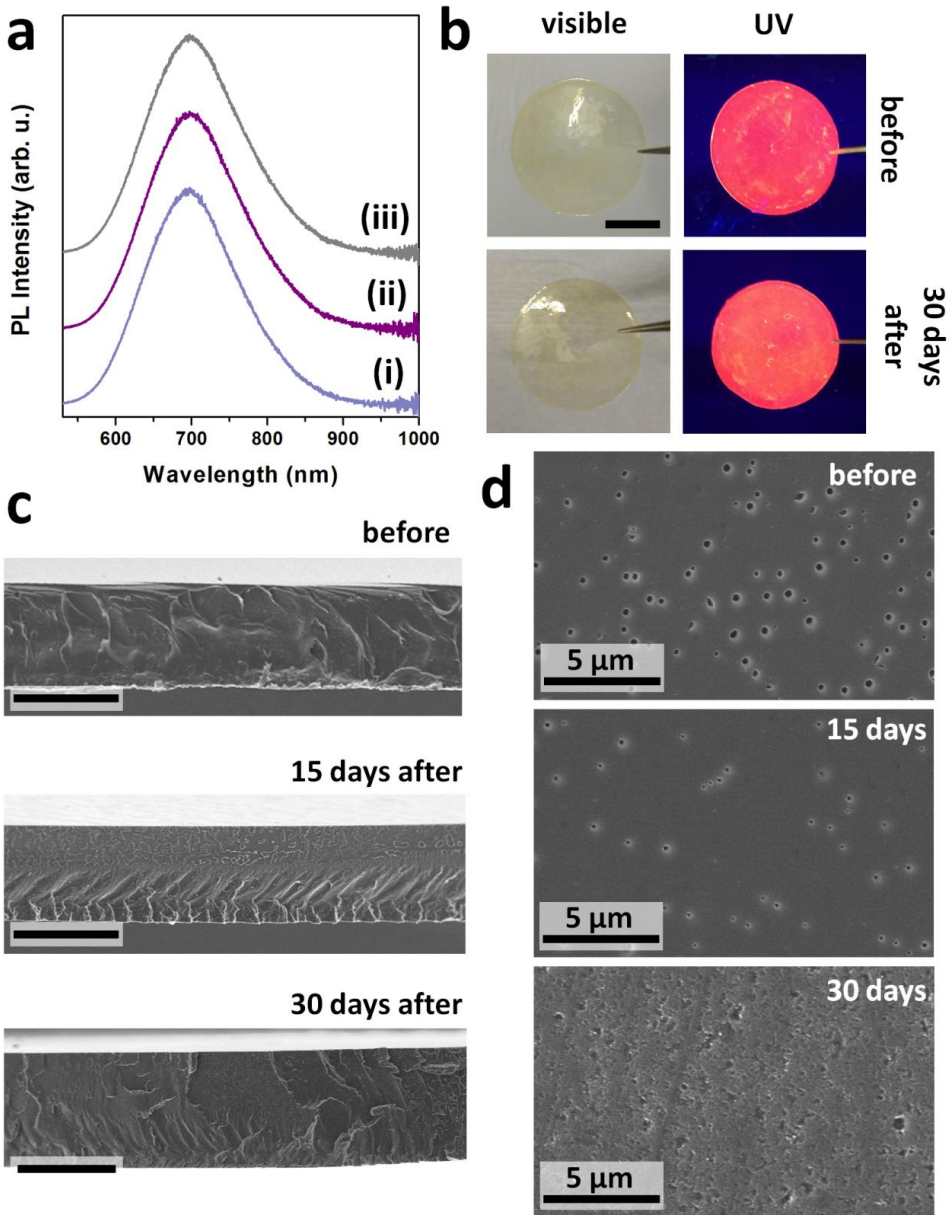

Figure 3-12: Characterization of PS functionalized 3 nm SiNC/PS thin film before and after the base solution resistance test. (a) PL spectra and (b) images showing their luminescent property before and after the test: (i) before the test; (ii) 15 days after, and (iii) 30 days after (scale bar: 1 cm). (c, d) SEM images of a thin film before and after the immersion test ((c) side view, (d) top view, scale bar: 50 µm).

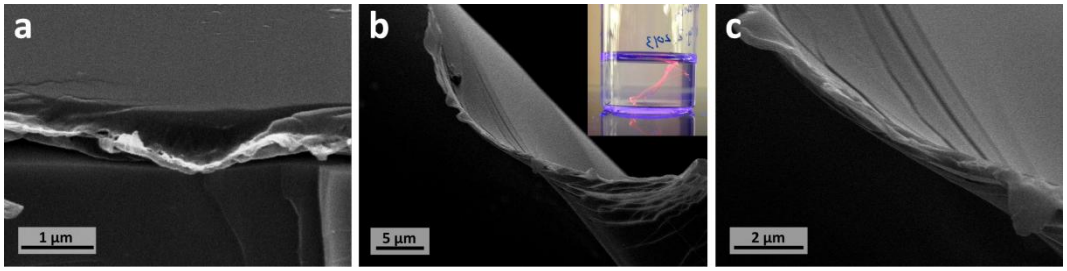

Figure 3-13: SEM images of thin film spin-coated onto a silicon substrate before (a) and after (b, c) the 7-day immersion test. The thickness was *ca.* 500 nm. No significant change was observed. Inset: image of a freestanding thin film during immersion test under 365 nm UV light irradiation.

Having established our hybrids are chemically resistant, we endeavored to exploit their properties and fabricate hybrid nanostructures using a sacrificial template, as summarized in Scheme 3-3. Briefly, a piece of commercial by available AAO bearing pore sizes of d = 250 – 300 nm (Figure 3-14) was dropcoated with a toluene solution of SiNC/PS (d = 3 nm). A glass slide was placed on top of the template and gently pressed, resulting in a uniform thin film on top of the AAO. The hybrid solution was draw into the nanopores by capillary action. The solvent was evaporated upon standing under ambient conditions to yield a highly luminescent solid film with hybrid nanofibers within the pores (See Figure 3-15). The chemical resistance of the polystyrene component of the hybrid enabled basic etching of the AAO template without any

detectable deterioration of the SiNC optical response. Following template removal, no trace aluminum was detected by EDX, consistent with complete template removal. SEM images of the liberated thin films clearly show bundles of flexible nanofibres with a diameter of *ca.* 250 nm and lengths exceeding 30 μm (Figure 3-15c–f). The interface between the surface film layer and nanofibres is shown in Figure 3-15f. The thin film is *ca.* 3 μm thick with a smooth surface. On the interface we also notice branch-like ends of the nanofibres that can be reasonably attributed to pore branching within the AAO template.

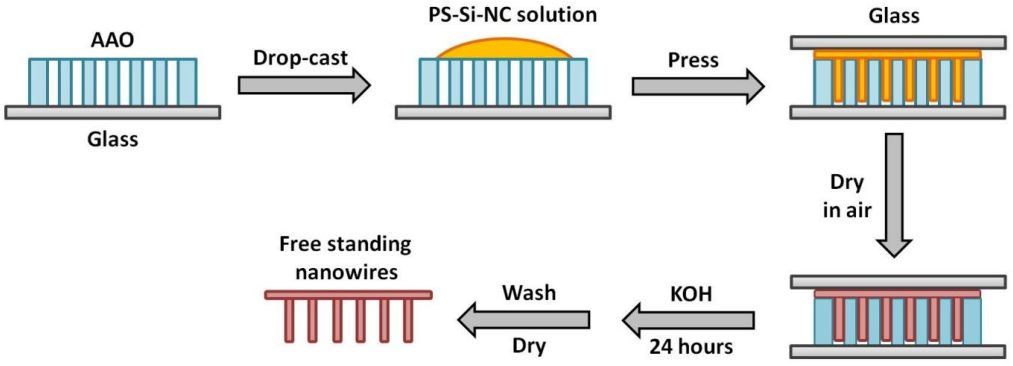

Scheme 3-3: A schematic of the fabrication of SiNC/PS hybrid nanofibres.

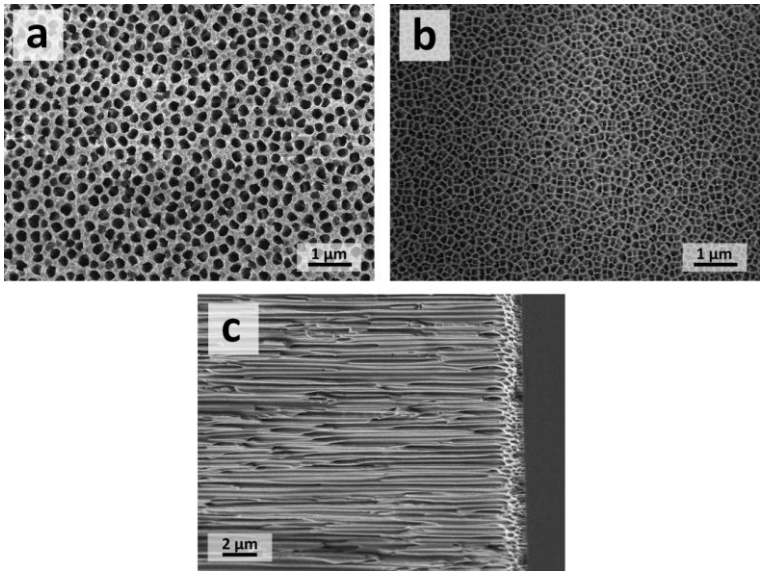

Figure 3-14: SEM images of the anodic aluminum oxide template with 200-300 nm pore size: (a) top view, (b) bottom view, and (c) side view.

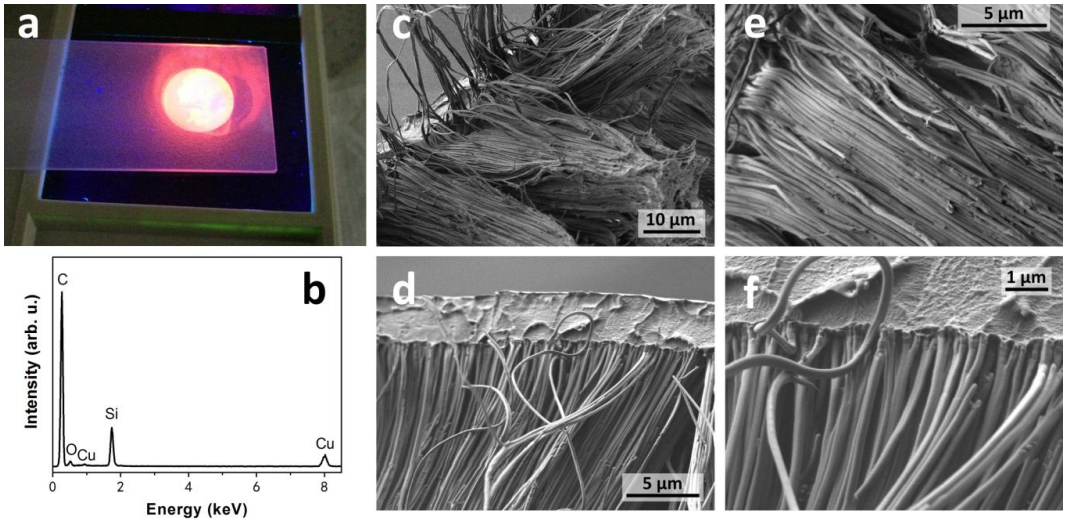

Figure 3-15: (a) Luminescent nanofibres fabricated using the 3 nm SiNC/PS hybrid material by drop-casting. (b) EDX showing the presence of silicon, carbon and oxygen. Cu signals arise from the sample grid. (c-f) SEM images of nanofibres liberated from the template.

3.4 Conclusions

In summary, a straightforward synthetic route for preparing highly luminescent, solution processable, SiNC/PS hybrid materials was reported. Hydride-terminated SiNC surface have been surface modified with polystyrene using a size-independent radical-initiated hydrosilylation. Detailed material information including, composition, optical properties and particle distribution, has been obtained. Combining the properties of SiNCs with PS significantly increases solubility, rendering the particles solution processable and provides the opportunity to fabricate uniform nano- and microscale architectures. Furthermore, the polystyrene matrix renders the SiNC chemically resistant to prolonged exposure to strongly basic conditions.

3.5 References

1. Burda, C.; Chen, X.; Narayanan, R.; El-Sayed, M. A., *Chem. Rev.* **2005**, *105*, 1025-1102.
2. Michalet, X.; Pinaud, F. F.; Bentolila, L. A.; Tsay, J. M.; Doose, S.; Li, J. J.; Sundaresan, G.; Wu, A. M.; Gambhir, S. S.; Weiss, S., *Science* **2005**, *307*, 538-544.
3. Kamat, P. V., *J. Phys. Chem. C* **2007**, *111*, 2834-2860.
4. Gao, X.; Cui, Y.; Levenson, R. M.; Chung, L. W. K.; Nie, S., *Nat. Biotech.* **2004**, *22*, 969-976.
5. Murray, C. B.; Norris, D. J.; Bawendi, M. G., *J. Am. Chem. Soc.* **1993**, *115*, 8706-8715.
6. Schaller, R. D.; Klimov, V. I., *Phys. Rev. Lett.* **2004**, *92*, 186601.
7. Peng, Z. A.; Peng, X., *J. Am. Chem. Soc.* **2000**, *123*, 183-184.
8. Peng, X.; Schlamp, M. C.; Kadavanich, A. V.; Alivisatos, A. P., *J. Am. Chem. Soc.* **1997**, *119*, 7019-7029.
9. Dabbousi, B. O.; Bawendi, M. G.; Onitsuka, O.; Rubner, M. F., *Appl. Phys. Lett.* **1995**, *66*, 1316-1318.
10. Lee, J.; Sundar, V. C.; Heine, J. R.; Bawendi, M. G.; Jensen, K. F., *Adv. Mater.* **2000**, *12*, 1102-1105.
11. Bakueva, L.; Musikhin, S.; Hines, M. A.; Chang, T. W. F.; Tzolov, M.; Scholes, G. D.; Sargent, E. H., *Appl. Phys. Lett.* **2003**, *82*, 2895-2897.
12. Lee, D. Y.; Pham, J. T.; Lawrence, J.; Lee, C. H.; Parkos, C.; Emrick, T.; Crosby, A. J., *Adv. Mater.* **2013**, *25*, 1248-1253.
13. Chan, Y.-H.; Ye, F.; Gallina, M. E.; Zhang, X.; Jin, Y.; Wu, I. C.; Chiu, D. T., *J. Am. Chem. Soc.* **2012**, *134*, 7309-7312.
14. Sukhorukov, G. B.; Rogach, A. L.; Garstka, M.; Springer, S.; Parak, W. J.; Muñoz-Javier, A.; Kreft, O.; Skirtach, A. G.; Susha, A. S.; Ramaye, Y.; Palankar, R.; Winterhalter, M., *Small* **2007**, *3*, 944-955.
15. Freeman, R.; Finder, T.; Bahshi, L.; Gill, R.; Willner, I., *Adv. Mater.* **2012**, *24*, 6416-6421.
16. Ren, S.; Chang, L.-Y.; Lim, S.-K.; Zhao, J.; Smith, M.; Zhao, N.; Bulović, V.; Bawendi, M.; Gradečak, S., *Nano Lett.* **2011**, *11*, 3998-4002.
17. Li, X.; Bullen, C.; Chon, J. W. M.; Evans, R. A.; Gu, M., *Appl. Phys. Lett.* **2007**, *90*, 161116-3.
18. Vaia, R. A.; Wagner, H. D., *Mater. Today* **2004**, *7*, 32-37.
19. Bradley, M.; Bruno, N.; Vincent, B., *Langmuir* **2005**, *21*, 2750-2753.
20. Joumaa, N.; Lansalot, M.; Théretz, A.; Elaissari, A.; Sukhanova, A.; Artemyev, M.; Nabiev, I.; Cohen, J. H. M., *Langmuir* **2006**, *22*, 1810-1816.

21. Tang, J.; Brzozowski, L.; Barkhouse, D. A. R.; Wang, X.; Debnath, R.; Wolowiec, R.; Palmiano, E.; Levina, L.; Pattantyus-Abraham, A. G.; Jamakosmanovic, D.; Sargent, E. H., *ACS Nano* **2010**, *4*, 869-878.
22. Derfus, A. M.; Chan, W. C. W.; Bhatia, S. N., *Nano Lett.* **2003**, *4*, 11-18.
23. Oberdorster, G.; Oberdorster, E.; Oberdorster, J., *Environ. Heatlth Perspect.* **2005**, *113*, 823-39.
24. Resch-Genger, U.; Grabolle, M.; Cavaliere-Jaricot, S.; Nitschke, R.; Nann, T., *Nat. Methods* **2008**, *5*, 763-775.
25. Nakashima, T.; Sakakibara, T.; Kawai, T., *Chem. Lett.* **2005**, *34*, 1410-1411.
26. Tomczak, N.; Jańczewski, D.; Han, M.; Vancso, G. J., *Prog. Polym. Sci.* **2009**, *34*, 393-430.
27. Wang, Y. A.; Li, J. J.; Chen, H.; Peng, X., *J. Am. Chem. Soc.* **2002**, *124*, 2293-2298.
28. Wang, M.; Dykstra, T. E.; Lou, X.; Salvador, M. R.; Scholes, G. D.; Winnik, M. A., *Angew. Chem. Int. Ed.* **2006**, *45*, 2221-2224.
29. Sill, K.; Emrick, T., *Chem. Mater.* **2004**, *16*, 1240-1243.
30. Pellegrino, T.; Manna, L.; Kudera, S.; Liedl, T.; Koktysh, D.; Rogach, A. L.; Keller, S.; Rädler, J.; Natile, G.; Parak, W. J., *Nano Lett.* **2004**, *4*, 703-707.
31. Yu, W. W.; Chang, E.; Falkner, J. C.; Zhang, J.; Al-Somali, A. M.; Sayes, C. M.; Johns, J.; Drezek, R.; Colvin, V. L., *J. Am. Chem. Soc.* **2007**, *129*, 2871-2879.
32. King-Heiden, T. C.; Wiecinski, P. N.; Mangham, A. N.; Metz, K. M.; Nesbit, D.; Pedersen, J. A.; Hamers, R. J.; Heideman, W.; Peterson, R. E., *Environ. Sci. Technol.* **2009**, *43*, 1605-1611.
33. Kelly, J. A.; Shukaliak, A. M.; Fleischauer, M. D.; Veinot, J. G. C., *J. Am. Chem. Soc.* **2011**, *133*, 9564-9571.
34. Hannah, D. C.; Yang, J.; Podsiadlo, P.; Chan, M. K. Y.; Demortière, A.; Gosztola, D. J.; Prakapenka, V. B.; Schatz, G. C.; Kortshagen, U.; Schaller, R. D., *Nano Lett.* **2012**, *12*, 4200-4205.
35. Miller, J. B.; Van Sickle, A. R.; Anthony, R. J.; Kroll, D. M.; Kortshagen, U. R.; Hobbie, E. K., *ACS Nano* **2012**, *6*, 7389-7396.
36. Dasog, M.; Yang, Z.; Regli, S.; Atkins, T. M.; Faramus, A.; Singh, M. P.; Muthuswamy, E.; Kauzlarich, S. M.; Tilley, R. D.; Veinot, J. G. C., *ACS Nano* **2013**, *7*, 2676-2685.
37. Alsharif, N. H.; Berger, C. E. M.; Varanasi, S. S.; Chao, Y.; Horrocks, B. R.; Datta, H. K., *Small* **2009**, *5*, 221-228.
38. Erogbogbo, F.; Yong, K.-T.; Roy, I.; Xu, G.; Prasad, P. N.; Swihart, M. T., *ACS Nano* **2008**, *2*, 873-878.
39. Park, J.-H.; Gu, L.; von Maltzahn, G.; Ruoslahti, E.; Bhatia, S. N.; Sailor, M. J., *Nat. Mater.* **2009**, *8*, 331-336.

40. Pavesi, L.; Dal Negro, L.; Mazzoleni, C.; Franzo, G.; Priolo, F., *Nature* **2000**, *408*, 440-444.
41. Holman, Z. C.; Liu, C.-Y.; Kortshagen, U. R., *Nano Lett.* **2010**, *10*, 2661-2666.
42. Liu, C.-Y.; Holman, Z. C.; Kortshagen, U. R., *Nano Lett.* **2008**, *9*, 449-452.
43. Rosso-Vasic, M.; Spruijt, E.; Popovic, Z.; Overgaag, K.; van Lagen, B.; Grandidier, B.; Vanmaekelbergh, D.; Dominguez-Gutierrez, D.; De Cola, L.; Zuilhof, H., *J. Mater. Chem.* **2009**, *19*, 5926-5933.
44. Buriak, J. M., *Chem. Rev.* **2002**, *102*, 1271-1308.
45. Ciampi, S.; Harper, J. B.; Gooding, J. J., *Chem. Soc. Rev.* **2010**, *39*, 2158-2183.
46. Veinot, J. G. C., *Chem. Commun.* **2006**, 4160-4168.
47. Li, X.; He, Y.; Swihart, M. T., *Langmuir* **2004**, *20*, 4720-4727.
48. Hessel, C. M.; Rasch, M. R.; Hueso, J. L.; Goodfellow, B. W.; Akhavan, V. A.; Puvanakrishnan, P.; Tunnel, J. W.; Korgel, B. A., *Small* **2010**, *6*, 2026-2034.
49. Erogbogbo, F.; Yong, K.-T.; Roy, I.; Hu, R.; Law, W.-C.; Zhao, W.; Ding, H.; Wu, F.; Kumar, R.; Swihart, M. T.; Prasad, P. N., *ACS Nano* **2010**, *5*, 413-423.
50. Chen, B.; Flatt, A. K.; Jian, H.; Hudson, J. L.; Tour, J. M., *Chem. Mater.* **2005**, *17*, 4832-4836.
51. Lu, M.; Nolte, W. M.; He, T.; Corley, D. A.; Tour, J. M., *Chem. Mater.* **2009**, *21*, 442-446.
52. He, T.; Ding, H.; Peor, N.; Lu, M.; Corley, D. A.; Chen, B.; Ofir, Y.; Gao, Y.; Yitzchaik, S.; Tour, J. M., *J. Am. Chem. Soc.* **2008**, *130*, 1699-1710.
53. Xu, F. J.; Yuan, Z. L.; Kang, E. T.; Neoh, K. G., *Langmuir* **2004**, *20*, 8200-8208.
54. Xu, F. J.; Cai, Q. J.; Kang, E. T.; Neoh, K. G., *Langmuir* **2005**, *21*, 3221-3225.
55. Zhang, N.; Salzinger, S.; Deubel, F.; Jordan, R.; Rieger, B., *J. Am. Chem. Soc.* **2012**, *134*, 7333-7336.
56. Li, Z. F.; Ruckenstein, E., *Nano Lett.* **2004**, *4*, 1463-1467.
57. Clark, R. J.; Dang, M. K. M.; Veinot, J. G. C., *Langmuir* **2011**, *27*, 2073-2073.
58. Deubel, F.; Steenackers, M.; Garrido, J. A.; Stutzmann, M.; Jordan, R., *Macromol. Mater. Eng.* **2013**, *298*, 1160-1165.
59. Hua, F.; Swihart, M. T.; Ruckenstein, E., *Langmuir* **2005**, *21*, 6054-6062.
60. Moran, I. W.; Carter, K. R., *Langmuir* **2009**, *25*, 9232-9239.
61. Dung, M. X.; Choi, J.-K.; Jeong, H.-D., *ACS Appl. Mater. Interfaces* **2013**, *5*, 2400-2409.
62. Hessel, C. M.; Henderson, E. J.; Veinot, J. G. C., *Chem. Mater.* **2006**, *18*,

6139-6146.
63. Hessel, C. M.; Reid, D.; Panthani, M. G.; Rasch, M. R.; Goodfellow, B. W.; Wei, J.; Fujii, H.; Akhavan, V.; Korgel, B. A., *Chem. Mater.* **2011**, *24*, 393-401.
64. Liang, C. Y.; Krimm, S., *Journal of Polymer Science* **1958**, *27*, 241-254.
65. Lin-Vien, D.; Colthup, N. B.; Fateley, W. G.; Grasselli, J. G., CHAPTER 15 - Organosilicon Compounds. In *The Handbook of Infrared and Raman Characteristic Frequencies of Organic Molecules*, Academic Press: San Diego, 1991; pp 251-261.
66. Hessel, C. M.; Henderson, E. J.; Kelly, J. A.; Cavell, R. G.; Sham, T.-K.; Veinot, J. G. C., *J. Phys. Chem. C* **2008**, *112*, 14247-14254.
67. Khuong, K. S.; Jones, W. H.; Pryor, W. A.; Houk, K. N., *J. Am. Chem. Soc.* **2005**, *127*, 1265-1277.
68. Cicero, R. L.; Linford, M. R.; Chidsey, C. E. D., *Langmuir* **2000**, *16*, 5688-5695.
69. Regli, S.; Kelly, J. A.; Veinot, J. G. C., *MRS Symp. Proc.* **2011**, *1359*, null-null.
70. Li, Z. F.; Swihart, M. T.; Ruckenstein, E., *Langmuir* **2004**, *20*, 1963-1971.

Chapter 4

Surface-Induced Alkene Oligomerization: Does Thermal Hydrosilylation Really Lead to Monolayer Protected Silicon Nanocrystals?[3]

[3] A Portion of this chapter has been published:
Yang, Z.; Iqbal, M.; Dobbie, A. R.; Veinot, J. G. C., *J. Am. Chem. Soc.* **2013**, *135*, 17595-17601.

4.1 Introduction

Silicon nanocrystals (SiNCs) are intriguing materials because their properties differ substantially from those of their bulk counterparts.[1-3] Their tunable optoelectronic response, as well as low toxicity and biocompatibility, has garnered much attention, and prototype applications including light-emitting diodes, solar cells, and biological probes have been demonstrated.[4-7] Claims have also been made that hydride-terminated SiNCs can "split water" without any energy input.[8] While some exceptions exist,[9-12] most methods to prepare functionalized SiNCs begin with particles terminated with Si−H moieties that are, in turn, modified using various hydrosilylation strategies based upon widely known work on bulk and porous silicon.[13-19] These procedures provide alkyl and alkenyl surface groups that render SiNCs environmentally stable and compatible with common organic solvents. Broadly, hydrosilylation reactions add an Si−H bond across the C−C multiple bond; however, the exact mechanism depends upon the conditions employed (*e.g.*, thermal initiation, photochemical activation, metal-based catalysis, among others).

For reactions on bulk silicon surfaces, Linford and Chidsey have proposed that the reaction proceeds via a self-propagating chain reaction that leads to close-packed monolayers.[14] Investigations probing these reactions under

somewhat "ideal" ultra-high-vacuum (UHV) conditions with low monomer concentration, flat single-crystal surfaces, and single initiation sites support this mechanism.[20-22] Subsequently, numerous contributions have reported that analogous surface passivation of silicon nanostructures (*e.g.*, porous silicon, SiNCs) provides close packing of ligands.[17, 23-25] Still, the exact hydrosilylation mechanism remains elusive and the subject of ongoing discussions.[25-30] Unquestionably, typical reaction conditions are far from the ideal UHV scenario noted above, and the reaction pathways depend upon the experimental parameters employed. Among the various approaches, thermally initiated hydrosilylation is widely employed for SiNCs because it is not influenced by particle size and shape,[14-15, 31-32] it affords comparatively high yields, and there is no need to remove trace catalyst impurities. A commonly accepted thermal hydrosilylation mechanism requires sufficient heat ($T \geq 150$ °C) to homolytically cleave Si−H bonds to create silyl radicals that subsequently react with solution-borne terminal alkenes or alkynes. Once initiated, it is assumed the reaction propagates via a surface chain reaction similar to that proposed for bulk systems.[14] However, thermal hydrosilylation can occur at much lower temperatures (*e.g.*, 110 °C[31]), suggesting Si−H thermal cleavage is not the only mode of activation. Woods *et al.* invoked a kinetic model for hydrosilylation in which reaction initiation occurs via hydrogen abstraction by trace oxygen to explain low-temperature initiation.[26]

Regardless of the mode of initiation, surface silyl radicals react with unsaturated C−C bonds. To date, it has been reasonably assumed that these reactions yield monolayer coatings. However, faceted and curved surfaces of SiNCs differ substantially from ideal bulk Si substrates, solution-phase reactions with SiNCs are pseudo-homogeneous vs. heterogeneous for bulk surfaces, and typical concentrations of reagents bearing unsaturated C−C bonds are very high.[33-34] Given these differences, it is possible that surface silyl radicals formed in the initial stages of thermally induced reactions could lead to a variety of products. An important consideration that is largely absent from the discussion is that of oligomerization (or polymerization) of unsaturated solution species (*e.g.*, alkenes) leading to surface-bonded oligomers (or polymers). It has been revealed that silane molecules are efficient initiators for the polymerization of acrylate systems.[35] In this context, it is important to recall the exceptionally high resolution imaging of SiNCs by transmission electron microscopy (TEM) reported by Panthani et al.[36] that suggests particles may be covered by multilayers or polymerics. Similarly, our group recently reported the preparation of covalently linked SiNC/polystyrene hybrids obtained from thermal hydrosilylation conditions.[37]

Herein, we describe the results of a methodical investigation that was designed to critically examine the products from the thermally induced

hydrosilylation of SiNCs by exploring the influence of reaction temperature and atmosphere (*i.e.*, dry argon vs. air). Using well-established protocols developed in our laboratory, we prepared oxide-free, surface hydride-terminated SiNCs with different sizes upon HF etching of a hydrogen silsesquioxane-derived SiNC/SiO_2 composite.[32, 38] SiNC surfaces were subsequently functionalized via a thermally initiated hydrosilylation. Dodecene was chosen as the alkene of choice because it affords a wide reaction temperature range bracketing that required for Si−H cleavage (*i.e.*, 80−190 °C). Reaction progress is qualitatively evaluated by monitoring the visual transparency of the reaction mixture, which started as a cloudy yellow suspension and became transparent orange. Products were purified and evaluated using IR and PL spectroscopy, XPS, and mass spectrometry (MS).

4.2 Materials and Methods

4.2.1 Reagents and Materials

Hydrogen silsesquioxane (HSQ, trade name Fox-17, sold commercially as a solution in methyl isobutyl ketone) was purchased from Dow Corning Corp. (Midland, MI). Electronic-grade hydrofluoric acid (HF, 49% aqueous solution) was purchased from J. T. Baker. Methanol (reagent grade), toluene (reagent grade), ethanol (reagent grade), 1-dodecene (97%), and dodecane (99%) were purchased from Sigma-Aldrich and used as received.

4.2.2 Synthesis and Liberation of SiNCs

Preparation of Oxide-Embedded Silicon Nanocrystals (d = 3 nm): The solvent was removed from the stock HSQ solution under vacuum to yield white solid powders. HSQ solid (ca. 4 g) was placed in a quartz reaction boat, transferred to a Lindberg Blue tube furnace, and heated from ambient to a peak processing temperature of 1100 ℃ at 18 ℃ min^{-1} in a slightly reducing atmosphere (5% H_2/95% Ar). The sample was maintained at the peak processing temperature for 1 h. Upon cooling to room temperature, the resulting amber solid was ground into a fine brown powder using a two-step process. First, the solid was crushed using an agate mortar and pestle to remove large particles.

Further grinding was achieved using a Burrell wrist-action shaker upon shaking with high-purity silica beads for 5 h. The resulting SiNC/SiO_2 composite powders were stable for extended periods and stored in standard glass vials.

Preparation of Oxide-Embedded Silicon Nanocrystals (d = 5 and 8 nm): Following mortar and pestle grinding (*vide supra*), 0.5 g of SiNC/SiO_2 composite containing 3 nm SiNCs was transferred to a high-temperature furnace (Sentro Tech Corp.) for further thermal processing in an argon atmosphere. This procedure leads to particle growth while maintaining relatively narrow particle size distributions. In the furnace, the SiNC/SiO_2 composite was heated to appropriate peak processing temperatures at 10 ℃/min to achieve the target particle size (*i.e.*, 1200 ℃ for 5 nm NCs and 1300 ℃ for 8 nm NCs). Samples were maintained at the peak processing temperature for 1 h. After cooling to room temperature, the brown composites were ground using procedures identical to those noted above.

Liberation of SiNCs: Hydride-terminated SiNCs were liberated from the SiNC/SiO_2 composites using HF etching. First, 0.2 g of the ground SiNC/SiO_2 composite was transferred to a polyethylene terephthalate beaker equipped with a Teflon-coated stir bar. Ethanol (3 ml) and water (3 ml) were then added under mechanical stirring to form a brown suspension, followed by 3 mL of 49% HF aqueous solution. (Caution! HF can be dangerous and must be handled using

appropriate safety precautions and extreme care.) After 1 h of etching in subdued light, the suspension appeared orange/yellow. Hydride-terminated SiNCs were subsequently extracted from the aqueous layer into ca. 30 mL of toluene by multiple (*i.e.*, 3 × 10 mL) extractions. The SiNC toluene suspension was transferred to test tubes, and the SiNCs were isolated by centrifugation at 3000 rpm.

4.2.3 Thermal Hydrosilylation and Purification

Thermal Functionalization of Dodecyl-Modified SiNCs: After decanting the toluene supernatant, the resulting hydride-terminated particles were redispersed into ca. 20 mL of dodecene to yield a cloudy suspension, which was transferred to a dry 100 mL Schlenk flask equipped with a magnetic stir bar and attached to a Schlenk line. The flask was evacuated and backfilled with argon three times to remove air and residual toluene from the solution. The temperature was increased to the set processing temperatures (*i.e.*, 100, 120, 140, 160, and 190 ℃, respectively), and the reaction was left stirring for a minimum of 15 h. For those comparison reactions in air atmosphere, the flask was reconnected to air atmosphere before the heating process.

Thermal Functionalization of SiNCs with Diluted Dodecene Solution: The dodecene was diluted by dodecane to form two solutions with different

concentration: (1) 5 mL of dodecene/15 mL of dodecane and (2) 2.5 mL of dodecene/17.5 mL of dodecane. Following the extraction and centrifugation (*vide supra*), hydrideterminated SiNCs were redispersed into these solutions, respectively. The mixed solution, which was cloudy yellow, was further transferred to a dry 100 mL Schlenk flask equipped with a magnetic stir bar and attached to a Schlenk line. Similarly, the flask was evacuated and backfilled with argon three times. The temperature was set at 190 ℃, and the reaction was left stirring for a minimum of 15 h.

SiNC Purification: Following thermal hydrosilylation, the solution was evenly dispensed into 1.5 mL centrifuge tubes (ca. 0.3 mL each). Next, ca. 1.2 mL of 1:1 methanol/ethanol mixture was added into each tube, resulting in a cloudy yellow dispersion. The precipitate was isolated by centrifugation in a high-speed centrifuge at 17000 rpm for 15 min. The supernatant was decanted, and the particles were redispersed in a minimum amount of toluene and subsequently precipitated by addition of the 1:1 methanol/ethanol again. The centrifugation and decanting procedure was repeated twice. Finally, the purified-functionalized SiNCs were redispersed in toluene, filtered through a 0.45 μm PTFE syringe filter, and stored in vials for further use.

4.2.4 Control Reactions

First, 10 mL of neat dodecene was transferred to a dry 100 mL Schlenk flask equipped with a magnetic stir bar and attached to a Schlenk line. The flask was evacuated and backfilled with argon three times. The temperature was then increased similarly to the thermal hydrosilylation reactions (*vide supra, i.e.*, 100, 120, 140, 160, and 190 ℃, respectively) for a minimum of 15 h. For those control samples heated under air atmosphere, the flask was reconnected to air atmosphere before the heating process.

4.2.5 Material Characterization and Instrumentation

PL spectra were obtained by irradiation of a quartz vial containing the sample toluene solution with a 441 nm line of a GaN laser (Wicked Laser Arctic Blue, ~600 mW). Emitted photons were collected with a fiber optic connected to an Ocean Optics USB2000 spectrometer. FT-IR spectroscopy was performed on powder samples using a Nicolet Magna 750 IR spectrophotometer. X-ray photoelectron spectra were acquired in energy spectrum mode at 210 W, using a Kratos Axis Ultra X-ray photoelectron spectrometer. Samples were prepared as films drop-cast from solution onto a copper foil substrate. For nanostructure-assisted laser desorption/ionization (NALDI)-MS sample

preparation, 1 μL of the sample solution was spotted onto a Bruker Daltonics NALDI target and air-dried. Mass spectra were obtained in the positive/negative reflectron mode using a Bruker Daltonics (Bremen, Germany) UltrafleXtreme MALDI TOF/TOF mass spectrometer. EI-MS spectra were recorded on a Kratos MS-50 (high resolution, electron impact ionization). Samples were loaded by direct probe.

4.3 Results and Discussion

4.3.1 Low Temperature Thermal Hydrosilylation and Oligomerization

FT-IR analysis is the most commonly employed method for evaluating SiNCs surface modification and provides valuable information regarding covalent attachment of the surface groups. The FT-IR spectrum of Si−H-terminated SiNCs (Figure 4-1a) shows strong absorptions attributed to $Si-H_x$ (ca. 2100 and 850 cm^{-1}, respectively). Following hydrosilylation (see Figure 4-1), absorptions associated with Si−H are replaced by intense vibrations at 2650−2900 and 1380−1470 cm^{-1}, characteristic of alkyl functionalities and consistent with surface modification.[32] Of particular importance to the present discussion, these features cannot be used to distinguish among monolayers, oligomers, or polymers. Weak absorptions at ca. 1100 cm^{-1} are also observed that indicate some limited surface oxidation of SiNCs has occurred. The oxidation state(s) of the SiNC cores was(were) evaluated using XPS (Figure 4-2). An emission at 99.3 eV routinely attributed to Si(0) was noted, while other components at 100.3, 101.3, 102.4, and 103.4 eV were assigned to the functionalized surface atoms as well as Si sub-oxides.[39]

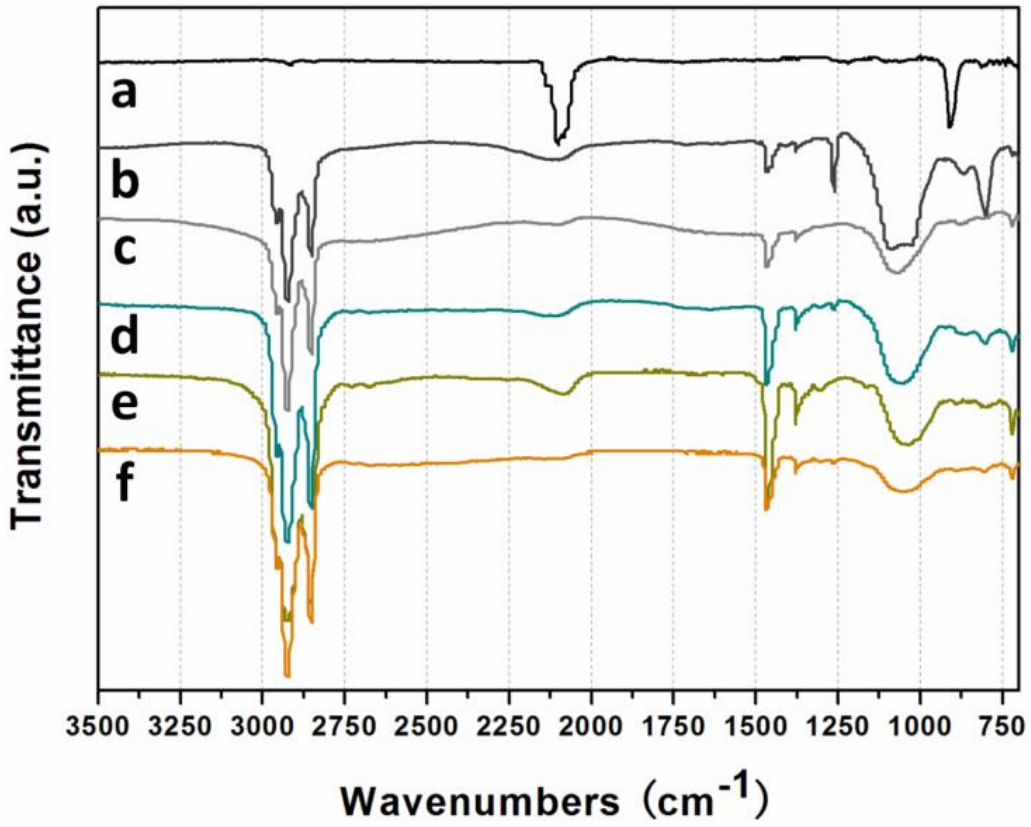

Figure 4-1: FTIR spectra of 3 nm (a) hydride-terminated and (b-f) dodecyl passivated Si functionalized under argon atmosphere at various temperatures: (b) 100 ℃, (c) 120 ℃, (d) 140 ℃, (e) 160 ℃ and (f) 190 ℃.

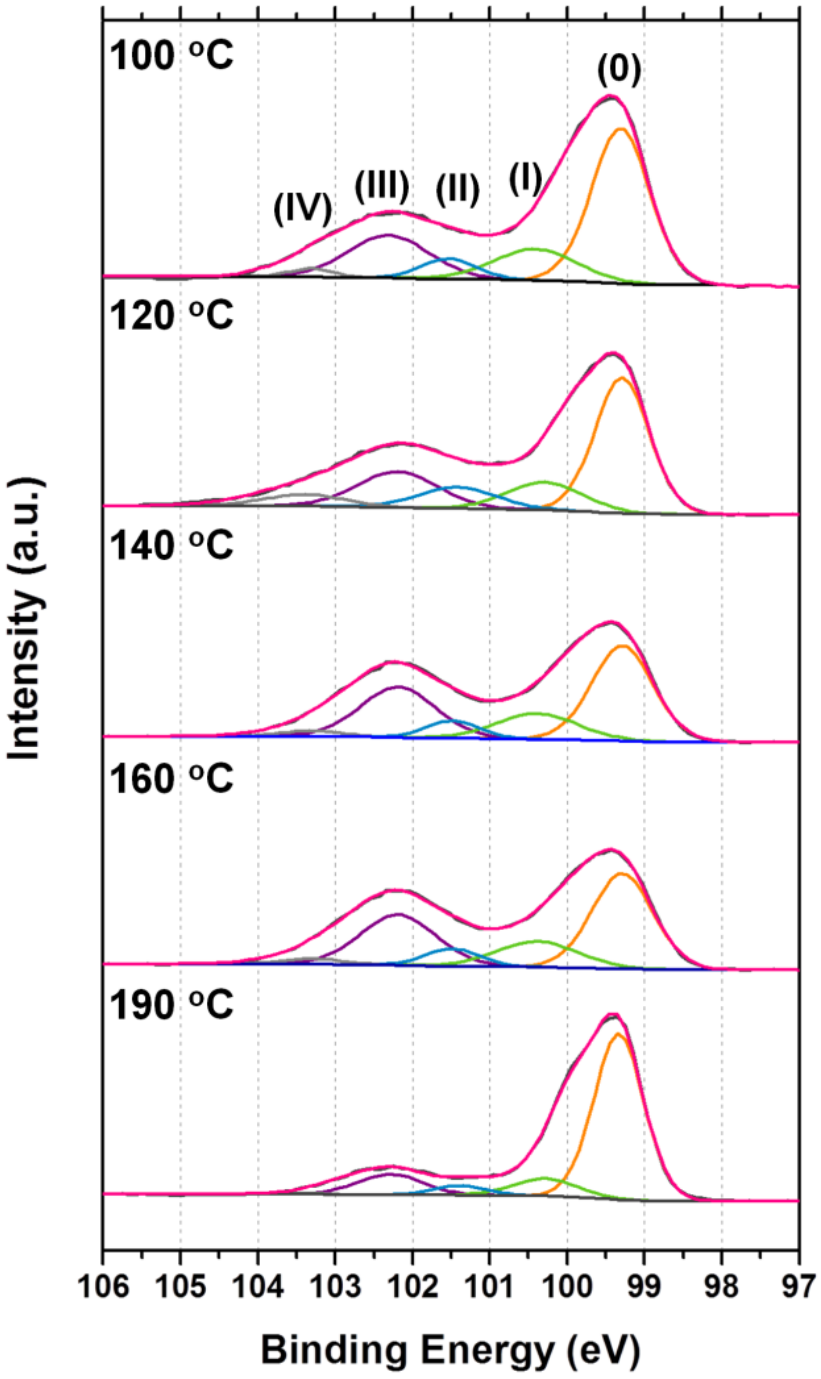

Figure 4-2: High-resolution XPS spectra of silicon (2p) for dodecyl passivated silicon nanocrystals functionalized under Ar atmosphere at various temperature (100 ℃ – 190 ℃). Fitting results are shown for the silicon spectrum with Si $2p_{3/2}$ signal . The Si $2p_{1/2}$ signals have removed for clarity.

MS was employed to evaluate the identity of SiNC surface groups. In light of the strong covalent Si−C bonds that bind the alkyl-based moieties to the SiNCs,[40] NALDI was employed. The MS data for functionalized particles obtained from a reaction performed at 190 ℃ under inert Ar atmosphere are shown in Figure 4-3. No fragments associated with the molecular weight of dodecene (MW = 168.3) were detected, consistent with effective purification. The fragmentation pattern observed is complex; however, this is not unexpected when comparing the various bond strengths at the SiNC surface (*i.e.*, Si−Si, 210−250; Si−C, 369; and C−C, 292−360 kJ mol^{-1}).[40] Because the Si−Si linkage is the weakest of the surface bonds, it will cleave preferentially, and liberated groups are expected to include differing numbers of silicon atoms. This complexity precludes definitive assignment of individual MS signals. Still, important insight into the nature of the SiNC surface species can be obtained when considering series of signals that are separated by m/z = 168.3, consistent with the loss of a dodecyl repeat unit from an oligomer or polymer. Further evaluation of the fragmentation pattern suggests that species liberated from the NC surfaces consist of two (purple and orange labels), three (blue labels), and four (green labels) dodecyl repeat units, consistent with surface oligomerization. Even more telling, when a blank sample (*i.e.*, pure dodecene, without SiNCs) was also heated following the identical procedure, only a trace amount of dimer (*i.e.*, MW = 336.4)

was detected (Figure 4-4). These observations suggest that high-temperature functionalization of hydride-terminated SiNCs with alkenes leads to ligand oligomerization.

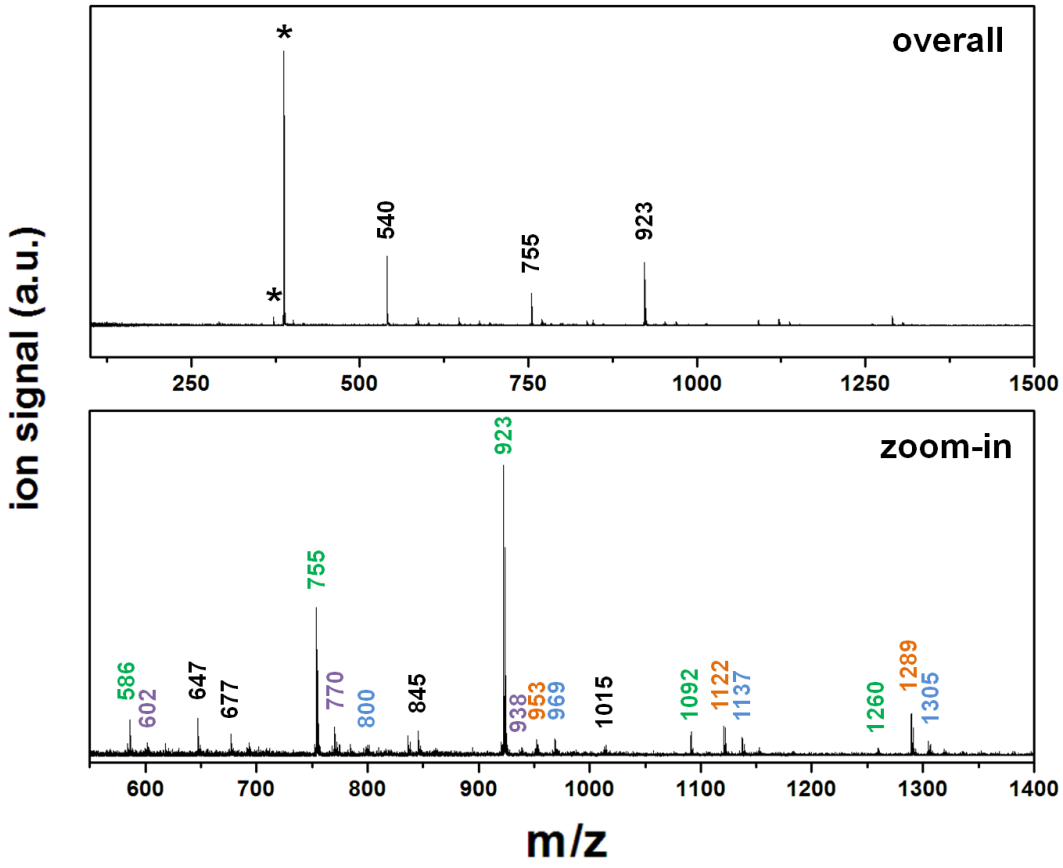

Figure 4-3: NALDI mass spectra of 3 nm dodecyl-passivated SiNCs functionalized at 190 ℃ under argon. Numbers in different colors indicate the gap corresponding to a dodecene unit (*i.e.*, *m/z* = 168.3). Numbers in black are assigned to unspecific fragments. Asterisks indicate background signals.

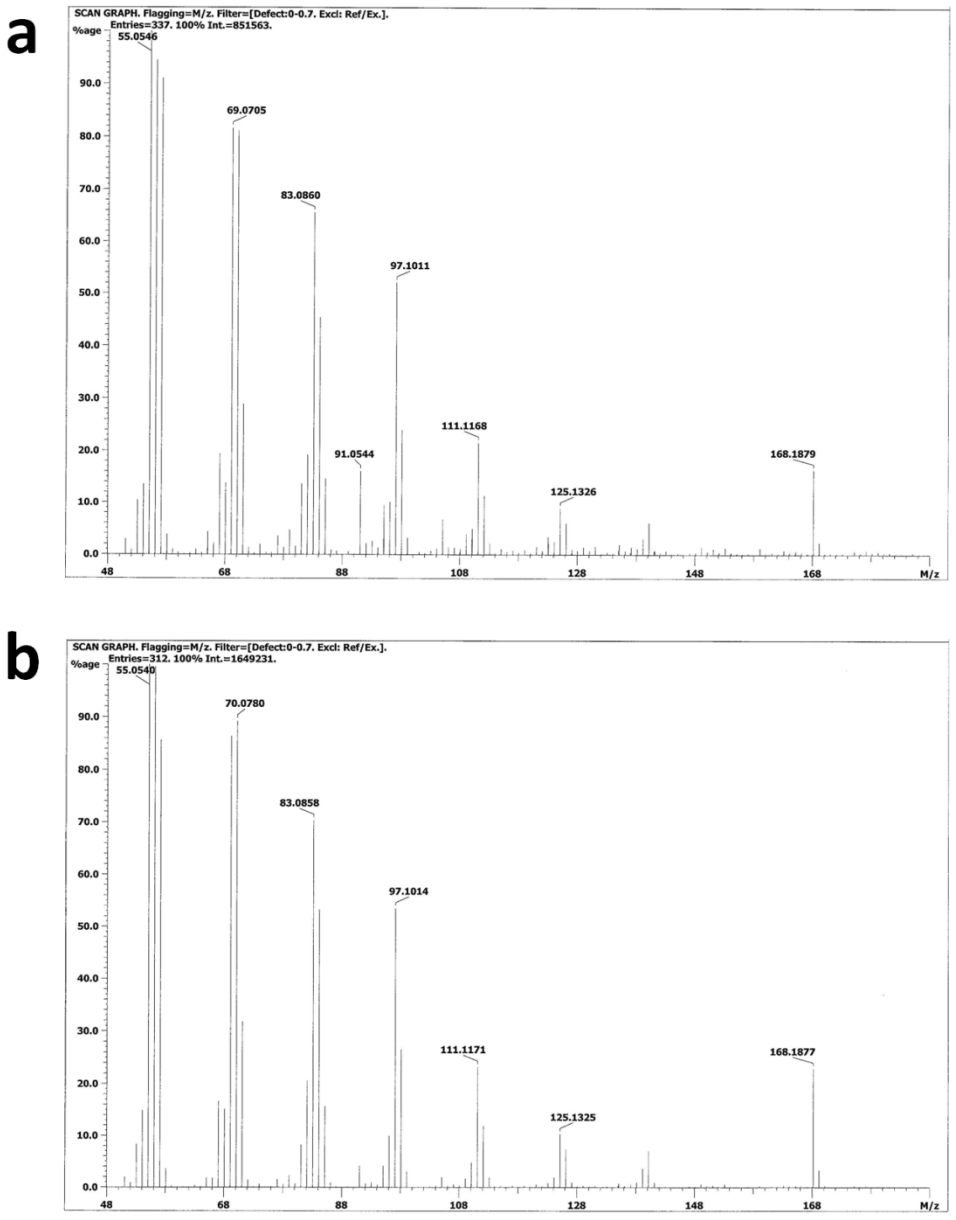

Figure 4-4. EI mass spectra of neat dodecene after heating under argon atmosphere at various temperatures: (a) 100, (b) 120, (c) 140, (d) 160 and (e) 190 ℃.

(**Figure 4-4 continued)**

c

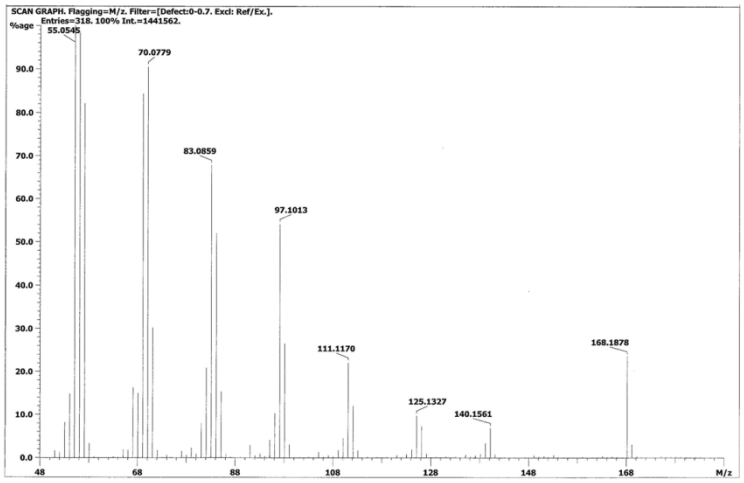

d

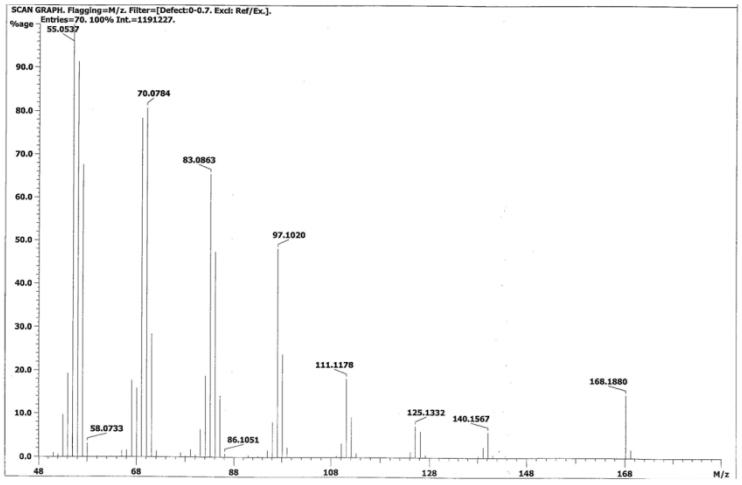

e

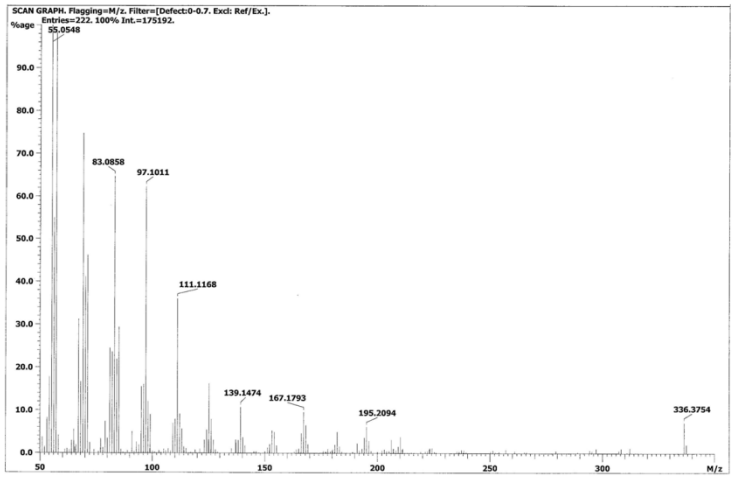

Based upon the generally accepted mechanism that involves the homolytic cleavage of the Si−H bond, it is expected that reaction temperature will play a crucial role in thermal hydrosilylation. By extension, temperature is certainly a key factor in the formation of oligomers. In this context, we explored how changes in reaction temperature impacted the product distribution for reactions carried out at predetermined temperatures between 80 and 160 ℃. With heating to 80 ℃, no qualitative changes in the appearance of the reaction mixture were noted, even after prolonged (*i.e.*, 3 days) heating. This observation is expected, given that homolytic cleavage of Si−H requires temperatures of at least 150 ℃.[40] To our surprise, reactions performed at 100 ℃ afforded transparent orange SiNC solutions after 72 h; when they were heated to 120 and 140 ℃, only 15 h was required. Removal of solvent provided a dark brown powder. IR and XPS analyses of samples prepared at 100, 120 and 140 ℃ confirmed surface functionalization and limited oxidation (Figures 4-1 and 4-2). No obvious evidence of ligand oligomerization was detected in the NALDI-MS analysis of products from reactions heated to 100 ℃, suggesting monolayer formation. Spectral signatures of products prepared at 120 and 140 ℃ (Figures 4-5 and 4-6) do suggest oligomerization. More specifically, samples prepared at 120 ℃ show a series of four peaks separated by 168.3 Da (green labels in Figure 4-5), consistent with the presence of dodecyl trimers. Similarly, products from reactions at 140

and 160 ℃ show peaks separated by 168.3 Da. Again, neat dodecene was heated under identical conditions, and only signals attributable to the monomer were detected (Figure 4-4), indicating that oligomer formation relies upon the presence of the SiNCs and the hydrosilylation process.

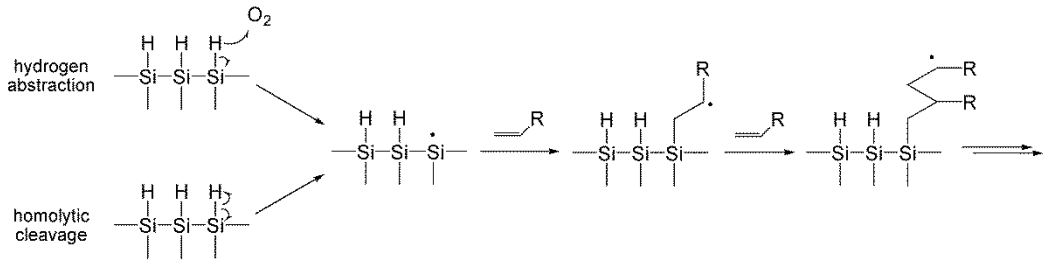

Scheme 4-1: Proposed mechanism of thermal hydrosilylation and ligand oligomerization processed at different temperatures, involving homolytic cleavage of Si−H bond and hydrogen abstraction by oxygen.

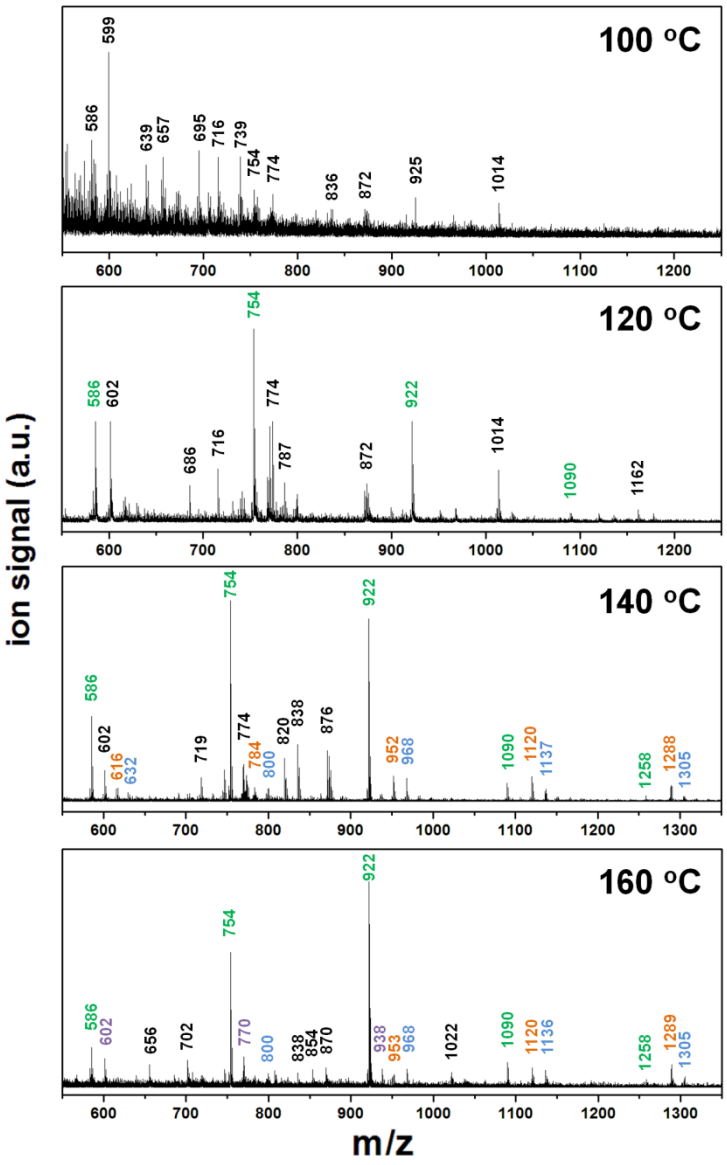

Figure 4-5: Zoom-in NALDI mass spectra of 3 nm dodecyl passivated Si nanocrystals functionalized at different temperatures under argon.

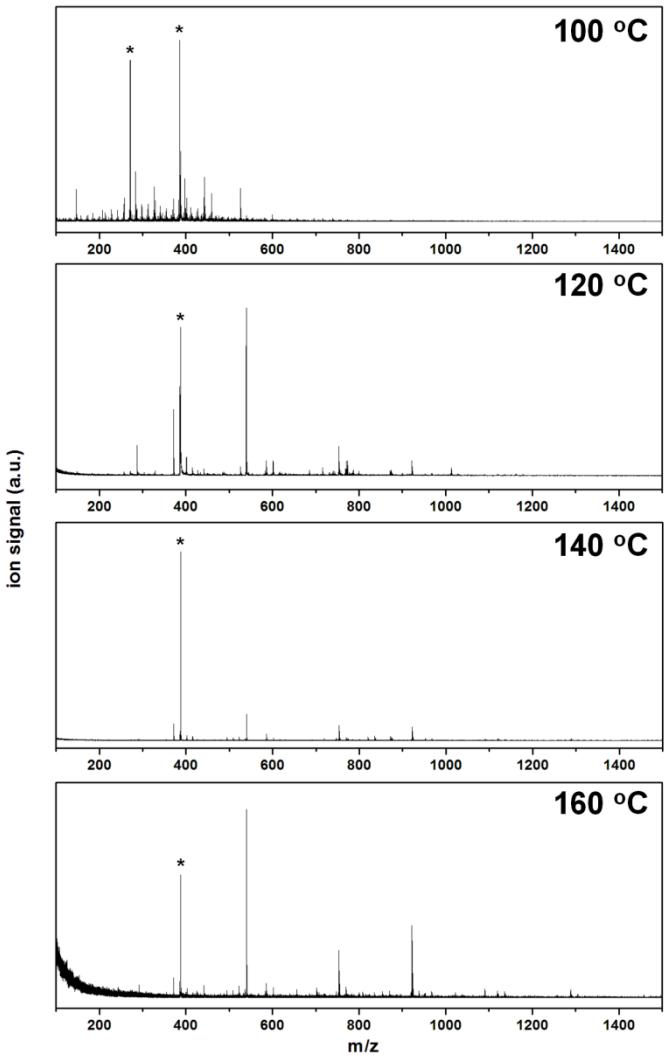

Figure 4-6: Overall NALDI mass spectra of 3 nm dodecyl passivated Si nanocrystals functionalized at different temperatures under argon. Note: * indicate background signals.

Our observations, that thermally induced hydrosilylation of SiNC surfaces occurs in ambient and subdued light at $100 \leq T \leq 140$ °C, contradict the widely accepted mechanism involving the thermally induced formation of silyl radicals

via homolytic cleavage of surface Si−H bonds.[40] One explanation for our findings was proposed by Woods et al., who considered hydrogen abstraction by trace oxygen while simulating a kinetic model for the hydrosilylation initiation step.[26] Those authors found that the computationally determined activation energy was much lower when trace oxygen was considered. This is in good agreement with our observations of low-temperature hydrosilylation and supports the hypothesis that hydrogen abstraction is another initiation pathway. In the context of our observations, we provide a possible mechanism of thermal hydrosilylation/oligomerization (see Scheme 4-1). We propose two reasonable modes of initiation: homolytic cleavage and hydrogen abstraction. Subsequently, the surface dangling bond (or silyl radical) reacts with a terminal alkene, producing a Si−C linkage and a secondary radical that reacts with additional terminal alkenes, leading to chain propagation and the formation of a surface-bonded oligomer. Because there is no evidence of oligomers in our control dodecene samples prepared at < 190 ℃, it is clear that the silyl radical is crucial for ligand oligomerization. This is further supported by our observations that more and longer oligomers are detected in the samples functionalized at higher temperatures.

4.3.2 Ligand Oligomerization in Air and Mechanism Study

If the silyl radical is responsible for the formation of oligomers, then reaction of Si−H-terminated SiNCs with dodecene in the presence of oxygen should lead to more oligomerization. To elucidate this potential "oxygen effect" on hydrosilylation/oligomerization, we performed thermal-induced hydrosilylation in air. Potential nitrogen influence is readiley excluded by control tests, whose results are similar to those obtained by reactions under Ar. Reactions performed at 100 ℃ provided only surface-oxidized SiNCs. Upon increasing the reaction temperature to 120 ℃, partially functionalized SiNCs bearing alkyl-based ligands and surface oxide were obtained. It is not surprising that silicon surfaces get oxidized when exposed to air; however, when the reaction was performed at higher temperatures, hydrosilylation proceeded qualitatively more quickly (*i.e.*, 140 ℃, ca. 3 h; 160 ℃, ca. 1 h; 190 ℃, ca. 30 min.) than the identical reactions carried in an argon atmosphere. The resulting products were obtained as photoluminescent transparent orange solutions. Unlike samples prepared in Ar atmosphere (*vide supra*), these solutions afforded a viscous orange oil upon solvent removal suggesting polymer or oligomer formation. IR spectra (Figure 4-7) confirmed effective passivation with alkyl chains and suggested that the degree of surface oxidation decreases with higher temperature, as evidenced by

Si−O−Si stretching at ca. 1100 cm^{-1}. Detailed XPS analysis of the Si oxidation states for samples obtained at 140, 160, and 190 ℃ are shown (Figure 4-8). Not unexpectedly, oxide components are more dominant than those obtained from samples reacted under Ar, and, consistent with our IR data, we note a decrease in oxidation with higher reaction temperature. As anticipated, a slight blue-shift was observed in PL spectra (Figure 4-9), which could be assigned to surface oxidation states.[41-42] The observation of faster hydrosilylation in air at higher temperature supports the eceoncept of an initiation pathway involving silyl radical formation by oxygen abstraction. Furthermore, the present observations that functionalization does not occur at lower temperature (*i.e.*, 100 and 120 ℃) suggest a competitive relationship between the oxidation and hydrosilylation reactions and that higher temperature favors hydrosilylation.

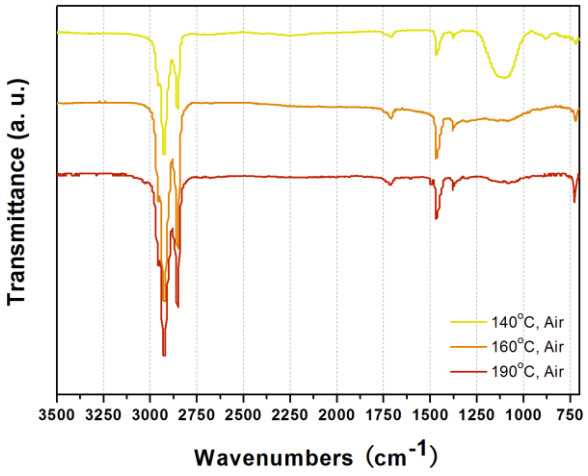

Figure 4-7: IR spectra of 3 nm dodecyl passivated Si functionalized under air at various temperatures.

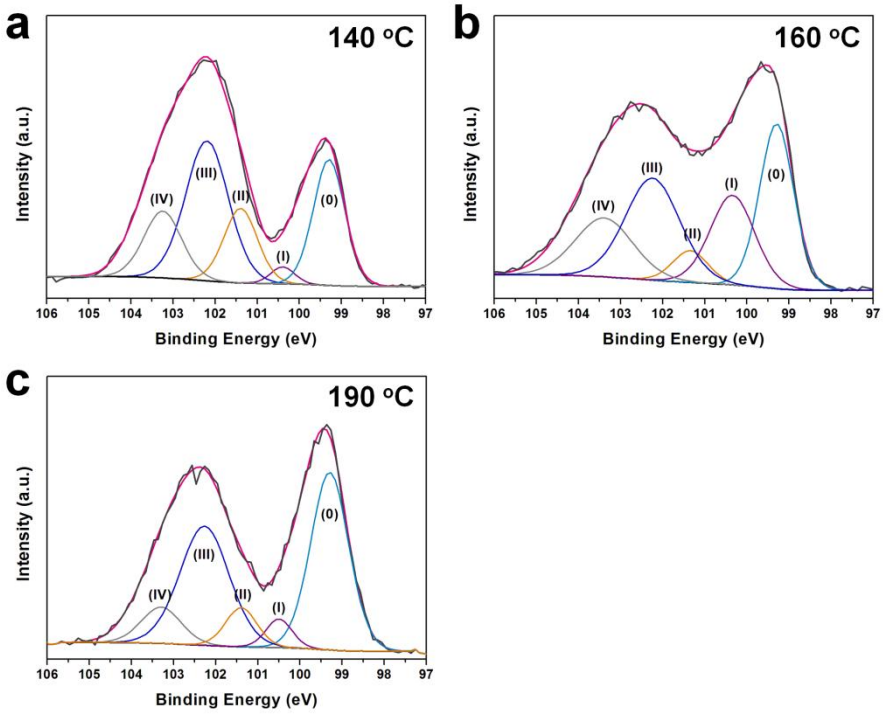

Figure 4-8: High-resolution XPS spectra of silicon (2p) for dodecyl passivated silicon nanocrystals functionalized under air at various temperatures. Fitting results are shown for the silicon spectrum with Si $2p_{3/2}$ signal shown. The Si $2p_{1/2}$ signals have been removed for clarity.

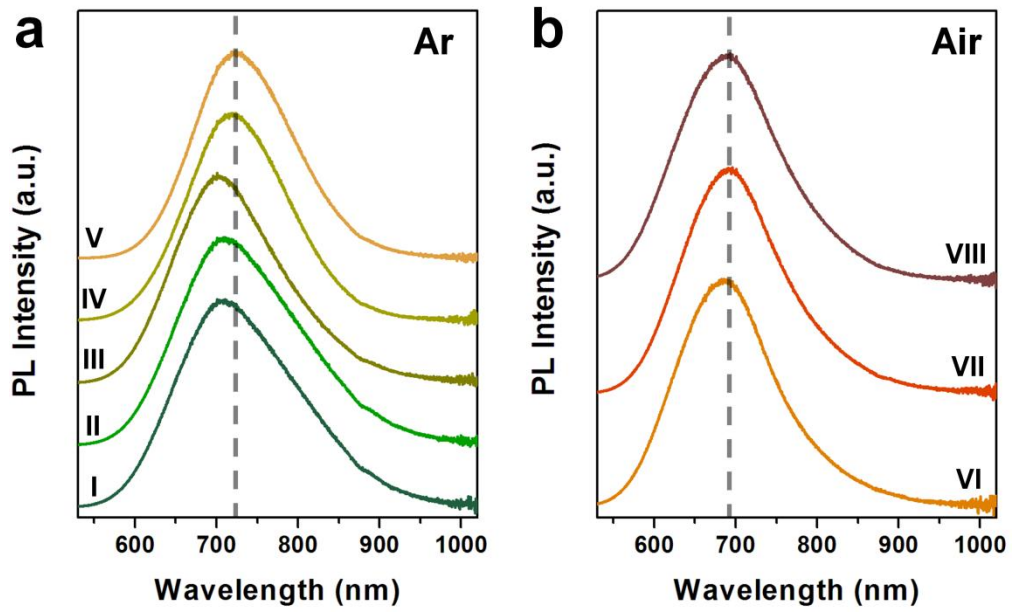

Figure 4-9: PL spectra of 3 nm dodecyl functionalized under (a) argon and (b) air environments at various processing temperatures: (I) 100, (II) 120, (III,VI) 140, (IV,VII) 160, and (V,VIII) 190 ℃. The dotted lines indicate the wavelength value corresponding to the peak maxima of spectra V and VIII.

Again, NALDI-MS analysis of the functionalized SiNCs showed no signals attributed to free dodecene monomer, and there was clear indication of dodecene oligomers (Figures 4-10 and 4-11). Similar to our inert atmosphere functionalization, when air is included in the reaction, we note that a higher reaction temperature generates more and longer dodecyl oligomers (*i.e.*, up to n = 7). Comparing the products obtained from inert and air reaction atmospheres, we find that air provides longer oligomer chains (*i.e.*, n_{air} = 7 vs n_{Ar} = 4). As was

the case with all dodecene controls, no oligomer was detected by EI-MS upon heating to 140 ℃ in the absence of hydride-terminated SiNCs; trace quantities of dimer and trimer were detected after heating to 160 and 190 ℃, respectively (Figure 4-12). These control samples clearly highlight the role of Si−H terminated SiNCs in dodecene oligomerization.

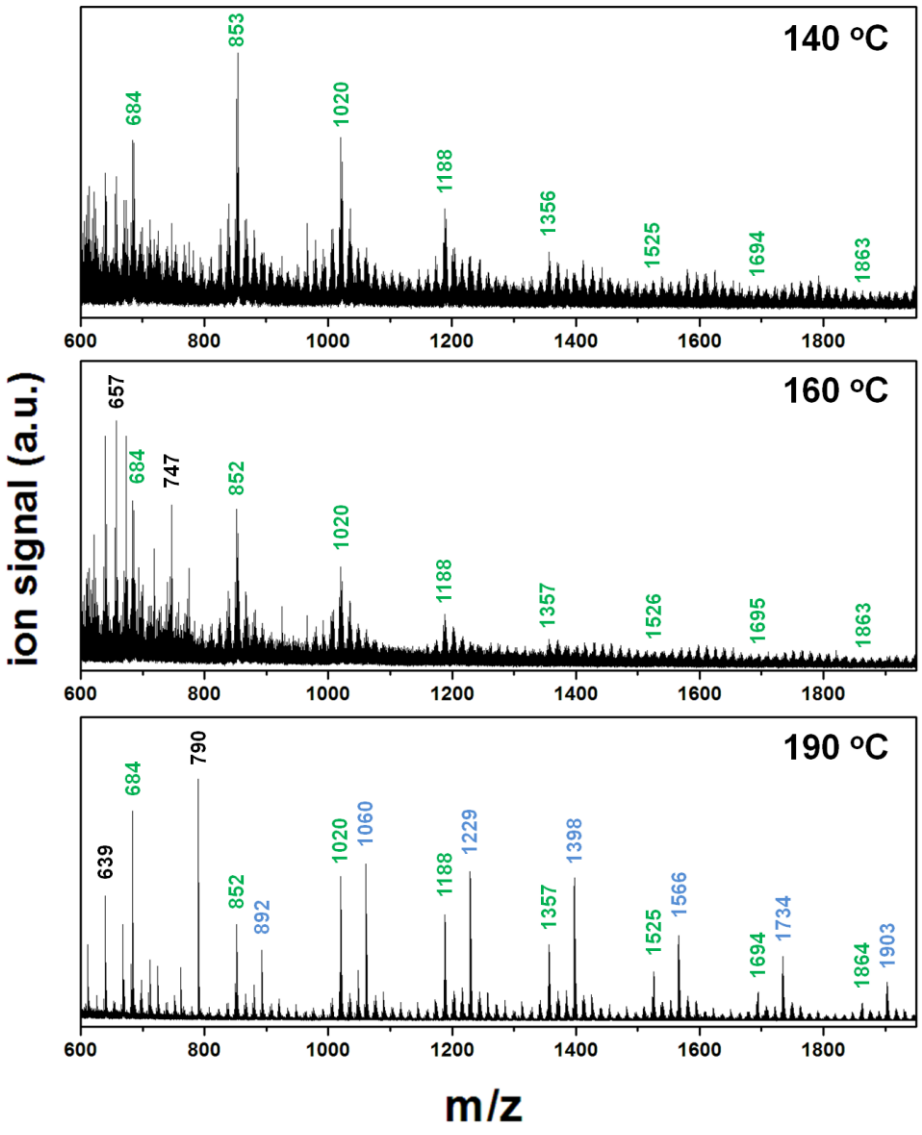

Figure 4-10: Zoom-in NALDI mass spectra of 3 nm dodecyl-passivated SiNCs functionalized at different temperatures under an air atmosphere.

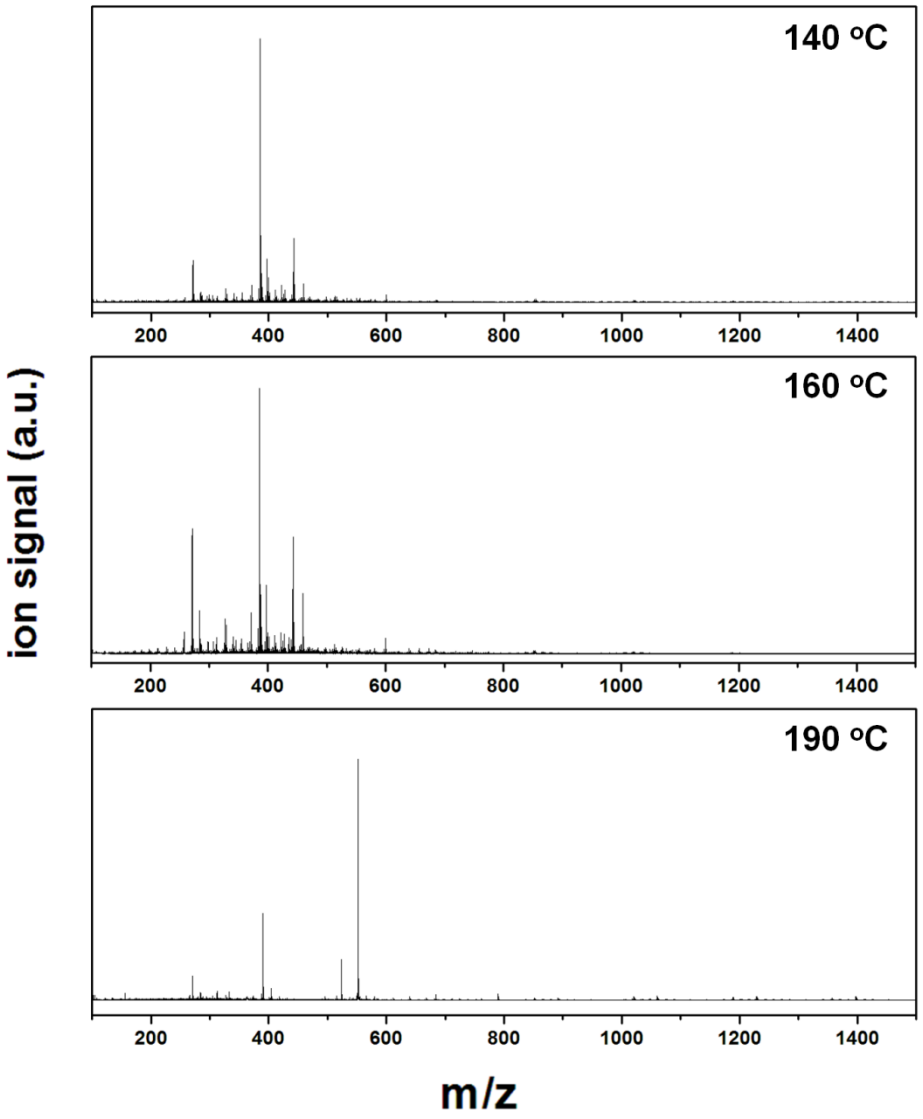

Figure 4-11: Overall NALDI mass spectra of 3 nm dodecyl passivated Si nanocrystals functionalized at different temperatures under air.

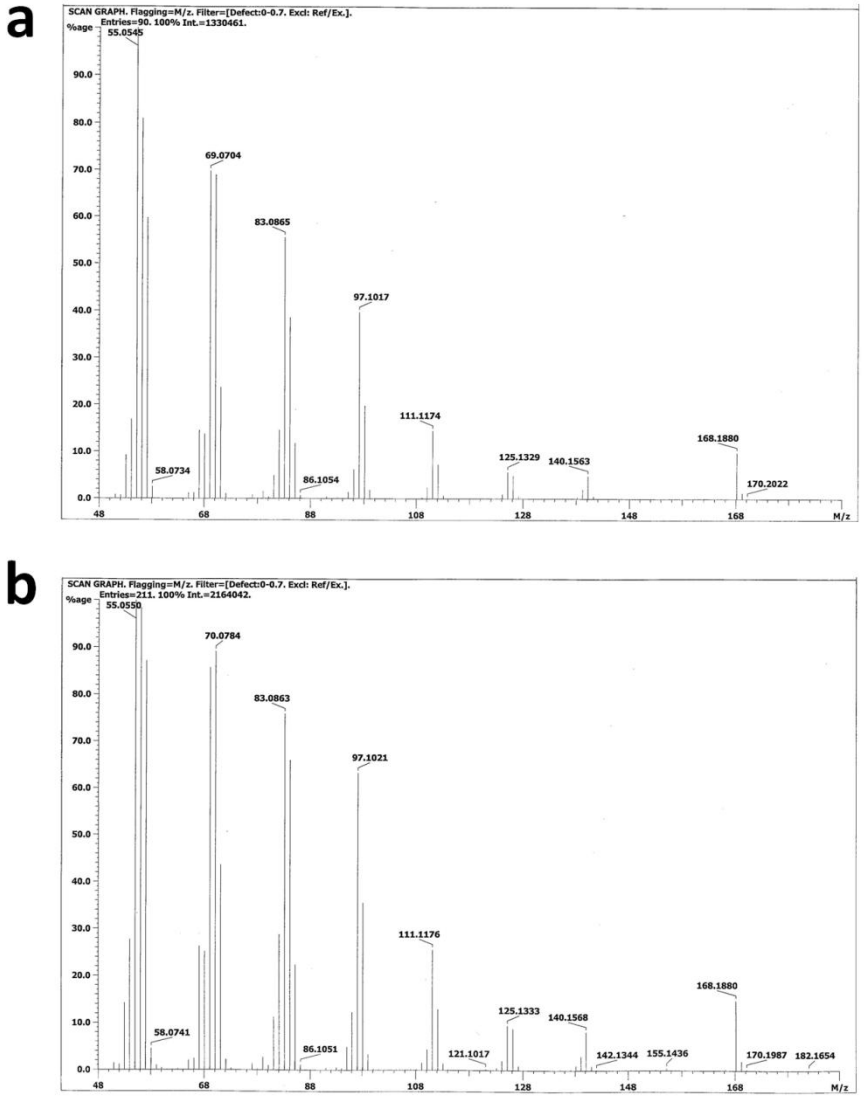

Figure 4-12: EI mass spectra of neat dodecene after heating under air at various temperatures: (a) 100 ℃, (b) 120 ℃, (c) 140 ℃, (d) 160 ℃ and (e) 190 ℃.

(**Figure 4-12 continued)**

c

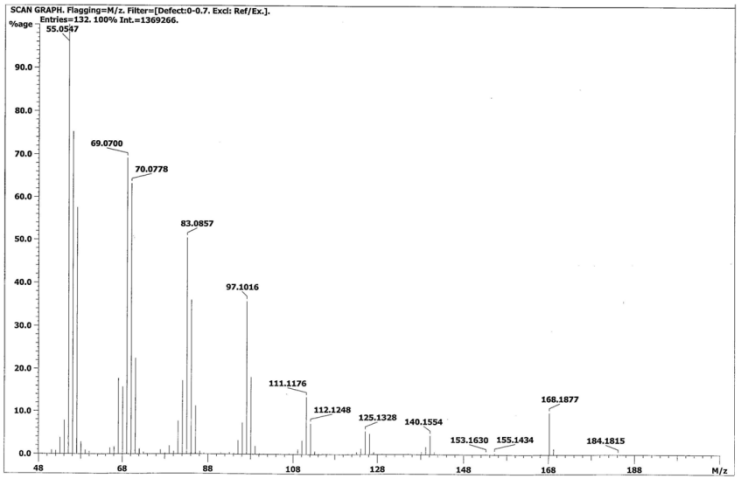

d

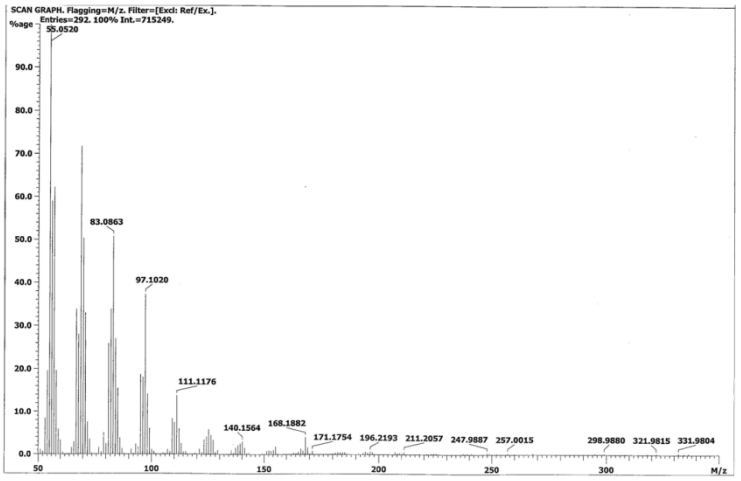

e

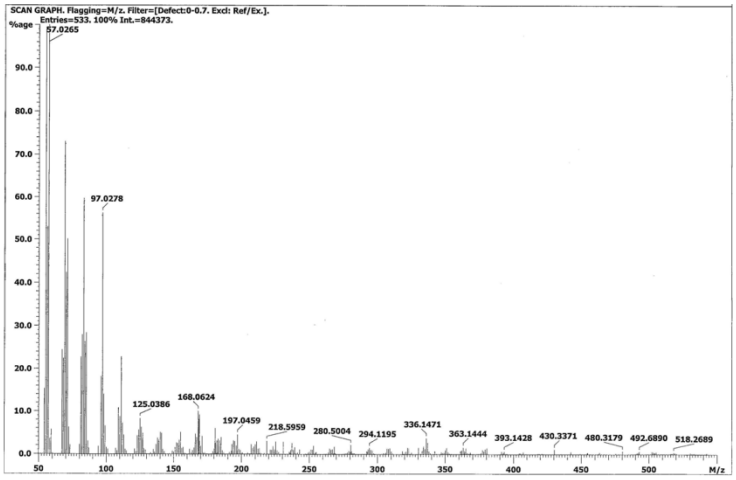

Having identified that surface functionalization of SiNCs via thermal hydrosilylation yields complex mixtures of surface products, we endeavored to identify if this reaction exhibited size dependence. In this regard, we performed reactions with d = 5 and 8 nm SiNCs in dodecene and observed identical trends associated with oligomer formation, reaction temperature, and atmosphere (Figures 4-13 and 4-14). We also discovered that decreasing the dodecene concentration led to lower oligomer production. When reactions were performed at 190 ℃ in argon using dodecene diluted with dodecane (*i.e.*, 5 mL of dodecene in 15 mL of dodecane, and 2.5 mL of dodecene in 17.5 mL of dodecane), we noted a marked decrease in oligomer formation (Figure 4-15).

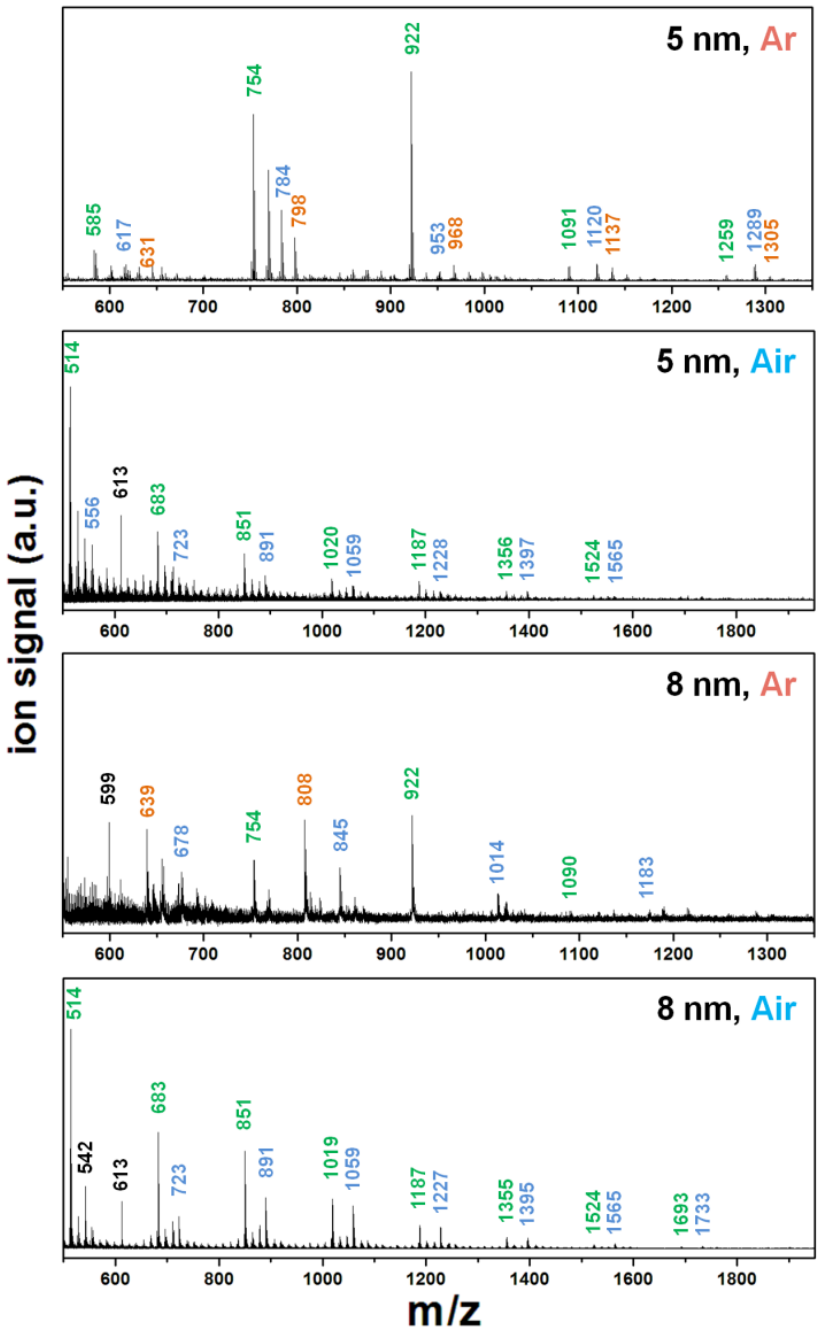

Figure 4-13: Zoom-in NALDI mass spectra of 5 and 8 nm dodecyl passivated SiNCs functionalized at 190 ℃ under argon and air atmosphere. The numbers in different colors indicate the gap corresponding to a dodecene unit. The numbers in black are attributed to unidentified fragments.

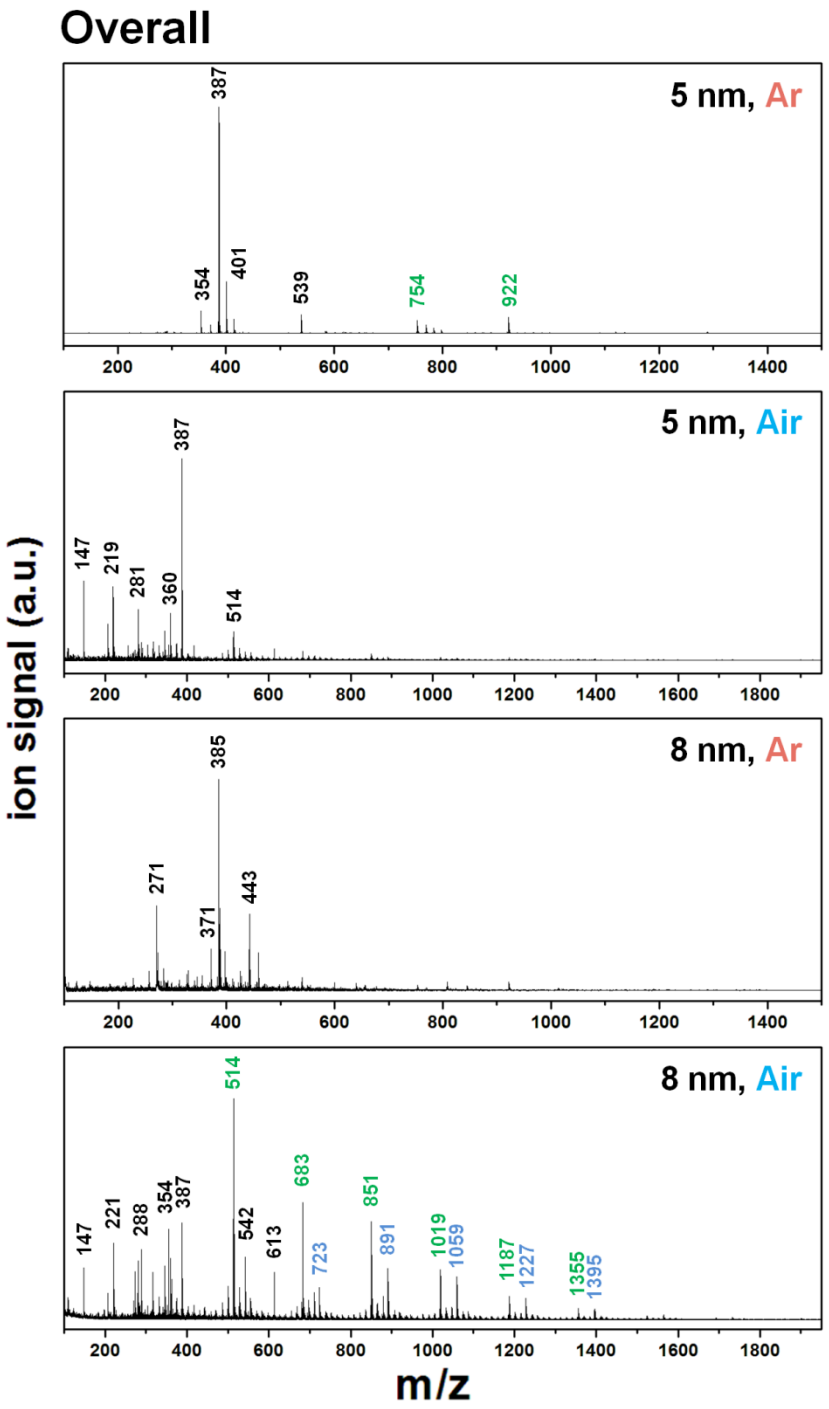

Figure 4-14: Overall NALDI mass spectra of 5 nm and 8 nm dodecyl passivated Si nanocrystals functionalized at 190 ℃ under argon and air atmosphere.

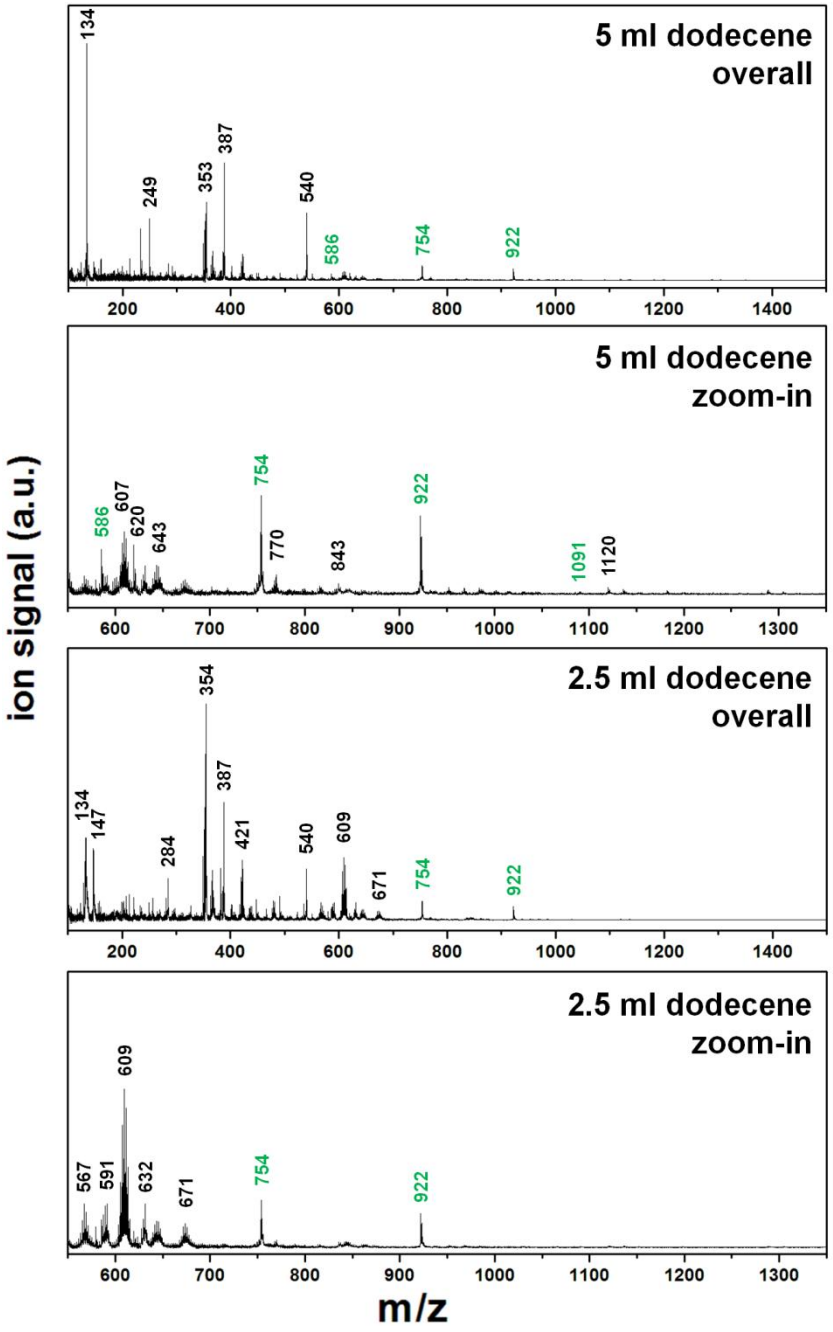

Figure 4-15: NALDI mass spectra of 3 nm dodecyl passivated Si nanocrystals functionalized with dodecene solution diluted by dodecane (*i.e.*, 5 ml dodecene in 15 ml dodecane and 2.5 ml dodecene in 17.5 ml dodecane, repsectively) at 190 ℃ under argon and air atmosphere.

4.4 Conclusions

In conclusion, this chapter describes the first reported detailed investigation into the nature of the surface species on freestanding SiNCs obtained from thermally induced hydrosilylation. We show convincing evidence that ligand oligomerization occurs under a variety of conditions and confirm that hydrogen abstraction by oxygen enables hydrosilylation to proceed at lower temperature through the production of silyl radicals. The resulting silyl radicals react with the unsaturated C=C bond, which subsequently promotes chain propagation and ultimately generates ligand oligomers on SiNC surfaces. These findings are supported by similar reactions under an air atmosphere, in which both rate of reaction and amount ofsurface oligomers increased. Based on this systematic study, it is clear that comparatively low temperature, inert atmosphere, and dilute ligand concentration are crucial to limit surface oligomerization and to obtain monolayer surface coverage. Furthermore, it should be possible to apply chemical trapping (*e.g.*, butylated hydroxyanisole or butylated hydroxytoluene) to operate with tolerable quantities of oxygen.

4.5 References

1. Brus, L., *J. Phys. Chem.* **1994,** *98*, 3575.
2. Ding, Z.; Quinn, B. M.; Haram, S. K.; Pell, L. E.; Korgel, B. A.; Bard, A. J., *Science* **2002,** *296*, 1293.
3. Heitmann, J.; Müller, F.; Zacharias, M.; Gösele, U., *Adv. Mater.* **2005,** *17*, 795.
4. Zhong, Y.; Peng, F.; Bao, F.; Wang, S.; Ji, X.; Yang, L.; Su, Y.; Lee, S.-T.; He, Y., *J. Am. Chem. Soc.* **2013,** *135*, 8350.
5. Liu, J.; Erogbogbo, F.; Yong, K.-T.; Ye, L.; Liu, J.; Hu, R.; Chen, H.; Hu, Y.; Yang, Y.; Yang, J.; Roy, I.; Karker, N. A.; Swihart, M. T.; Prasad, P. N., *ACS Nano* **2013,** *7*, 7303.
6. Cheng, K.-Y.; Anthony, R.; Kortshagen, U. R.; Holmes, R. J., *Nano Lett.* **2010,** *10*, 1154.
7. Jang, H.; Pell, L. E.; Korgel, B. A.; English, D. S., *J. Photochem. Photobiol. A* **2003,** *158*, 111.
8. Erogbogbo, F.; Lin, T.; Tucciarone, P. M.; LaJoie, K. M.; Lai, L.; Patki, G. D.; Prasad, P. N.; Swihart, M. T., *Nano Lett.* **2013,** *13*, 451.
9. Bley, R. A.; Kauzlarich, S. M., *J. Am. Chem. Soc.* **1996,** *118*, 12461.
10. Liu, Q.; Kauzlarich, S. M., *Mater. Sci. Eng., B* **2002,** *96*, 72.
11. Bryan, D. R.; Jonathan, G. C. V., *Nanotechnology* **2005,** *16*, 732.
12. Heintz, A. S.; Fink, M. J.; Mitchell, B. S., *Adv. Mater.* **2007,** *19*, 3984.
13. Linford, M. R.; Chidsey, C. E. D., *J. Am. Chem. Soc.* **1993,** *115*, 12631.
14. Linford, M. R.; Fenter, P.; Eisenberger, P. M.; Chidsey, C. E. D., *J. Am. Chem. Soc.* **1995,** *117*, 3145.
15. Boukherroub, R.; Morin, S.; Bensebaa, F.; Wayner, D. D. M., *Langmuir* **1999,** *15*, 3831.
16. Cicero, R. L.; Linford, M. R.; Chidsey, C. E. D., *Langmuir* **2000,** *16*, 5688.
17. Stewart, M. P.; Buriak, J. M., *J. Am. Chem. Soc.* **2001,** *123*, 7821.
18. Sun, Q.-Y.; de Smet, L. C. P. M.; van Lagen, B.; Giesbers, M.; Thüne, P. C.; van Engelenburg, J.; de Wolf, F. A.; Zuilhof, H.; Sudhölter, E. J. R., *J. Am. Chem. Soc.* **2005,** *127*, 2514.
19. Tilley, R. D.; Yamamoto, K., *Adv. Mater.* **2006,** *18*, 2053.
20. Lopinski, G. P.; Wayner, D. D. M.; Wolkow, R. A., *Nature* **2000,** *406*, 48.
21. DiLabio, G. A.; Piva, P. G.; Kruse, P.; Wolkow, R. A., *J. Am. Chem. Soc.* **2004,** *126*, 16048.
22. Cicero, R. L.; Chidsey, C. E. D.; Lopinski, G. P.; Wayner, D. D. M.; Wolkow, R. A., *Langmuir* **2001,** *18*, 305.
23. Sieval, A. B.; Demirel, A. L.; Nissink, J. W. M.; Linford, M. R.; van der

Maas, J. H.; de Jeu, W. H.; Zuilhof, H.; Sudhölter, E. J. R., *Langmuir* **1998,** *14*, 1759.
24. Rosso-Vasic, M.; Spruijt, E.; van Lagen, B.; De Cola, L.; Zuilhof, H., *Small* **2008,** *4*, 1835.
25. Boukherroub, R.; Morin, S.; Wayner, D. D. M.; Bensebaa, F.; Sproule, G. I.; Baribeau, J. M.; Lockwood, D. J., *Chem. Mater.* **2001,** *13*, 2002.
26. Woods, M.; Carlsson, S.; Hong, Q.; Patole, S. N.; Lie, L. H.; Houlton, A.; Horrocks, B. R., *J. Phys. Chem. B* **2005,** *109*, 24035.
27. Eves, B. J.; Lopinski, G. P., *Langmuir* **2006,** *22*, 3180.
28. Mischki, T. K.; Lopinski, G. P.; Wayner, D. D. M., *Langmuir* **2009,** *25*, 5626.
29. Wang, X.; Ruther, R. E.; Streifer, J. A.; Hamers, R. J., *J. Am. Chem. Soc.* **2010,** *132*, 4048.
30. Coletti, C.; Marrone, A.; Giorgi, G.; Sgamellotti, A.; Cerofolini, G.; Re, N., *Langmuir* **2006,** *22*, 9949.
31. Bateman, J. E.; Eagling, R. D.; Worrall, D. R.; Horrocks, B. R.; Houlton, A., *Angew. Chem. Int. Ed.* **1998,** *37*, 2683.
32. Yang, Z.; Dobbie, A. R.; Cui, K.; Veinot, J. G. C., *J. Am. Chem. Soc.* **2012,** *134*, 13958.
33. Song, J. H.; Sailor, M. J., *J. Am. Chem. Soc.* **1998,** *120*, 2376.
34. Kelly, J. A.; Henderson, E. J.; Clark, R. J.; Hessel, C. M.; Cavell, R. G.; Veinot, J. G. C., *J. Phys. Chem. C* **2010,** *114*, 22519.
35. Lalevee, J.; Dirani, A.; El-Roz, M.; Allonas, X.; Fouassier, J. P., *Macromolecules* **2008,** *41*, 2003.
36. Panthani, M. G.; Hessel, C. M.; Reid, D.; Casillas, G.; José-Yacamán, M.; Korgel, B. A., *J. Phys. Chem. C* **2012,** *116*, 22463.
37. Yang, Z.; Dasog, M.; Dobbie, A. R.; Lockwood, R.; Zhi, Y.; Meldrum, A.; Veinot, J. G. C., *Adv. Funct. Mater.* **2013**.
38. Hessel, C. M.; Reid, D.; Panthani, M. G.; Rasch, M. R.; Goodfellow, B. W.; Wei, J.; Fujii, H.; Akhavan, V.; Korgel, B. A., *Chem. Mater.* **2011,** *24*, 393.
39. Hessel, C. M.; Henderson, E. J.; Veinot, J. G. C., *J. Phys. Chem. C* **2007,** *111*, 6956.
40. Buriak, J. M., *Chem. Rev.* **2002,** *102*, 1271.
41. Ledoux, G.; Guillois, O.; Porterat, D.; Reynaud, C.; Huisken, F.; Kohn, B.; Paillard, V., *Phys. Rev. B* **2000,** *62*, 15942.
42. Pi, X. D.; Liptak, R. W.; Nowak, J. D.; Wells, N. P.; Carter, C. B.; Campbell, S. A.; Kortshagen, U., *Nanotechnology* **2008,** *19*, 245603.

Chapter 5

The Origin of Nanosecond Lifetime Decay from Orange-Emitting Alkyl-Functionalized Silicon Nanocrystals

5.1 Introduction

Silicon nanocrystals (SiNCs) exhibit promising properties that have potential applications in the fields of optoelectronics devices, ultrafast data communication and data storage, fluorescent labels and biological sensors.[1-6] Researchers have been investigated photoluminescent silicon nanomaterials for no less than twenty years following the discovery of light-emitting porous silicon by Canham.[7] However, the origin of the SiNC PL remains the subject of ongoing debate and numerous explanations exist.[8-16] For quantum dots with direct band gaps (*e.g.*, CdSe, PbS), PL arises from direct relaxation of excited electrons from conduction band back to valance band. Silicon is an indirect band gap semiconductor and thus electrons excited to the conduction band need to seek other paths to return to the ground state (*e.g.*, phonon-assisted transition). Several models, including quantum confinement, defects, and surface states, have been applied to explain the emissive properties of porous silicon and colloidal SiNC systems. Among these explanations, quantum confinement is considered to be a major, if not the factor contributing to SiNC PL and is supported by common observation of size-dependent emission and other experimental results;[10, 17-18] still, many phenomena contradict this model leading to the continued debate.[19-22] For example, pressure-dependent SiNC PLs was observed by Hannah *et al.*,

suggesting that a long-lived phonon-assisted band-gap transition contributes to the PL.[23] This study may finally result in the consensus of the origin of SiNC PL within ultra high vacuum, however, few of these proposals address how SiNC PL is affected by other factors (*e.g.*, surface states, doping effects).[24-27] This is a significant deficiency in our understanding of SiNC optical response, particularly in the context of numerous studies the show PL arising from colloidal SiNCs is dramatically influenced by surface ligands and molecular interactions.[28-30] Clearly, the origin of SiNC PL is a unsolved complex problem.

In general, two broad classifications of PL arising from silicon nanostructures (*e.g.*, porous silicon, SiNCs) have been discovered: i) long lifetime decay (microsecond scale) PL from yellow to infrared region, and ii) a short lifetime decay (nanosecond scale) usually leading to an emission in the blue to green region.[31-32] To date, it has been widely accepted that the comparatively slow microsecond lifetime decay corresponds to the electron relaxation within the intrinsic silicon indirect band structure which requires the assistance from a phonon. While the specific origin of the nanosecond lifetime decay remains unknown, it has been considered as one of the major pieces of experimental evidence for quantum confinement in SiNC PL and points toward the indirect band gap of bulk silicon becomes "direct-like" leading to fast electron-hole recombination.[33-35] Although this hypothesis is supported computationally,[36]

recently experimental results strongly suggest the preservation of indirect band structure within ultrasmall SiNCs.[23] Concomitantly, other explanations for the short-lived excited state lifetime have surfaced and primarily involve fast recombination of the electron and hole via alternative pathways (*e.g.*, surface states or defects created by ligand or oxidation).[10-11, 18, 31, 37-43] While a charge transfer mechanism involving surface species and/or defects have been implicated in the nanosecond scale lifetime of blue-emitting particles,[30, 44] the origin of similar short lifetime decay found from yellow/orange-emitting SiNCs is still unclear.

Some consensus exists that surface oxidation can influence the PL from nano-silicon (e.g., porous silicon, SiNCs). Oxidation on nano-silicon surfaces reportedly induces red- and blue-shifts in the PL maximum, as well as changes (i.e., increases and decreases) in the PL quantum yield.[16] Wolkin and Fauchet found the PL of hydride-terminated porous silicon exhibited a significant red-shift following exposure to oxygen and proposed a model invoking the formation of metastable surface silanones (Si=O) that introduced new electronic states leading to "trapped-electron-to-band" recombination.[16] This silanone surface species remains the subject of controversy and some molecular analogues of this functional group have been reported.[45-48] However, in light of the anticipated complexity of the NC surface, unique bonding motifs cannot be ignored.

Nanosecond lifetime decay has also been reported for alkyl-functionalized and hydride-terminated freestanding yellow/orange emitting SiNCs with significant oxide signals, invoking the reconsideration of the role of surface oxidation.[14, 42-43, 49] However, due to the rapid, spontaneous oxidation of silicon surfaces, most PL studies have focused on uncontrolled oxidation of Si nanomaterials or ignored the influence of surface oxide species unintentionally. Because SiNCs exhibit attractive features for far reaching potentially revolutionary applications and investigation of nanosilicon surface oxidation is a nontrivial,[4, 50] it is crucial that the origin of SiNC nanosecond lifetime decay be studied methodically and thoroughly.

In an effort to exert some control over surface oxidation and correlate a response in the PL of colloidal SiNCs, we designed an approach to limit oxidation using general thermal and photochemical hydrosilylation methods to form dodecyl functionalized SiNCs with two different sizes (diameters *ca.* 3 nm and 5 nm). Hydride-terminated particles were prepared and liberated following well-established solid state synthetic protocol and HF etching process[51]. Thermal hydrosilylation allows particle surfaces to be sufficiently passivated by alkyl ligands following a generally accepted size-independent radical mechanism.[52] The relative quantities and the identities of surface oxides on SiNCs were confirmed by Fourier transform-infrared FT-IR and XPS.

Detailed and accurate photoluminescence data was acquired for the SiNCs using a frequency doubled 400 nm pulses from a regenerative Ti:Sapphire laser (RegA 9000) and a continuous wave 406 nm line from a diode laser (Toptica, iBeam 405) and monitored using a thermoelectrically cooled ultrasensitive CCD couple to a grating spectrometer. The nanosecond- and microsecond-carrier recombination lifetimes were measured using a time-correlated single photon counting (TCSPC) system and a fast photodiode coupled to a 300-MHz oscilloscope, respectively. We observed two types of PL with microsecond and nanosecond lifetime decays from SiNCs that we propose originate from the SiNC core and surface oxide related defects/traps, respectively. Furthermore, the lack of nanosecond lifetime decay from oxide free functionalized SiNCs using photochemical hydrosilylation under prolonged UV irradiation time (*i.e.*, 39 hours) is consistent with the fast lifetime decay corresponding to SiNC orange PL reported previously by others results from partial oxidized surfaces.[14, 49]

5.2 Materials and Methods

5.2.1 Reagents and Materials

Hydrogen silsesquioxane (HSQ) was purchased from Dow Corning Corporation (Midland, MI) as FOx-17. Electronics grade hydrofluoric acid (HF, 49% aqueous solution) was purchased from J. T. Baker. Reagent grade methanol, toluene, ethanol, and 1-dodecene (97%) were purchased from Sigma Aldrich and used as received. Dry toluene was prepared by adding sodium pieces and benzophenone indicator, refluxing for 24 hours.

5.2.2 Synthesis and Liberation of SiNCs

Preparation of oxide-embedded SiNCs (d = 3 nm): Established literature procedures were used to prepare oxide-embedded silicon nanocrystals ($SiNC/SiO_2$).[51] Briefly, solvent was removed from the stock HSQ solution (FOx-17) under vacuum to yield a white solid. The solid (*ca.* 4 g) was placed in a quartz reaction boat and transferred to a Lindberg Blue tube furnace and heated from ambient to a peak processing temperature of 1100 ℃ at 18 ℃ min^{-1} in a slightly reducing atmosphere (5% H_2/95% Ar). The sample was maintained at the peak processing temperature for 1 hour. Upon cooling to room temperature, the resulting amber solid was ground into a fine brown powder using a two-step

process. The solid was crushed using an agate mortar and pestle to remove large particles and finally ground to a fine powder using a Burrell Wrist Action Shaker upon shaking with high-purity silica beads for 5 hours. The resulting SiNC/SiO_2 powders were stable for extended periods and stored in standard glass vials.

Preparation of oxide-embedded SiNCs (d = 5 nm): After grinding with a mortar and pestle (*vide supra*), 0.5 g of SiNC/SiO_2 composite containing 3 nm SiNCs were transferred to a high temperature furnace (Sentro Tech Corp.) for further thermal processing in an inert argon atmosphere. This procedure leads to particle growth while maintaining relatively narrow particle size distributions. In the furnace, the SiNC/SiO_2 composite was heated to 1200 ℃ at 10 ℃/min to achieve the target particle size. Samples were maintained at the peak processing temperature for 1 hour. After cooling to room temperature, the brown composites were ground using procedures identical to those noted above.

Liberation of SiNCs: Hydride-terminated SiNCs were liberated from the SiNC/SiO_2 composite by HF etching. 0.25 g of ground Si-NC/SiO_2 composite were transferred to a polyethylene terephthalate beaker equipped with a Teflon coated stir bar. Ethanol (3 ml) and water (3 ml) were added under mechanical stirring to form a brown suspension followed by 3 ml of 49% HF aqueous solution (**Caution!** HF must be handled with extreme care). After 1 hour of etching in subdued light the suspension appeared orange/yellow.

Hydride-terminated SiNCs were subsequently extracted from the aqueous layer into *ca.* 30 ml of toluene by multiple (*i.e.*, 3 x 10 ml) extractions. The SiNC toluene suspension was transferred to test tubes and the SiNCs were isolated by centrifugation at 3000 rpm.

5.2.3 Thermal and Photochemical Hydrosilylation Approaches

Formation of 3 nm and 5 nm dodecyl-functionalized SiNCs (thermal hydrosilylation): After decanting the toluene supernatant, the resulting hydride-terminated particles were re-dispersed into *ca.* 20 ml dodecene to yield a cloudy suspension which was transferred to a dry 100 ml Schlenk flask equipped with a magnetic stir bar and attached to an argon charged Schlenk line. The flask was evacuated and backfilled with argon three times The Schlenk flask was placed in an oil bath and the temperature was increased to 190 ℃. The reaction was stirred at peak temperature for a minimum of 15 hours yielding a transparent orange/yellow solution.

Formation of 3 nm and 5 nm dodecyl-functionalized SiNCs (photochemical hydrosilylation): After centrifugation at 3000 rpm for 5 minutes, the toluene supernatant was decanted and the precipitated hydride-terminated SiNCs were redispersed into dry toluene. The solution was recentrifuged at 3000 rpm for

another 5 minutes. Again, the toluene supernatant was decanted and the particles were redispersed into dodecene: dry toluene mixture (7.5 ml of dodecene and 30 ml toluene). The mixture was transferred into a pre-dried Schlenk flask equipped with a stir bar and quartz insert for photochemical reaction under an argon atmosphere. The reaction mixtures were subjected to three freeze–pump–thaw cycles, and photochemical hydrosilylation was carried out using a 365 nm UV LED light source for 15 hours. For the functionalization time-dependent study, 5 nm hydride-terminated SiNCs were chosen for model experiments. The UV initiated hydrosilylation reaction mixtures were processed for predefined times (*i.e.*, 20, 30, and 39 hours).

5.2.4 Purification of SiNCs

Following thermal and photochemical hydrosilylation, reaction mixtures were equally distributed amongst 1.5 ml centrifuge tubes (*ca.* 0.3 ml each). *ca.* 1.2 ml of 1:1 methanol/ethanol mixture was added to each tube to yield a cloudy yellow dispersion. The precipitate was isolated by centrifugation in a high-speed centrifuge at 17000 rpm for 15 minutes. The supernatant was decanted and the particles were redispersed in a minimal amount of toluene and subsequently precipitated by addition of 1:1 methanol water. Centrifugation and decanting procedure was repeated twice. Finally, the purified functionalized Si-NCs were

redispersed in toluene, filtered through a 0.45 μm PTFE syringe filter and stored in vials for further use.

5.2.5 Material Characterization and Instrumentation

FT-IR spectroscopy was performed on powder samples using a Nicolet Magna 750 IR spectrophotometer. X-ray photoelectron spectroscopy (XPS) measurements were acquired in the energy spectrum mode at 210 W, using a Kratos Axis Ultra X-ray photoelectron spectrometer. Samples were prepared as film drop-cast from solution onto a copper foil substrate. CasaXPS software (VAMAS) was used to interpret the high-resolution spectra. All of the spectra were internally calibrated to the C 1s emission (284.8 eV). Transmission electron microscopy (TEM) and energy dispersive X-ray (EDX) analyses were performed using a JEOL-2010 (LaB_6 filament) electron microscope with an accelerating voltage of 200 keV. TEM JEOL 2010 with AMT imaging system is calibrated with standard Au nanoparticles (20 nm). The resolution with the analytical polepieces is 0.23nm point to point. High resolution TEM (HRTEM) imaging was performed on a JEOL-2200FS TEM instrument with an accelerating voltage of 200 kV. TEM and HRTEM samples of SiNCs were drop-casted onto a holey carbon coated copper grid and allowing the solvent to evaporate under vacuum. TEM and HRTEM images were processed using ImageJ software

(version 1.45).

PL emission spectra were measured using a thermoelectric-cooled CCD (Acton Pixis 400B, Princeton Instruments) coupled to a spectrometer (Acton SP2500, Princeton Instruments). For ultrafast PL and ns lifetime measurements, the excitation pulse was a 400-nm second harmonic signal from a BBO crystal pumped by 800-nm pulses from a Ti:Sapphire laser (RegA900 with 65 fs pulse width and 250 kHz repetition rate) with an average excitation power of 1.83 mW. The steady state PL was excited by a continuous wave 406 nm (Toptica, iBeam 405) with an average power of 1.05 mW. The PL spectra were corrected to the combined spectral response of the grating and CCD detector. The PL spectra were integrated for 120 s. A 435-nm long pass filter (Edmund optics) was placed at the entrance of the spectrometer to cut off scattered laser pulses. The excitation pulses were focused to the sample using a microscope objective (Nikon, M Plan Apo, 20x/0.45) and the PL was collected by the same objective. Time-resolved PL was recorded using a single-photon avalanche photodiode (SPAD, MAPD) coupled to a TCSPC unit (Picoharp 300, Picoquant). For the microsecond carrier recombination lifetime measurements, 1 kHz frequency-doubled 400nm pulses from another Ti:Sapphire laser (Legend Elite, 45 fs pulse width) were used to excite the PL at an average excitation power of 4.5 mW. A fast silicon photodiode (Thorlabs, PDA36A rise time 20.6 ns) coupled

to a 300 MHz oscilloscope (Tektronix) was used to measure the microsecond carrier recombination lifetime. The photodiode was placed perpendicular to the excitation pulses and a bandpass filter (Edmund Optics) was used to select a particular emission wavelength.

5.3 Results and Discussion

5.3.1 Thermal and Photochemical Hydrosilylation of 3 nm SiNCs

Hydride-terminated SiNCs with diameters of *ca.* 3 nm were prepared following a well-established approach.[51] In a slightly reducing atmosphere (95% Ar/ 5% H_2) at 1100 ℃ the solid white residue obtained upon evaporation of the solvent was heated to induce disproportionation and formation of well-defined SiNCs embedded in an SiO_2-like matrix. Then the particles were liberated using an ethanol/water HF solution mixture and functionalized using thermal and photochemical hydrosilylation protocols. High temperature (*i.e.*, 190 ℃) or UV irradiation (λ = 365 nm, 0.06 mW) was applied in the presence of dodecene to replace the hydride surface termination with dodecyl groups. This procedure was performed under an inert Ar atmosphere for 15 hours and yielded a transparent orange solution. Particles were purified by multi-step antisolvent precipitation and finally redispersed in toluene. Transmission electron microscopy (TEM) confirmed the morphological uniformity of the SiNCs functionalized using these two routes (Figure 5-1). Minimal particle agglomeration was noted in the TEM micrographs and the lattice planes (e.g., Si{111} from the silicon core were revealed by high-resolution TEM (Figure 5-1b,

5-1e). Particles functionalized using both approaches exhibit near identical, statistically equivalent sizes and narrow distributions (Figure 5-1).

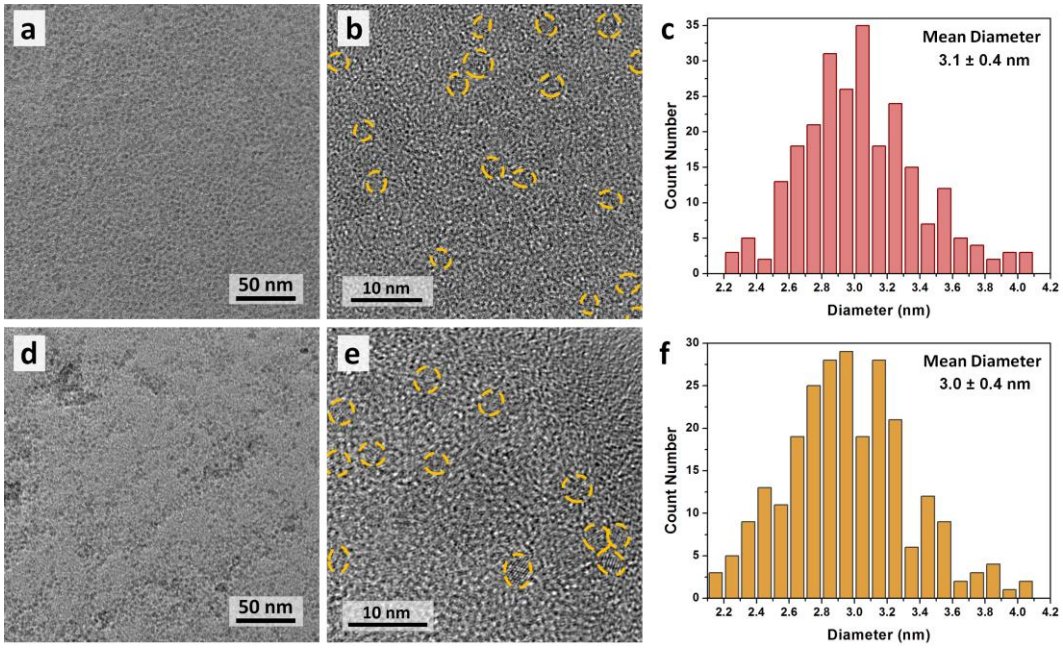

Figure 5-1: Bright field TEM, HRTEM images and size distribution of ensembles of 3 nm dodecyl-passivated silicon nanocrystals functionalized via using thermal (a-c) and photochemical (d-f) hydrosilylation approaches.

FT-IR spectra are consistent with the surfaces of SiNCs being terminated with dodecyl groups (Figure 5-2a). Freshly etched hydride-terminated particles have two distinctive signal regions corresponding to Si–H_x stretching and scissoring (2000 - 2100 cm^{-1} and 900 cm^{-1}). These two signals disappear after hydrosilylation and are replaced with intense vibrations at 2650-2900 cm^{-1} and

1380-1470 cm^{-1}, which are confidently assigned to the dodecyl chain C–H stretching and bonding vibrations. Features in the Si–O–Si stretching region at *ca.* 1100 cm^{-1} are evidence of particle surface oxidation. Experimental and computational studies indicate that surface oxidation is inevitable on alkyl functionalized SiNCs because of the ligand steric hindrance.[53-55] A straightforward comparison of the FTIR spectra from *ca.* 3 nm SiNCs shows more intense Si–O–Si stretching and lower intensities of $Si–H_x$ signals at *ca.* 2100 cm^{-1} and *ca.* 900 cm^{-1} for the photo-functionalized particles. This is consistent with functionalized particles obtained using the thermally induced functionalization possess more complete dodecyl coverage than those obtained from irradiation with 365 nm UV light after equivalent reaction time (*i.e.*, 15 hours).

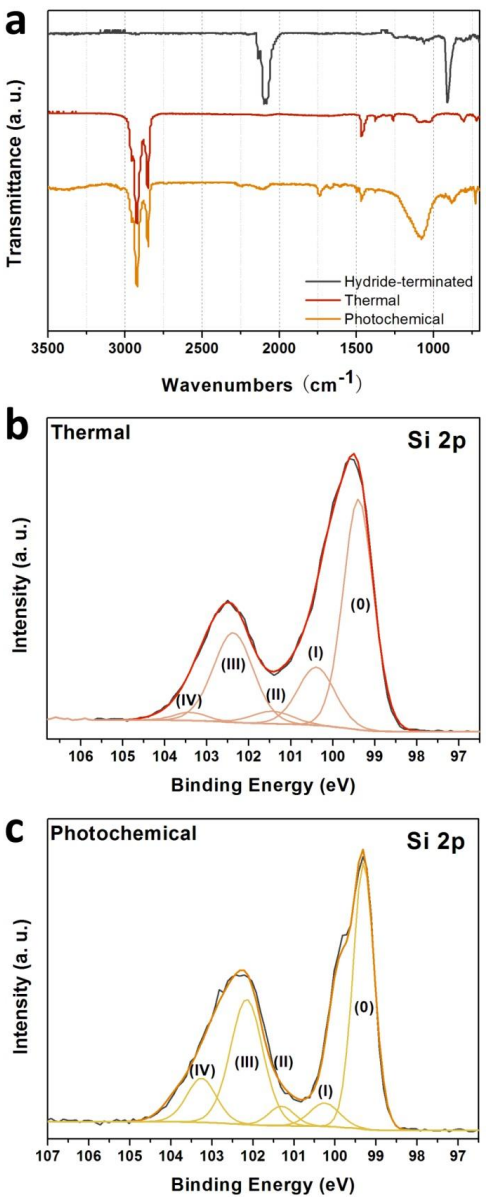

Figure 5-2: (a) FT-IR spectra of 3 nm hydride-terminated (color in black), thermally prepared (red) and photochemically prepared (orange) SiNCs. (b, c) High-resolution XPS spectra of silicon (2p) for 3 nm SiNCs functionalized using these two approaches. The fitting results are shown for the silicon spectrum with Si $2p_{3/2}$ signals. The Si $2p_{1/2}$ signals have been omitted for clarity.

Details of the SiNC surface oxidation were obtained using X-ray photoelectron spectroscopy (XPS). High resolution spectra of Si 2p regions were obtained and calibrated to the C 1s peak at 284.8 eV (Figure 5-2b and 5-2c). Multiple components are found in the Si 2p region within these two materials. For clarity only the Si $2p_{3/2}$ spin-orbit coupling components are shown. The emission at 99.3 eV arises from elemental Si, consistent with previous reports of dodecyl passivated SiNCs.[56] Other features, such as the components at 100.3, 101.4, 102.4 and 103.4 eV, are assigned to ligand functionalized surface, as well as Si oxides. Supporting the FT-IR results, surface oxide species are observed in both XPS samples, while the intensities of Si oxide features are more pronounced/intense for samples functionalized using the photochemical approach.

Functionalized SiNC samples were dispersed in toluene and filtered to yield transparent solutions for PL and lifetime decay measurements. Figure 5-3a shows the images of visible PL from surface modified SiNCs upon exposure to 365 nm UV irradiation. SiNCs functionalized using thermal hydrosilylation show intense red luminescence, while the photochemically processed sample emits bright yellow/orange. The significant difference in emission maximum is reflected in the PL spectra (Figure 5-3b). The emission from the photochemical functionalized SiNCs is centered at *ca.* 634 nm, substantially blue-shifted compared to the thermally functionalized particles (peak center at *ca.* 758 nm).

The origin of the wider linewidth of the PL from the thermally functionalized sample is unclear. One explanation may be the presence of larger particles, which are known to be readily functionalized by size-independent thermal hydrosilylation while similar surface modification is greatly suppressed under 365 nm UV irradiation, however these are not observed in the present TEM analysis.[57] Also, it is possible that the coupled phonon modes of the ligand passivated surface cause broadening of the emission bandwidth.[58-60] Luminescence obtained upon exposure to 400-nm pulses (fluence of 65.4 mJ/cm^2) and 406-nm continuous wave (CW) (average power = 1.05 mW) were compared. The steady-state PL of the SiNCs is slightly red-shifted (10-20 nm) compared to the ultrafast PL. To evaluate the photostability of the SiNC photoluminescence under different laser intensities, a 406 nm CW laser was also applied. Shifts of 1 nm and 13 nm were observed for photochemical and thermal functionalized samples, respectively (Figure 5-3c, 5-3d).

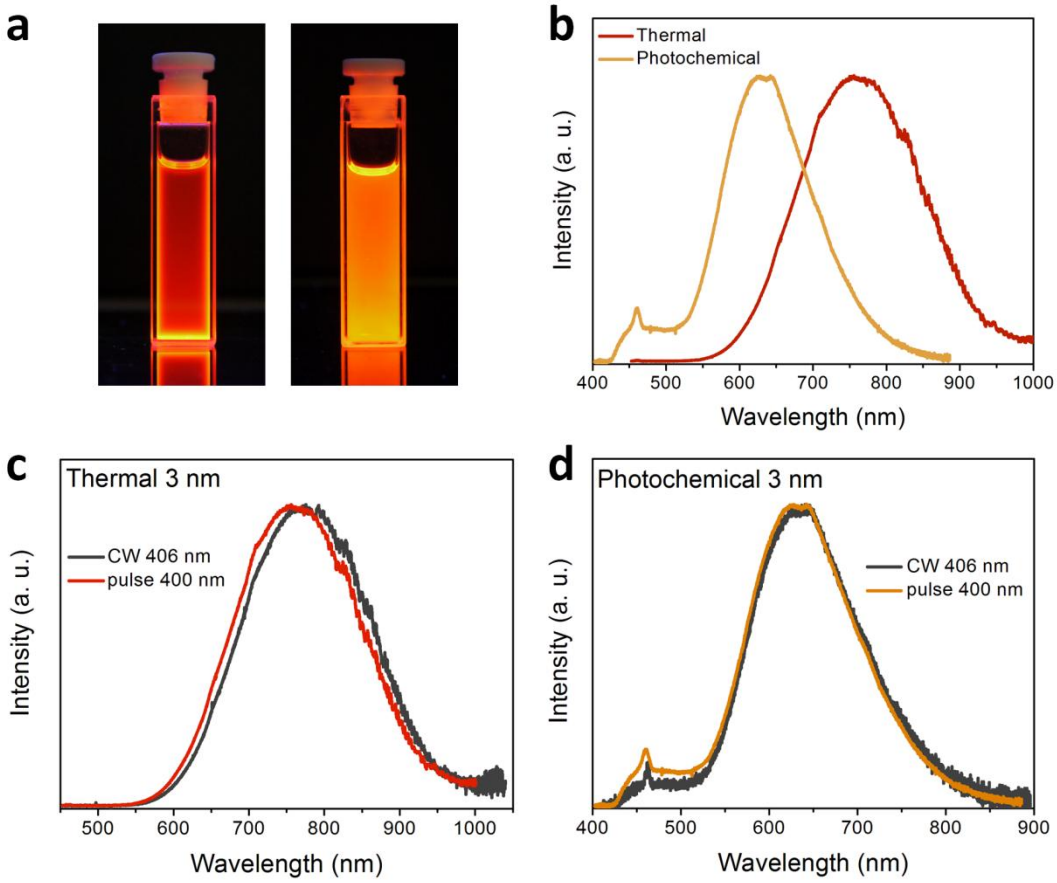

Figure 5-3: (a) Images of toluene dispersion of 3 nm dodecyl functionalized SiNC via thermal (left) and photochemical (right) approaches under UV irradiation and (b) their corresponding PL spectra. (c, d) The comparison spectra of these samples irradiated by CW and pulse laser sources, respectively.

The PL emission maximum of quantum dots, regardless of the material, is frequently predicted using effective mass approximation (EMA)[61] given in Equation 5-1:

$$E_g^{opt} = E_g + \frac{h^2}{8d^2m^*} - \frac{1.786e^2}{\varepsilon_r d} \qquad Equation\ (5-1)$$

$$m^* = \frac{m_e^* m_h^*}{m_e^* + m_h^*}$$

where d is the nanocrystal diameter, e is the electron charge, ε_r is the relative permittivity, for silicon 11.68, m_e^* and m_h^* are the effective masses of the electron and hole equal to 0.19 m_o and 0.286 m_o, where m_0 is the free electron rest mass.[62] The EMA affords predicted peak emission energies for 3.06 nm and 2.97 nm SiNCs at 843 nm (1.47 eV) and 832 nm (1.49 eV), respectively. Both of the experimentally observed PL maxima occur at higher energy than that predicted by the EMA prediction; this is a known deficiency of the EMA.[61] The present PL experimental results are in agreement with previously reported values[62-63] as well as direct band gap measurements using scanning tunneling microscopy results.[26] Furthermore, the evident PL blue-shift for photochemically functionalized SiNCs cannot be simply explained by quantum confinement mechanism since the size and functionalized ligand for the particles prepared both hydrosilylation approaches are alike (Figure 5-1b and 5-1d).

To gain insight into the dynamics of the present red and yellow-orange emitting SiNCs, two different excitation sources were used: a 250-kHz

Ti:Sapphire laser which facilitated evaluation of nanosecond excited state lifetime measurements and a 1-kHz Ti:Sapphire laser for evaluation of microsecond lifetimes. For nanosecond recombination lifetime measurements, time-resolved PL measurements were conducted using a single-photon avalanche photodiode (SPAD) coupled to a time-correlated single-phonon counting (TCSPC) unit. The TCSPC system provides a time resolution of 54 ± 1 ps. The microsecond lifetime component was measured using a fast silicon photodiode coupled to a 300 MHz oscilloscope.

Figure 5-4 shows representative lifetime decay plots for the dodecyl functionalized SiNCs. The microsecond and nanosecond decay plots were fit by a bi-exponential curve (Equation 5-2):

$$y = Ae^{-x/\tau_1} + Be^{-x/\tau_2} \qquad Equation\ (5-2)$$

For particles prepared by thermal hydrosilylation, only microsecond lifetime decays were observed where τ_1 = 36.06 μs and τ_2 = 182.5 μs. The results are in agreement with the consensus that SiNC PL with microsecond lifetime decay originates from the excited electron-hole recombination.[49, 64-66] Microsecond lifetime decays are also found for photochemically modified SiNCs, but the values are smaller (τ_1 = 17.52 μs and τ_2 = 75.14 μs). Nanosecond lifetime decay components were also observed for the present photochemically modified SiNCs. Figure 5-4b shows the decay curves for the short-lived excited states. All time

constants (*i.e.*, τ_x) are sub-7 ns although they show some emission wavelength dependence and when shorter wavelength is chosen. Nanosecond lifetime decay has been commonly found from blue/blue-green emitting SiNCs and most frequently attributed to surface trap and/or charge transfer states (*vide supra*); similar findings for yellow/orange luminescent particles are rare.[14, 49] Kim *et al.* observed similar short lifetime decay from freshly-etched freestanding SiNCs (emission maximum: *ca.* 657 nm).[14] Relying upon the observation of silicon oxide signals in their XPS analysis, they proposed inevitable (and uncontrollable) surface oxidation creates interface defects in which fast electron-hole recombination occurs to explain the nanosecond lifetime. In our case, surface oxides are present in the thermally and photochemically functionalized SiNCs. Moreover, the XPS spectra data indicate that the photochemically modified SiNCs bear more silicon oxide (*vide supra*). Analogous results have been reported by Tsybeskov *et al.* who investigated porous silicon that was intentionally oxidized.[67] These observations suggest it is reasonable that the blue-shifted PL and the nanosecond lifetime exhibited photochemically modified SiNCs originate from the presence of various amount of surface oxide species due to different hydrosilylation approaches.

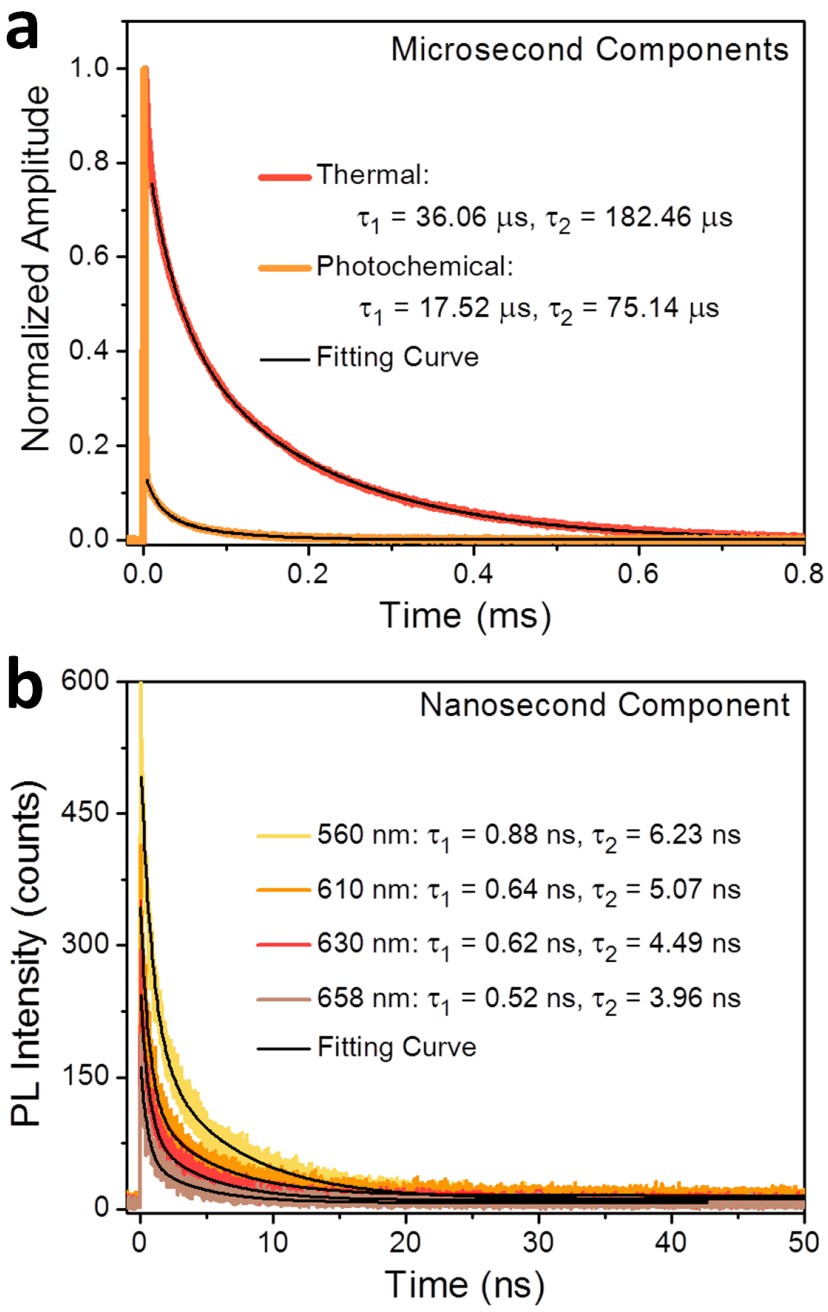

Figure 5-4: (a) Comparison photoluminescence decay in the microsecond regime from 3 nm SiNCs functionalized *via* thermal and photochemical hydrosilylation. (b) Wavelength dependence of photoluminescent decay in the nanosecond regime of 3 nm photochemically functionalized SiNCs.

5.3.2 Thermal and Photochemical Hydrosilylation of 5 nm SiNCs

If the hypothesis of "oxide-induced nanosecond lifetime" is reasonable, the emission should be size independent and the introduction of silicon oxide-based surface defects/traps should invoke similar PL (*i.e.*, blue-shifted PL and nanosecond lifetimes) for SiNCs with different sizes. To explore this possibility, we prepared d = 5 nm SiNCs using an established high temperature annealing process (1200 ℃), functionalized and purified following the identical procedures (*i.e.*, 15-hour thermal or photochemical hydrosilylation) used for particles with d = 3 nm. Particle morphology and size distribution of the functionalized 5 nm SiNCs are shown in Figure 5-5. Particles obtained from the two methods are statistically the same (4.89 ± 0.59 nm (thermal) and 4.68 ± 0.77 nm (photochemical)). Solutions/suspensions of surface functionalized 5 nm SiNC depend upon the surface functionalization methodology: a non-opalescent deep orange solution was obtained from thermally induced surface modification, whereas even after 15-hours of photochemical hydrosilylation, an orange/brown cloudy suspension remained, suggesting the functionalization process was incomplete.

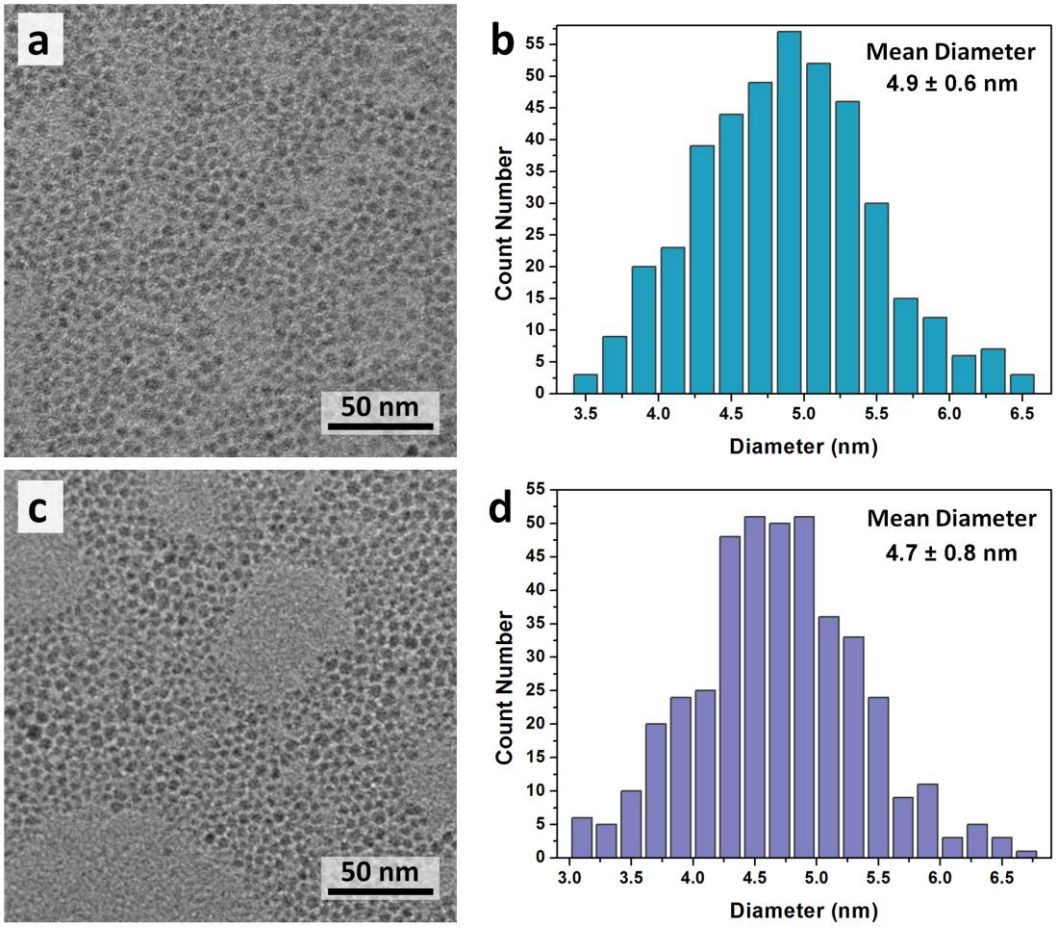

Figure 5-5: Bright field TEM images and size distribution of ensembles of 5 nm dodecyl-passivated silicon nanocrystals functionalized via using thermal (a, b) and photochemical (c, d) hydrosilylation approaches.

Samples were purified and passed through syringe filters to remove any large agglomerates prior to characterization. The resulting particles were characterized by FT-IR and XPS (Figure 5-6). Again, FT-IR spectra indicate the surface modification by dodecyl chains (Si–C stretching at 2650 - 2900 cm^{-1}) while hydride and oxidized silicon are also observed (Si–H_x and Si–O–Si signals

at 2000 - 2150 cm^{-1} and 1100 cm^{-1}, respectively). The XPS spectrum of thermally modified 5 nm SiNCs is similar to that of its 3 nm counterpart but exhibited a negligible Si (IV) peak. In contrast, the photochemically modified 5 nm SiNCs showed evidence of more Si (IV) even when compared to its 3 nm equivalent. It is very likely that spontaneous oxidation also occurs on those unfunctionalized hydride-terminated surfaces during purification and the more complete oxidation originates from more unmodified hydride-terminated surface due to lower reactivity of bigger particles during UV irradiation.

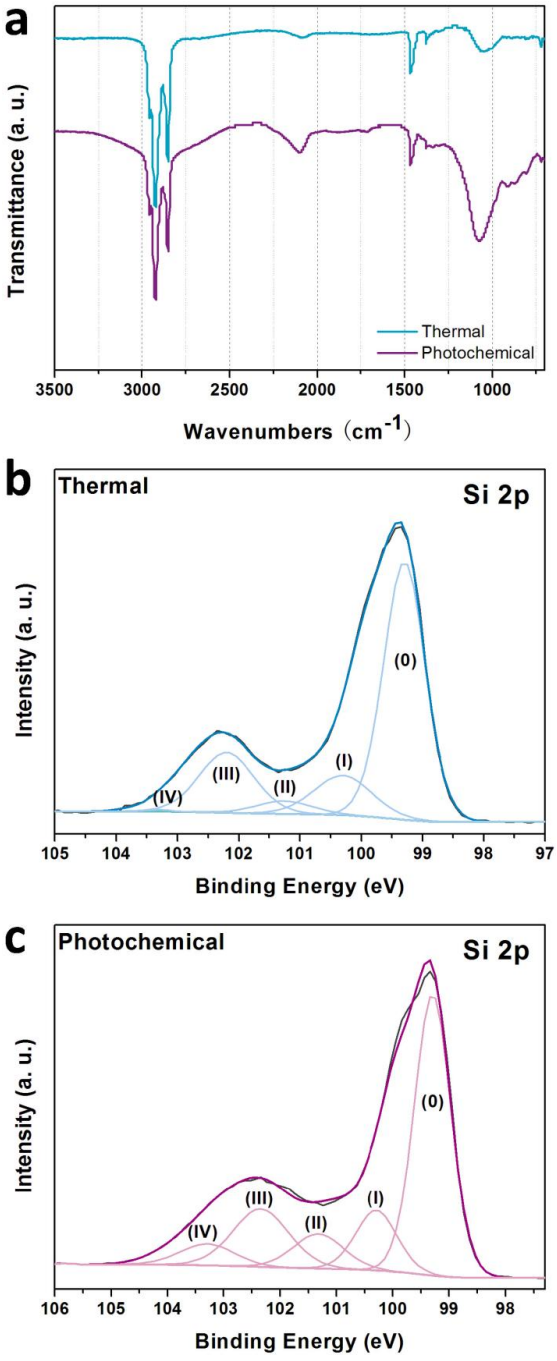

Figure 5-6. (a) FT-IR spectra of 5 nm dodecyl functionalied SiNCs. (b, c) High-resolution XPS spectra of silicon (2p) for 5 nm SiNCs functionalized using these two approaches. The fitting results are shown for the silicon spectrum with Si $2p_{3/2}$ signals. The Si $2p_{1/2}$ signals have been omitted for clarity.

The PL and lifetime measurement of the two d = 5 nm particle samples were measured using a thermally-cooled CCD and a TCSPC system. Photographs of SiNC solutions and corresponding visible PL upon exposure to 365 nm UV lamp are shown in Figure 5-7a; both samples have dark red luminescence. Figure 5-7b shows the PL of 5 nm SiNCs after photochemical and thermal hydrosilylation with dodecene. As expected, for both functionalized samples increasing the size of NCs from 3 nm to 5 nm results in the PL red-shifting (55 nm and 84 nm for the thermally and photochemically prepared samples, respectively); this is in agreement with quantum confinement effects influencing the SiNC PL. Similar to the observations made for d = 3 nm SiNCs, the PL from the photochemically prepared dodecyl SiNCs (PL maximum at 718 nm) is significantly blue-shifted (*ca.* 93 nm) from the emission band obtained from SiNCs prepared *via* thermal hydrosilylation (PL maximum at 813 nm). The possibility that it is the small size difference between two samples that causes such blue-shift is simply excluded by EMA calculated results. Based on EMA, the emission energy difference resulting from the slight size difference between these two samples (Figure 5-5) should be smaller than 0.05 eV, while the actual measured difference is 0.21 eV (1.73 eV *vs.* 1.52 eV). The measured excited state lifetimes are also presented in Figure 5-7c and 5-7d. Again, only microsecond lifetime component was found for the thermally modified SiNCs (τ_1

= 45.40 μs and τ_2 = 234.0 μs), while nanosecond and microsecond lifetimes coexist for SiNCs photochemically functionalized. All lifetime values obtained for the present d = 5 nm samples are slightly larger than those obtained from their d = 3 nm equivalents, consistent with previous studies.[13, 49, 68] Although all PL emission maxima have been red-shifted by size increase, the general trend of PL lifetime decay of these 5 nm samples is retained. The stark similarities (*i.e.*, quantity and identity) of the oxide species determined by FT-IR and XPS as well as the PL response of SiNCs functionalized by both approaches regardless of particle size difference strongly supports the origin of those nanosecond lifetime being the same for the d = 3 and 5 nm NCs.

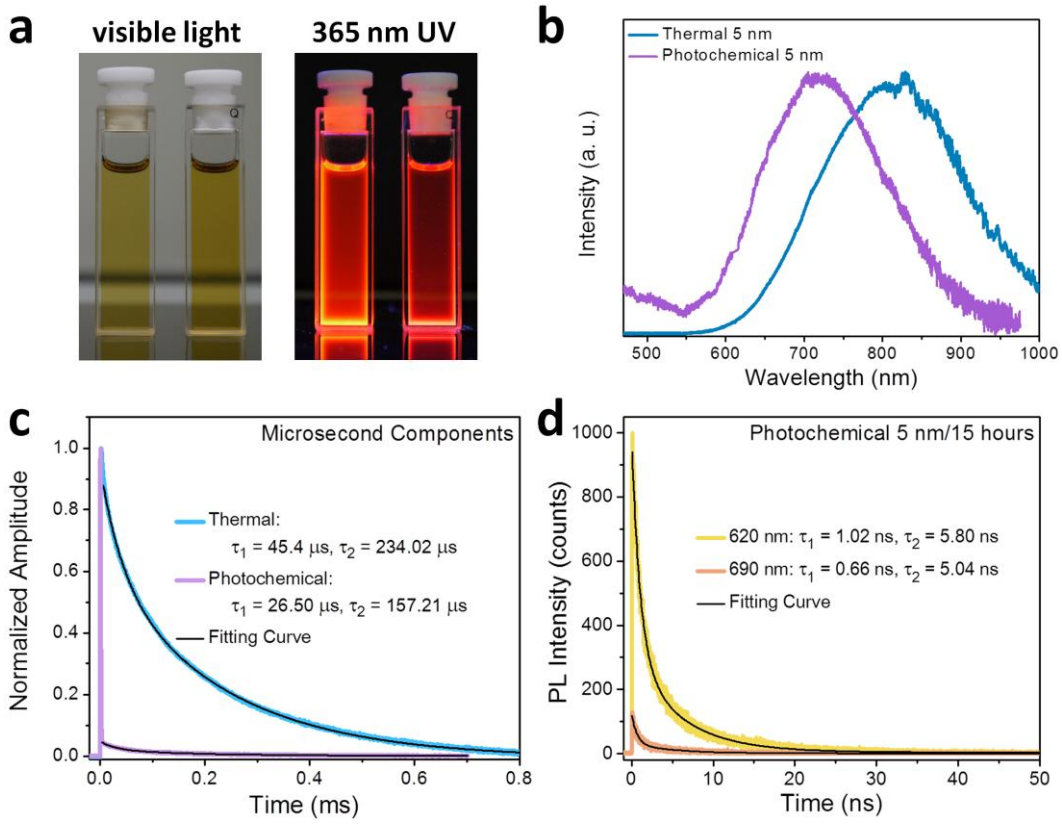

Figure 5-7: (a) Images of toluene dispersion of 5 nm dodecyl functionalized SiNC *via* photochemical (left) and thermal (right) approaches under visible light and UV irradiation and (b) their corresponding PL spectra. (c) Comparison of overall lifetime decays in microsecond region. (d) Wavelength dependent lifetime in nanosecond region of 5 nm photochemically functionalized SiNCs.

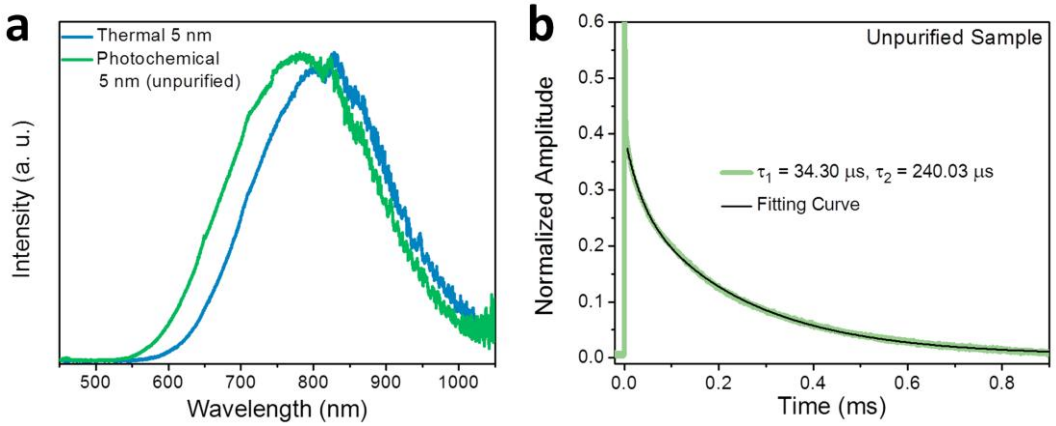

Figure 5-8: (a) PL spectrum of 5 nm unpurified photochemically functionalized SiNCs. The corresponding PL spectrum obtained from 5 nm thermally prepared SiNCs is shown here as comparison. (b) Overall lifetime decay in microsecond region of this unpurified sample.

To further explore the possibility that oxidation resulting from the sample purification procedure induced the change in NC PL properties, a 5 nm dodecyl SiNC sample was freshly prepared by a 15-hour photochemical approach and immediately sent for emission and lifetime measurement without purification (free dodecene does not contribute any PL or lifetime in this experiment). The corresponding emission maximum is *ca.* 781 nm (Figure 5-8a), which is also slightly blue-shifted from the thermal prepared sample (emission maximum at *ca.* 813 nm), but is red-shifted compared to the PL maximum obtained for the purified photochemically modified NCs (emission maximum at *ca.* 718 nm). Moreover, it is important to note that **only** the microsecond lifetime decay was observed

from this fresh, unpurified sample (Figure 5-8b). The τ_1 and τ_2 were equal to 34.30 and 240.0 μs, respectively which are very close to the values obtained from the thermally prepared sample. These pronounced differences in PL maximum and lifetime decay suggest thermally and photochemically initiated hydrosilylation approaches endow similar optical responses of SiNCs during functionalization, however the surfaces of the photochemically functionalized SiNCs are not suitably passivated to prevent as of yet unidentified modification during post functionalization purification. It is reasonable that the affects of post functionalization purification are more pronounced for larger SiNCs particles because of the established size dependence of photochemical hydrosilylation,[57] which leads to less efficient surface passivation. In this context, oxidation of the resulting unfunctionalized silicon surfaces by water or air introduced during purification could induce changes in SiNC optical response.

5.3.3 Time Dependent Photochemical Hydrosilylation of 5 nm SiNCs

To better understand the influence of surface oxidation on the optical response of SiNCs, a series of time-dependent photochemical hydrosilylation experiments were performed. The hypothesis leading this experiment was that higher functionalization temperatures or prolonged reaction times can increase the surface functionalization rate of the thermal hydrosilylation on the SiNCs.[56] It is expected that the prolonged photochemical approach would also provide more complete passivation of the SiNC surfaces and allow for indirect tailoring of the amount of surface oxidation resulting from the workup procedures. Herein, d = 5 nm SiNCs were chosen as the model due to their comparatively slow rate of photochemical hydrosilylation was expected to provide a larger range of surface passivation. Figure 5-9a shows the PL of these SiNCs after functionalization for the indicated reaction times following purification. The PL arising from the 20-hour sample is centered at *ca.* 715 nm. Extending the reaction time to 30 hours induced an obvious red-shift in the PL maximum to *ca.* 776 nm. The red-shift continues with increased reaction time and after 39-hour reaction the PL maximum of SiNCs is centered at *ca.* 792 nm. Consistent with more complete surface functionalization with longer reaction time, samples obtained after a 15

hour photochemical reaction are cloudy, while the solution of SiNCs after 39 hours was completely transparent. Despite the solution appearing non-opalescent and the PL maximum of the shifted to lower energy than that observed for shorter photochemical reactions, the PL maximum exhibited by the 39 hour sample remains slightly PL blue shifted (*ca.* 21 nm) compared to samples prepared thermally. This is readily understood considering larger particles (*e.g.*, > 6 nm) are not readily functionalized using photochemical method.

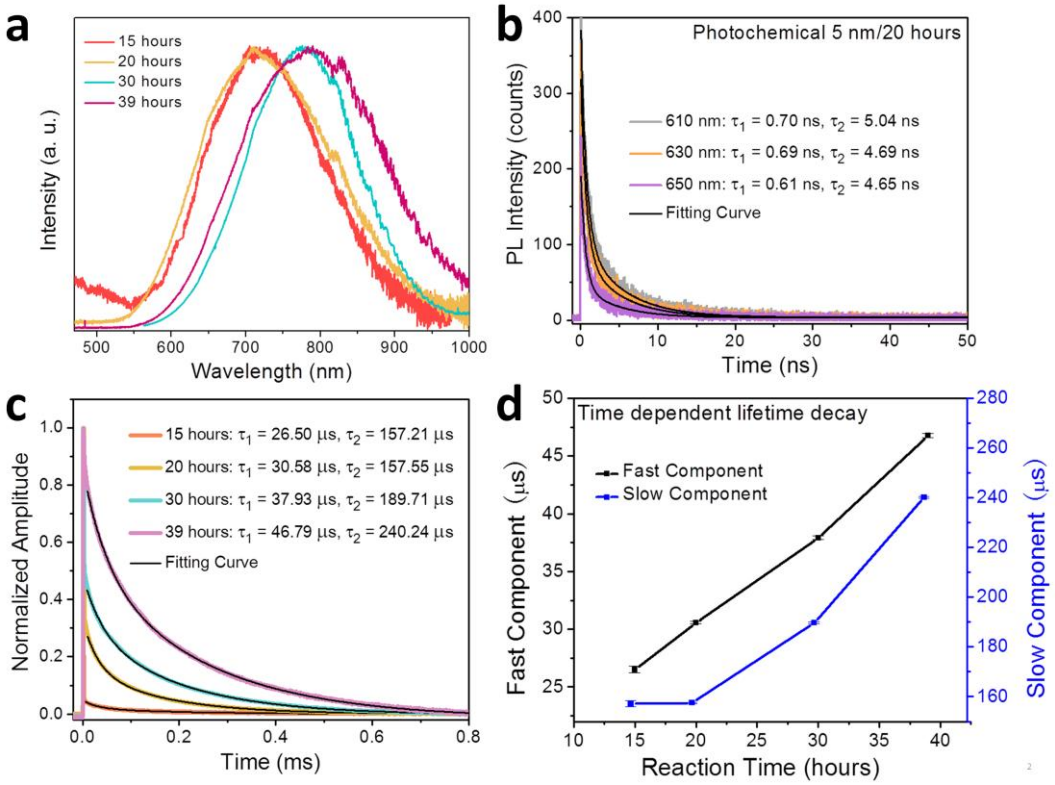

Figure 5-9: (a) PL spectra of 5 nm dodecyl-passivated SiNCs functionalized via time-dependent photochemical hydrosilylation with indicated reaction time. (b) Wavelength dependent lifetime in nanosecond region of 5 nm SiNCs after 20-hour photochemical functionalization. (c) Excited-state lifetime decays and (d) the comparison of fast and slow components (τ_1 and τ_2) in the microsecond region of these photochemically prepared samples.

Based upon our hypothesis, if the PL blue-shift is minimized/eliminated by ensuring complete surface passivation, the nanosecond lifetime component should be suppressed and ultimately disappear if a prolonged photochemical reaction is

employed. Indeed, this is the case for the present reaction time-dependent experiments. All samples exhibited microsecond lifetime components while nanosecond components were only detected for samples obtained from shorter photochemical reactions (*i.e.*, 15 and 20 hours, shown in Figure 5-9b). The trend in the microsecond component (*i.e.*, increase in τ_1 and τ_2) followed the red-shift of the PL maximum (Figure 5-9c) with the values of τ_1 and τ_2 obtained for the "39 hour" samples (τ_1 = 46.79 μs and τ_2 = 240.2 μs) approaching that of the 5 nm thermally modified particles (*i.e.*, τ_1 = 45.40 μs and τ_2 = 234.0 μs). Also, when comparing the lifetimes of the samples obtained from the 15 and 20 hour photochemical reactions times, it was noticed that lifetime in the nanosecond region decreases while lifetime in microsecond increases with increasing reaction time (Figure 5-9b and 5-9c).

The proposal that the abovementioned trends in PL response as a function of reaction time are related to the degree of NC surface oxidation is supported by XPS analysis (Figure 5-10). Increasing the reaction time (from 20 hours to 39 hours) for the photochemical surface modification resulted in a decrease in the intensity of the Si(IV) component (*i.e.*, SiO_2). Simultaneously, the intensities of the signals arising from the silicon sub-oxides (*i.e.*, Si(I), Si(II) and Si(III)) increase slightly, consistent with the proposal that more hydride terminated Si surfaces have been modified by alkyl ligands. However, trace surface oxidation

appears inevitable for the photochemical modification, even after 30-hour UV irradiation.

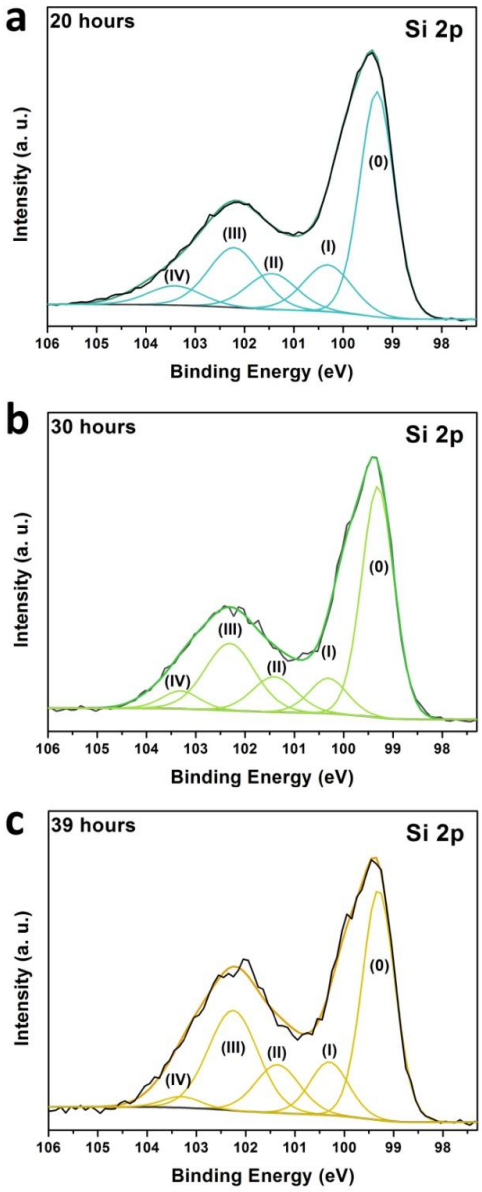

Figure 5-10: High-resolution XPS of the silicon region for purified dodecyl-functionalized 5 nm SiNCs after (a) 20, (b) 30 and (c) 39 hour photochemical hydrosilylation. The Si $2p_{1/2}$ signals have been omitted for clarity.

5.4 Conclusions

In this chapter the interconnection of SiNC nanosecond excited state lifetime and surface oxidation has been examined and confirmed by using carefully designed systematic studies involving SiNC functionalized by dodecene. Differences in the degree of surface reactivity of the thermal and photochemical hydrosilylation methods provide opportunities to control the amount of surface modification on alkyl terminated SiNCs. Microsecond lifetime components were observed from all samples, regardless of functionalization methodology and have been attributed to silicon particle core electron-hole radiative band gap recombination. However, nanosecond lifetime components (< 5 ns) were only observed for samples prepared using the photochemical approach, regardless the size of particles. Time dependent and control experiments indicate the origin of nanosecond lifetime is related to the degree and nature of surface oxidation due to incomplete functionalized SiNC surface which can result from the purification procedure. The phenomena of this fast recombination are consistent with observations in previous reports and the relationship with surface oxidation is supported by detailed electron microscopy and spectroscopy data. Future work will involve quantum yield measurement and single particle studies (*e.g.*, scanning tunneling microscopy or spectroscopy) to investigate the detailed

influence on SiNC surface by oxide species.

5.5 References

1. Alsharif, N. H.; Berger, C. E. M.; Varanasi, S. S.; Chao, Y.; Horrocks, B. R.; Datta, H. K., *Small* **2009**, *5*, 221-228.
2. Erogbogbo, F.; Yong, K.-T.; Roy, I.; Xu, G.; Prasad, P. N.; Swihart, M. T., *ACS Nano* **2008**, *2*, 873-878.
3. Park, J.-H.; Gu, L.; von Maltzahn, G.; Ruoslahti, E.; Bhatia, S. N.; Sailor, M. J., *Nat. Mater.* **2009**, *8*, 331-336.
4. Pavesi, L.; Dal Negro, L.; Mazzoleni, C.; Franzo, G.; Priolo, F., *Nature* **2000**, *408*, 440-444.
5. Holman, Z. C.; Liu, C.-Y.; Kortshagen, U. R., *Nano Lett.* **2010**, *10*, 2661-2666.
6. Liu, C.-Y.; Holman, Z. C.; Kortshagen, U. R., *Nano Lett.* **2008**, *9*, 449-452.
7. Canham, L. T., *Appl. Phys. Lett.* **1990**, *57*, 1046-1048.
8. Sung, K.; Yong Min, P.; Suk-Ho, C.; Kyung Joong, K.; Dong Hoon, C., *J. Phys. D: Appl. Phys.* **2007**, *40*, 1339.
9. de Boer, W. D. A. M.; TimmermanD; DohnalovaK; Yassievich, I. N.; ZhangH; Buma, W. J.; GregorkiewiczT, *Nat. Nanotech.* **2010**, *5*, 878-884.
10. Kanemitsu, Y., *Phys. Rev. B* **1994**, *49*, 16845-16848.
11. Kovalev, D. I.; Yaroshetzkii, I. D.; Muschik, T.; Petrova-Koch, V.; Koch, F., *Appl. Phys. Lett.* **1994**, *64*, 214-216.
12. Fan, J. C.; Chen, C. H.; Chen, Y. F., *Appl. Phys. Lett.* **1998**, *72*, 1605-1607.
13. Garcia, C.; Garrido, B.; Pellegrino, P.; Ferre, R.; Moreno, J. A.; Morante, J. R.; Pavesi, L.; Cazzanelli, M., *Appl. Phys. Lett.* **2003**, *82*, 1595-1597.
14. Kim, S.; Shin, D. H.; Choi, S.-H., *Appl. Phys. Lett.* **2012**, *100*, 253103-3.
15. Žídek, K.; Pelant, I.; Trojánek, F.; Malý, P.; Gilliot, P.; Hönerlage, B.; Oberlé, J.; Šiller, L.; Little, R.; Horrocks, B. R., *Phys. Rev. B* **2011**, *84*, 085321.
16. Wolkin, M. V.; Jorne, J.; Fauchet, P. M.; Allan, G.; Delerue, C., *Phys. Rev. Lett.* **1999**, *82*, 197-200.
17. Sa'ar, A., *Phys. Status Solidi (c)* **2011**, *8*, 1764-1768.
18. Valenta, J.; Fucikova, A.; Pelant, I.; Kůsová, K.; Dohnalová, K.; Aleknavičius, A.; Cibulka, O.; Fojtík, A.; Kada, G., *New J. Phys.* **2008**, *10*, 073022.
19. Luppi, M.; Ossicini, S., *Phys. Rev. B* **2005**, *71*, 035340.
20. Lioudakis, E.; Othonos, A.; Nassiopoulou, A. G., *Appl. Phys. Lett.* **2007**, *90*, -.
21. Dohnalová, K.; Žídek, K.; Ondič, L.; Kůsová, K.; Cibulka, O.; Pelant, I., *J. Phys. D: Appl. Phys.* **2009**, *42*, 135102.
22. Brewer, A.; Von Haeften, K., *Appl. Phys. Lett.* **2009**, *94*, 261102-261102-3.

23. Hannah, D. C.; Yang, J.; Podsiadlo, P.; Chan, M. K. Y.; Demortière, A.; Gosztola, D. J.; Prakapenka, V. B.; Schatz, G. C.; Kortshagen, U.; Schaller, R. D., *Nano Lett.* **2012**, *12*, 4200-4205.
24. Ding, Z.; Quinn, B. M.; Haram, S. K.; Pell, L. E.; Korgel, B. A.; Bard, A. J., *Science* **2002**, *296*, 1293-1297.
25. Kenyon, A. J.; Chryssou, C. E.; Pitt, C. W.; Shimizu-Iwayama, T.; Hole, D. E.; Sharma, N.; Humphreys, C. J., *J. Appl. Phys.* **2002**, *91*, 367-374.
26. Wolf, O.; Dasog, M.; Yang, Z.; Balberg, I.; Veinot, J. G. C.; Millo, O., *Nano Lett.* **2013**, *13*, 2516-2521.
27. Huang, W.-Q.; Huang, Z.-M.; Cheng, H.-Q.; Miao, X.-J.; Shu, Q.; Liu, S.-R.; Qin, C.-J., *Appl. Phys. Lett.* **2012**, *101*, 171601-4.
28. Lauerhaas, J. M.; Sailor, M. J., *Science* **1993**, *261*, 1567-1568.
29. Rosso-Vasic, M.; De Cola, L.; Zuilhof, H., *J. Phys. Chem. C* **2009**, *113*, 2235-2240.
30. Dasog, M.; Yang, Z.; Regli, S.; Atkins, T. M.; Faramus, A.; Singh, M. P.; Muthuswamy, E.; Kauzlarich, S. M.; Tilley, R. D.; Veinot, J. G. C., *ACS Nano* **2013**, *7*, 2676-2685.
31. Valenta, J.; Fucikova, A.; Vácha, F.; Adamec, F.; Humpolíčková, J.; Hof, M.; Pelant, I.; Kůsová, K.; Dohnalová, K.; Linnros, J., *Adv. Funct. Mater.* **2008**, *18*, 2666-2672.
32. Pi, X. D.; Liptak, R. W.; Nowak, J. D.; Wells, N. P.; Carter, C. B.; Campbell, S. A.; Kortshagen, U., *Nanotechnology* **2008**, *19*, 245603.
33. Wilcoxon, J. P.; Samara, G. A.; Provencio, P. N., *Phys. Rev. B* **1999**, *60*, 2704-2714.
34. Dohnalova, K.; Poddubny, A. N.; Prokofiev, A. A.; de Boer, W. D. A. M.; Umesh, C. P.; Paulusse, J. M. J.; Zuilhof, H.; Gregorkiewicz, T., *Light Sci Appl* **2013**, *2*, e47.
35. Sankaran, R. M.; Holunga, D.; Flagan, R. C.; Giapis, K. P., *Nano Lett.* **2005**, *5*, 537-541.
36. Zhou, Z.; Brus, L.; Friesner, R., *Nano Lett.* **2003**, *3*, 163-167.
37. Augustine, B. H.; Irene, E. A.; He, Y. J.; Price, K. J.; McNeil, L. E.; Christensen, K. N.; Maher, D. M., *J. Appl. Phys.* **1995**, *78*, 4020-4030.
38. Liu, N.; Chen, H.-Z.; Chen, F.; Wang, M., *Chem. Phys. Lett.* **2008**, *451*, 70-74.
39. Rosso-Vasic, M.; Spruijt, E.; Popovic, Z.; Overgaag, K.; van Lagen, B.; Grandidier, B.; Vanmaekelbergh, D.; Dominguez-Gutierrez, D.; De Cola, L.; Zuilhof, H., *J. Mater. Chem.* **2009**, *19*, 5926-5933.
40. Dohnalová, K.; Kůsová, K.; Cibulka, O.; Ondič, L.; Pelant, I., *Phys. Scripta* **2010**, *2010*, 014011.

41. Dohnalova, K.; Ondic, L.; Kusova, K.; Pelant, I.; Rehspringer, J. L.; Mafouana, R. R., *J. Appl. Phys.* **2010**, *107*, 053102-053102-6.
42. English, D. S.; Pell, L. E.; Yu, Z.; Barbara, P. F.; Korgel, B. A., *Nano Lett.* **2002**, *2*, 681-685.
43. Kůsová, K.; Cibulka, O.; Dohnalová, K.; Pelant, I.; Valenta, J.; Fučíková, A.; Žídek, K.; Lang, J.; Englich, J.; Matějka, P.; Štěpánek, P.; Bakardjieva, S., *ACS Nano* **2010**, *4*, 4495-4504.
44. Wolf, O.; Dasog, M.; Yang, Z.; Balberg, I.; Veinot, J. G. C.; Millo, O., *Nano Lett.* **2013**.
45. Muraoka, T.; Abe, K.; Haga, Y.; Nakamura, T.; Ueno, K., *J. Am. Chem. Soc.* **2011**, *133*, 15365-15367.
46. Xiong, Y.; Yao, S.; Driess, M., *J. Am. Chem. Soc.* **2009**, *131*, 7562-7563.
47. Rodriguez, R.; Gau, D.; Troadec, T.; Saffon-Merceron, N.; Branchadell, V.; Baceiredo, A.; Kato, T., *Angew. Chem., Int. Ed.* **2013**, *125*, 9150-9153.
48. Xiong, Y.; Yao, S.; Müller, R.; Kaupp, M.; Driess, M., *Nat Chem* **2010**, *2*, 577-580.
49. Mastronardi, M. L.; Maier-Flaig, F.; Faulkner, D.; Henderson, E. J.; Kübel, C.; Lemmer, U.; Ozin, G. A., *Nano Lett.* **2011**, *12*, 337-342.
50. Buriak, J. M., *Chem. Rev.* **2002**, *102*, 1271-1308.
51. Hessel, C. M.; Henderson, E. J.; Veinot, J. G. C., *Chem. Mater.* **2006**, *18*, 6139-6146.
52. Linford, M. R.; Fenter, P.; Eisenberger, P. M.; Chidsey, C. E. D., *J. Am. Chem. Soc.* **1995**, *117*, 3145-3155.
53. Boukherroub, R.; Morin, S.; Wayner, D. D. M.; Bensebaa, F.; Sproule, G. I.; Baribeau, J. M.; Lockwood, D. J., *Chem. Mater.* **2001**, *13*, 2002-2011.
54. Sieval, A. B.; van den Hout, B.; Zuilhof, H.; Sudhölter, E. J. R., *Langmuir* **2000**, *16*, 2987-2990.
55. Sieval, A. B.; van den Hout, B.; Zuilhof, H.; Sudhölter, E. J. R., *Langmuir* **2001**, *17*, 2172-2181.
56. Yang, Z.; Iqbal, M.; Dobbie, A. R.; Veinot, J. G. C., *J. Am. Chem. Soc.* **2013**, *135*, 17595-17601.
57. Kelly, J. A.; Shukaliak, A. M.; Fleischauer, M. D.; Veinot, J. G. C., *J. Am. Chem. Soc.* **2011**, *133*, 9564-9571.
58. Sychugov, I.; Juhasz, R.; Valenta, J.; Linnros, J., *Phys. Rev. Lett.* **2005**, *94*, 087405.
59. Wilson, W. L.; Szajowski, P. F.; Brus, L. E., *Science* **1993**, *262*, 1242-1244.
60. Valenta, J.; Juhasz, R.; Linnros, J., *Appl. Phys. Lett.* **2002**, *80*, 1070-1072.
61. Trwoga, P. F.; Kenyon, A. J.; Pitt, C. W., *J. Appl. Phys.* **1998**, *83*, 3789-3794.
62. Hessel, C. M.; Reid, D.; Panthani, M. G.; Rasch, M. R.; Goodfellow, B. W.;

Wei, J.; Fujii, H.; Akhavan, V.; Korgel, B. A., *Chem. Mater.* **2011**, *24*, 393-401.
63. Clark, R. J.; Dang, M. K. M.; Veinot, J. G. C., *Langmuir* **2010**, *26*, 15657-15664.
64. Delerue, C.; Allan, G.; Lannoo, M., *Phys. Rev. B* **1993**, *48*, 11024-11036.
65. Proot, J. P.; Delerue, C.; Allan, G., *Appl. Phys. Lett.* **1992**, *61*, 1948-1950.
66. Garcia, C.; Garrido, B.; Pellegrino, P.; Ferre, R.; Moreno, J. A.; Morante, J. R.; Pavesi, L.; Cazzanelli, M., *Appl. Phys. Lett.* **2003**, *82*, 1595-1597.
67. Tsybeskov, L.; Vandyshev, J. V.; Fauchet, P. M., *Phys. Rev. B* **1994**, *49*, 7821-7824.
68. Lockwood, R.; Meldrum, A., *Phys. Status Solidi (a)* **2009**, *206*, 965-968.

Chapter 6

Conclusions and Future Directions

6.1 Conclusions

As one of the important members in the family of semiconductor nanomaterials, silicon nanocrystals (SiNCs) have been widely studied and applied in areas of energy conversion and storage, catalyst, biotechnology, and optoelectronic devices not only because of their unique size-dependent intense photoluminescence, but also many favorable physical and chemical properties.[1-4] These properties open the door to many new applications such as, magnetic resonance imaging (MRI) and anodes for lithium ion batteries. Despite the practical potential of these exciting materials, it is important to realize that fundamental studies are still necessary if their full potential is to be realized.

Four research projects comprising this thesis belong to three major areas within the scope SiNC science: (i) particle morphology control and crystal evolution; (ii) silicon surface chemistry and (iii) its corresponding influence on optical properties; and (iv) synthesis and fabrication of homogenous SiNC/polymer hybrid materials. All particles utilized in these projects were synthesized and liberated following an well-established solid state synthetic protocol and HF etching procedure developed since 2006 by the Veinot Group.[5]

Chapter Two demonstrated the shape evolution of SiNCs upon high temperature annealing of oxide embedded SiNCs obtained from thermal

processing of hydrogen silsesquioxane (HSQ). The control of SiNCs size through alternating synthetic parameters have been shown previously. Yet reports of shape controlled syntheses of silicon nanomaterials are rare and even nonexistent because the strong directional bonding in Si precludes standard colloidal synthesis. Using TEM and XRD, it was shown that prolonged annealing induces diffusion of the surface atoms of spherical SiNCs to self-optimize and yield a variety of faceted structures (*e.g.,* cubic, truncated trigonal and hexagonal structures). The optimization of the processing time and temperature could effectively form nanocubes in an oxide matrix. Similar atomic diffusion was indirectly observed through the formation of larger faceted structures (i.e., 1400 ℃).

For preparing nanoparticle/polymer hybrids, one of looming challenges is achieving a uniform dispersion of small particles within the polymer matrix while also minimizing agglomeration. In Chapter Three, a facile approach to highly luminescent homogenous SiNC/polystyrene hybrid materials was described. Instead of following Si-H bond hemolytic cleavage mechanism in thermal hydrosilylation method, in the work presented herein styrene was a radical initiator. SiNC surface modification by polymers was confirmed by IR and Raman spectra and the molecular weight information and particle concentration of such hybrids were studied by GPC and TGA. Furthermore, it was shown that

combining the properties of silicon nanocrystals with polymers significantly increases solubility, and processability. Thus providing the opportunity to fabricate various uniform nano- and microscale architectures (i.e., inner wall-coated optical fibers/capillaries, nanofibers and thin films).

In Chapter Four, the surface functionalization of hydride-terminated SiNCs with dodecene via thermal hydrosilylation was reexamined. MALDI-MS detected the presence of dodecyl oligomers ($n \leq 4$) in the products obtained from the reaction performed under in argon atmosphere at various temperatures (100 ℃ – 190 ℃). In a comparative study, surface hydrosilylation and ligand oligomerization were found to be more pronounced when reactions were performed air (*n* up to 7). These observations strongly suggest that hydrogen abstraction by oxygen accelerates hydrosilylation and generates sufficient silyl radicals to induce reaction with unsaturated bonds, promote chain propagation and generate ligand oligomers. Furthermore, systematic experiments showed it is feasible to control ligand oligomerization and obtain monolayer coverage on SiNC surfaces.

There is a protracted debate over how surface atoms influence the SiNC PL response. Red/blue shifts of PL during hydrosilylation of SiNCs with alkyl terminated surface is frequently mentioned. Chapter five reported a systematic study to compare the difference of PL shift from two hydrosilylation methods:

thermal and photochemical. It was noted that after functionalization SiNCs showed oxide signals in the XPS and IR with different intensities, that correlated with the degree of blue-shift in emission spectrum. Microsecond lifetime components were detected in all time resolved PL analysis of these samples, and were attributed to recombination from the conduction band to the valence band; in addition nanosecond lifetime components were only observed in samples prepared using photochemical hydrosilylation, regardless of the size of particles. Time dependent and control experiments strongly suggest the origin of nanosecond lifetime is relative to surface defects/traps created by oxidation of incomplete functionalized SiNC surface during purification process.

6.2 Future Directions

6.2.1 Development of SiNC surface modification approaches.

Numerous approaches have been discovered and developed for functionalizing SiNCs and most of them originate from the reactions reported on the bulk silicon system. Still, the curved and faceted surfaces of SiNCs are substantially different with those on ideal flat silicon films, which might introduce unexpected results even from similar reactions. While hydrosilylation is relatively effective and efficient for passivating the SiNC surface, shortcomings

remain and significantly restrain the applicability of hydrosilylation in particular circumstances as described in this thesis (*i.e.*, Chapters Four and Five). The development of alternative surface modification approaches is certainly possible. For example, preliminary investigations of radical initiator involved hydrosilylation indicate that hydride-terminated SiNC surfaces can be modified at much lower temperature without the formation of ligand oligomers/polymers. Another potential promising method is dehydrocoupling functionalization of SiNCs with organosilanes. Unpublished results show Wilkinson's catalyst is can catalyze dehydrocoupling between hydride-terminated SiNC and various silanes (*e.g.*, primary and tertiary alkylsilanes) under mild reaction conditions.

6.2.2 Conjugated Polymer/Silicon Nanocrystal Hybrid Silicon Solar Cell.

Hybrid solar cells containing the mixture of SiNCs and conjugated polymers are definitely appealing, not only because of the energetically favorable electron dissociation at the interface, solution processability and lower cost of manufacturing, but also because it merges the advantages of SiNCs (e.g., strong UV absorption, tunable band gap and feasible surface modification)[6-8] and the properties of conjugated polymers (e.g., light weight, flexibility and customizable composition).[9] Since 2009, several prototypes of polymer/SiNC solar cell have

been fabricated by the integration of hydride-terminated SiNCs and widely-used conjugated polymers (e.g., polythiophene, poly(*p*-phenylene vinylene)).[7-8, 10] Currently the power conversion efficiency (PCE) of polymer/SiNC hybrid solar cells has been improved to 3.2 %,[11] yet it is still much lower than those records achieved by conjugated polymer or CdSe QD based solar cells. The relativity low PCEs of those SiNC devices may be primarily caused by lack of covalent hydride-terminated silicon surface. Both of these two factors would significantly affect electron/hole mobility and device stability. Hydrosilylation is a versatile method for functionalization of silicon surface with organic ligand monomer/polymer and protecting silicon from oxidation. In Chapter 3, a bulk synthetic approach to form homogenous SiNC/polystyrene hybrids with high photoluminescence and solution processability was developed, which could be feasible to extend to other polymer/SiNC systems. Also, literature has shown thiophene species can directly attached silicon surface by surface modification.[12] Therefore, it is possible that using conjugated polymer functionalized SiNCs as the absorption layer may effectively improve the performance of SiNC hybrid solar cells.

6.2.3 Carbon/Silicon Nanocrystal Based Lithium-Ion Battery Electrodes

Silicon is an ideal anode material candidate for lithium-ion battery application because of its high capacity (4200 $mAhg^{-1}$) and low toxicity.[13-15] However, its large volume change during lithiation/delithiation may induce crystal pulverization and cause rapid capacity decay upon continuous cycling.[16-17] Using SiNCs as an electrode can effectively avoid the influence of volume change mainly because there is sufficient space between particles to accommodate the volume change. However, during cycling they might impinge during lithiation and detach from their electrical connections, which also leads to capacity fading.[15] To overcome these challenges, new structures such as Si materials (e.g., SiNCs, Si nanowires) encapsulated in a conductive coating layer have been proposed and show improved performance.[18-19] Carbon nanomaterials, such as graphene, graphene oxide, and ultrathin graphite have high electrical conductivity, low density, and superior flexibility and thus have been applied as the coating materials to improve SiNC electrode stability.[20-23] Since both graphene and ultrathin graphite have a similar sp^2 unsaturated carbon network, it is believed that an optimized hydrosilylation approach could also be utilized to graft carbon surface on hydride-terminated SiNC surfaces. These chemical linkages are able

to enlarge ion conductivity between carbon and silicon and further stabilize SiNCs onto carbon matrix is foreseeable to become an important process for the development of lithium-ion battery electrodes.

6.3 References

1. Zhong, Y.; Peng, F.; Bao, F.; Wang, S.; Ji, X.; Yang, L.; Su, Y.; Lee, S.-T.; He, Y., *J. Am. Chem. Soc.* **2013**, *135*, 8350-8356.
2. Liu, J.; Erogbogbo, F.; Yong, K.-T.; Ye, L.; Liu, J.; Hu, R.; Chen, H.; Hu, Y.; Yang, Y.; Yang, J.; Roy, I.; Karker, N. A.; Swihart, M. T.; Prasad, P. N., *ACS Nano* **2013**, *7*, 7303-7310.
3. Cheng, K.-Y.; Anthony, R.; Kortshagen, U. R.; Holmes, R. J., *Nano Lett.* **2010**, *10*, 1154-1157.
4. Jang, H.; Pell, L. E.; Korgel, B. A.; English, D. S., *J. Photochem. Photobiol. A* **2003**, *158*, 111-117.
5. Hessel, C. M.; Henderson, E. J.; Veinot, J. G. C., *Chem. Mater.* **2006**, *18*, 6139-6146.
6. Herrmann, D.; Niesar, S.; Scharsich, C.; Köhler, A.; Stutzmann, M.; Riedle, E., *J. Am. Chem. Soc.* **2011**, *133*, 18220-18233.
7. Liu, C.-Y.; Holman, Z. C.; Kortshagen, U. R., *Nano Lett.* **2008**, *9*, 449-452.
8. Liu, C.-Y.; Holman, Z. C.; Kortshagen, U. R., *Adv. Funct. Mater.* **2010**, *20*, 2157-2164.
9. Wright, M.; Uddin, A., *Sol. Energ. Mat. Sol. Cells* **2012**, *107*, 87-111.
10. Liu, C.-Y.; Kortshagen, U. R., *Nanoscale* **2012**, *4*, 3963-3968.
11. Kim, S.; Jeon, K.; Lee, J. C.; Swihart, M. T.; Yang, M., *Appl. Phys. Express 5*, 022302.
12. O'Leary, L. E.; Rose, M. J.; Ding, T. X.; Johansson, E.; Brunschwig, B. S.; Lewis, N. S., *J. Am. Chem. Soc.* **2013**, *135*, 10081-10090.
13. Huggins, R. A., *J. Power Sources* **1999**, *81–82*, 13-19.
14. Park, C.-M.; Kim, J.-H.; Kim, H.; Sohn, H.-J., *Chem. Soc. Rev.* **2010**, *39*, 3115-3141.
15. Wu, H.; Cui, Y., *Nano Today* **2012**, *7*, 414-429.
16. Yu, Y.; Gu, L.; Zhu, C.; Tsukimoto, S.; van Aken, P. A.; Maier, J., *Adv. Mater.* **2010**, *22*, 2247-2250.
17. Liu, X. H.; Zhong, L.; Huang, S.; Mao, S. X.; Zhu, T.; Huang, J. Y., *ACS Nano* **2012**, *6*, 1522-1531.
18. Hu, Y.-S.; Demir-Cakan, R.; Titirici, M.-M.; Müller, J.-O.; Schlögl, R.; Antonietti, M.; Maier, J., *Angew. Chem., Int. Ed.* **2008**, *47*, 1645-1649.
19. Wu, H.; Zheng, G.; Liu, N.; Carney, T. J.; Yang, Y.; Cui, Y., *Nano Lett.* **2012**, *12*, 904-909.
20. Zhu, Y.; Murali, S.; Stoller, M. D.; Ganesh, K. J.; Cai, W.; Ferreira, P. J.; Pirkle, A.; Wallace, R. M.; Cychosz, K. A.; Thommes, M.; Su, D.; Stach, E. A.; Ruoff, R. S., *Science* **2011**, *332*, 1537-1541.

21. Lee, J. K.; Smith, K. B.; Hayner, C. M.; Kung, H. H., *Chem. Commum.* **2010**, *46*, 2025-2027.
22. Zhou, X.; Yin, Y.-X.; Wan, L.-J.; Guo, Y.-G., *Adv. Energy Mater.* **2012**, *2*, 1086-1090.
23. Ji, J.; Ji, H.; Zhang, L. L.; Zhao, X.; Bai, X.; Fan, X.; Zhang, F.; Ruoff, R. S., *Adv. Mater.* **2013**, *25*, 4673-4677.